

# The LAMOST Stellar Parameter Pipeline at Peking University — LSP3

M. S. Xiang<sup>1\*</sup>, X. W. Liu<sup>1,2†</sup>, H. B. Yuan<sup>2</sup>, Y. Huang<sup>1</sup>, Z. Y. Huo<sup>3</sup>, H. W. Zhang<sup>1</sup>, B. Q. Chen<sup>1</sup>, H. H. Zhang<sup>1</sup>, N. C. Sun<sup>1</sup>, C. Wang<sup>1</sup>, Y. H. Zhao<sup>3</sup>, J. R. Shi<sup>3</sup>, A. L. Luo<sup>3</sup>, G. P. Li<sup>4</sup>, Y. Wu<sup>3</sup>, Z. R. Bai<sup>3</sup>, Y. Zhang<sup>4</sup>, Y. H. Hou<sup>4</sup>, H. L. Yuan<sup>3</sup>, G. W. Li<sup>3</sup>

<sup>1</sup> Department of Astronomy, Peking University, Beijing 100871, P. R. China

<sup>2</sup> Kavli Institute for Astronomy and Astrophysics, Peking University, Beijing 100871, P. R. China

<sup>3</sup> Key Laboratory of Optical Astronomy, National Astronomical Observatories, Chinese Academy of Sciences, Beijing 100012, P. R. China

<sup>4</sup> Nanjing Institute of Astronomical Optics & Technology, National Astronomical Observatories, Chinese Academy of Sciences, Nanjing 210042, P. R. China

Received:

## ABSTRACT

We introduce the LAMOST Stellar Parameter Pipeline at Peking University — LSP3, developed and implemented for the determinations of radial velocity  $V_r$  and stellar atmospheric parameters (effective temperature  $T_{\text{eff}}$ , surface gravity  $\log g$ , metallicity [Fe/H]) for the LAMOST Spectroscopic Survey of the Galactic Anti-center (LSS-GAC). We describe the algorithms of LSP3 and examine the accuracy of parameters yielded by it. The precision and accuracy of parameters yielded are investigated by comparing results of multi-epoch observations and of candidate members of open and globular clusters, with photometric calibration, as well as with independent determinations available from a number of external databases, including the PASTEL archive, the APOGEE, SDSS and RAVE surveys, as well as those released in the LAMOST DR1. The uncertainties of LSP3 parameters are characterized and quantified as a function of the spectral signal-to-noise ratio (SNR) and stellar atmospheric parameters. We conclude that the current implementation of LSP3 has achieved an accuracy of  $5.0 \text{ km s}^{-1}$ , 150 K, 0.25 dex, 0.15 dex for the radial velocity, effective temperature, surface gravity and metallicity, respectively, for LSS-GAC spectra of FGK stars of SNRs per pixel higher than 10. The LSP3 has been applied to over a million LSS-GAC spectra collected hitherto. Stellar parameters yielded by the LSP3 will be released to the general public following the data policy of LAMOST, together with estimates of the interstellar extinction  $E(B - V)$  and stellar distances, deduced by combining spectroscopic and multi-band photometric measurements using a variety of techniques.

**Key words:** Galaxy: disk – stars: abundance – techniques: spectroscopy – techniques: radial velocity – surveys

## 1 INTRODUCTION

The structure and origin of the Galactic disk(s) are among the hottest debating issues of the Galactic astronomy. An archeological approach to the problems relies on the collection of information in multi-dimensional phase space for large samples of stars. The ongoing LAMOST Spectroscopic Survey of the Galactic Anti-center (LSS-GAC), will collect medium-to-low resolution ( $R \sim 1800$ ) spectra of millions of stars and deliver fundamental stellar parameters, including radial velocity ( $V_r$ ) and stellar atmospheric param-

eters (effective temperature  $T_{\text{eff}}$ , surface gravity  $\log g$ , metallicity [Fe/H]), as well as elemental abundance ratios (the  $\alpha$ -element to iron abundance ratio  $[\alpha/\text{Fe}]$ , and the carbon to iron abundance ratio [C/Fe]), deducible from the spectra (Liu et al. 2014). Combined with accurate optical and infrared (IR) photometry, the LSS-GAC will also deliver estimates of the interstellar extinction and distances to individual stars (Yuan et al. 2014, submitted; Paper III hereafter). Together with determinations of proper motions, either from existing catalogs, such as the PPMXL (Roeser et al. 2010) and UCAC4 (Zacharias et al. 2013), or from the forth coming measurements of Gaia of unprecedented accuracy (Perryman et al. 2001), as well as accurate parallaxes (distances) also provided by Gaia, the LSS-GAC will provide an unprecedented large stellar database

\* E-mail: xms@pku.edu.cn

† E-mail: x.liu@pku.edu.cn

in multi-dimensional phase space to study the stellar populations, kinematics and chemistry of the Galactic disk and its assemblage and evolution history. Deriving accurate stellar parameters from millions of medium-to-low resolution fiber spectra in an efficient way is thus of fundamental importance to fulfill the scientific goals of LSS-GAC.

Various methods have been developed in the past to derive stellar atmospheric parameters from large number of medium-to-low resolution spectra (Recio-Blanco et al. 2006; Lee et al. 2008a, Wu et al. 2011). The approaches generally fall into two main categories of method (Wu et al. 2011): the minimum distance method (MDM) and non-linear regression method. Both categories of method have been applied to large stellar spectroscopic surveys, including the SEGUE (Yanny et al. 2009), RAVE (Steinmetz et al. 2006), APOGEE (Majewski et al. 2007) and LAMOST (Zhao et al. 2012). The MDM is usually based on spectral template matching, and searches for the template spectrum that has the shortest distance in parameter space from the target spectrum. The  $\chi^2$  minimization, cross-correlation, weighted mean algorithm, and the  $k$ -nearest neighbor (KNN), are thought to be specific cases of MDM (Wu et al. 2011). Softwares and pipelines developed based on those algorithms include the TGMET (Katz et al. 1998), MATISSE (Recio-Blanco et al. 2006), SSPP (Lee et al. 2008a), ULySS (Koleva et al. 2009), that of Allende Prieto et al. (2006) and of Zwitter et al. (2008). The non-linear regression method is sometimes also referred to as the artificial neural network (ANN). The method constructs a functional mapping between the spectra and stellar atmospheric parameters by training a library of template spectra with non-linear algorithms such as the principal component analysis (PCA), and then apply the mapping to target spectra. Related work can be found in Re Fiorentin et al. (2007) and Lee et al. (2008a). In addition to the above two categories of method, other approaches have been developed, for example, the line-index method based on the relations between the stellar atmospheric parameters and the equivalent widths of spectral features and/or photometric colours (Wilhelm et al. 1999; Beers et al. 1999; Cenarro et al. 2002). More recently, a Bayesian approach to determine stellar atmospheric parameters combining spectral and photometric measurements has been developed by Schönrich & Bergemann (2013).

Different methods usually have different valid parameter ranges, outside which the methods perform poorly. For example, the line-index method usually loses sensitivity when the adopted metallic lines are either saturated or too weak. Because stars are widely distributed in the parameter space and different spectral features have different sensitivity to the atmospheric parameters, one can hardly rely on one single method to derive stellar atmospheric parameters with a uniform accuracy for all types of star. A “multi-method” approach, which takes averaged stellar atmospheric parameters deduced from a variety of methods that utilizes different spectral wavelength ranges, is adopted by the SSPP (Lee et al. 2008a). Since systematic errors from different methods cannot be easily compared and combined, the systematic errors of the final parameters are difficult to estimate.

Almost all of the methods determine the stellar atmospheric parameters via either direct or indirect comparisons between the target and template spectra, a set of comprehensive templates of known parameters covering a broad parameter space are thus of fundamental importance. Both libraries consisting of empirical and synthetic spectral templates have been used in the literature. Lists of the currently available empirical and synthetic libraries can be found in Wu et al. (2011) and at a website on stellar spectral li-

braries<sup>1</sup>. An advantage of the empirical libraries is that they consist of spectra of *real* stars. The disadvantage is that it is often laborious and time-consuming to build an empirical spectral library of stars of accurately known parameters that cover wide parameter ranges with sufficient resolution and homogeneity. It is clear that the parameter space encompassed by the existent empirical libraries are limited by our current knowledge of stars in the solar neighborhood and the available observations. On the other hand, while it may be straightforward to construct a set of synthetic spectra covering homogeneously a wide parameter space, it is difficult to assess the robustness of the spectra, especially those of very low ( $T_{\text{eff}} < 4500$  K) or high temperatures (for instance, stars of the O, B or A spectral types). Properties of stellar spectra are determined not only by basic stellar parameters such as  $T_{\text{eff}}$ ,  $\log g$ ,  $[\text{Fe}/\text{H}]$  and  $[\alpha/\text{Fe}]$ , but also depend on other parameters and processes such as the micro-turbulence and rotation velocities as well as convection. Observational uncertainties combined with inadequacies in our understanding of stellar atmospheres may lead to unrealistic parameters  $T_{\text{eff}}$ ,  $\log g$ ,  $[\text{Fe}/\text{H}]$  and  $[\alpha/\text{Fe}]$  by matching an observed medium-to-low resolution spectrum with a library of synthetic spectra.

Thanks to the efforts involving many observers, several empirical spectral libraries, including the ELODIE (Prugniel & Soubiran 2001; Prugniel et al. 2007) and MILES (Sánchez-Blázquez et al. 2006; Falcón-Barroso et al. 2011), are now available. They cover a wide range of stellar parameters, accurately determined with high resolution spectroscopy. A pipeline, the LAMOST stellar parameter pipeline (LASP), which is mainly based on the Université de Lyon Spectroscopic Analysis Software (ULySS; Koleva et al. 2009; Wu et al. 2011) and makes use of the ELODIE library, has been developed and applied to the LAMOST spectra at the LAMOST Operation and Development Center of the National Astronomical Observatories of Chinese Academy of Sciences (NAOC; Wu et al. 2014). The library is used to determine radial velocities as well as atmospheric parameters. Parameters thus determined have been made available via the LAMOST official data release (Luo et al. 2012, Bai et al. 2014).

As parts of the LSS-GAC survey, a pipeline, the LAMOST Stellar Parameter Pipeline at Peking University – LSP3, has been developed in parallel. Similar to the LASP, the LSP3 determines stellar atmospheric parameters by template matching, but using the MILES rather than the ELODIE empirical library instead. Compared to the ELODIE spectra which are secured using an echelle spectrograph with a very high spectral resolution ( $R \sim 42,000$ ; Prugniel & Soubiran 2001; Prugniel et al. 2007), the MILES spectra are obtained using a long-slit spectrograph at a spectral resolution ( $\text{FWHM} \sim 2.4 \text{ \AA}$ ) comparable to that of the LAMOST spectra, and are accurately flux-calibrated to an accuracy of a few per cent over the  $\lambda\lambda 3525\text{--}7410$  wavelength coverage. The stellar atmospheric parameters of MILES spectra, determined in most cases using high resolution spectroscopy, have been calibrated to a uniform reference (Cenarro et al. 2007). On the other hand, the radial velocities of MILES stars are not as accurately determined as those in the ELODIE library, given the fairly low spectral resolution of MILES spectra. Thus for radial velocity determinations, the LSP3 continues to make use of the ELODIE library.

The LSP3 has been successfully applied to hundreds of thousands spectra collected for the LSS-GAC survey. Radial velocities and atmospheric parameters, together with other additional param-

<sup>1</sup> <http://pendientedemigracion.ucm.es/info/Astrof/invest/actividad/spectra.html>

eters such as estimates of interstellar extinction and distance to individual stars are released as value-added catalogs supplementary to the LAMOST official data release (Paper III). In this work, we introduce the algorithm and implementation of LSP3 in detail, and examine the accuracy of stellar parameters yielded by the LSP3, by applying the LSP3 to the spectral templates themselves, to LAMOST multi-epoch spectra of duplicate stars and to LAMOST and SDSS spectra of member candidates of open and globular clusters. Parameters yielded by the LSP3 are compared extensively with independent determinations from a number of external databases, including the PASTEL archive and the APOGEE, SDSS and RAVE surveys, as well as with values published in the LAMOST first data releases (DR1; Bai et al. 2014).

The paper is organized as follows. In Section 2, we introduce template libraries adopted by the LSP3. Section 3 describes the methodology of LSP3 in detail. In Section 4, we examine the LSP3 algorithm by applying it to the template spectra themselves. In Section 5, we discuss the precision and accuracy of LSP3 by comparing the results yielded by different algorithms and by multi-epoch observations of duplicate stars. In Section 6, LSP3 stellar parameters are compared extensively with independent determinations from external databases. Calibration and error estimates of LSP3 parameters are presented in Section 7. In Section 8, we discuss the error sources of LSP3 stellar parameters. We close with a summary in Section 9.

## 2 THE SPECTRAL TEMPLATES

### 2.1 The MILES and ELODIE libraries

The MILES library consists of 985 stars spanning wide range of stellar atmospheric parameters. The spectra are obtained with the 2.5 m Issac Newton Telescope, covering the wavelength range 3525 – 7500 Å at an almost constant resolution of full width at half maximum (FWHM) of about 2.5 Å (Sánchez-Blázquez et al. 2006; Falcón-Barroso et al. 2011), which is slightly smaller than the typical FWHM of LAMOST spectra ( $\sim 2.8$  Å). The high accuracy of (relative) flux calibration (Sánchez-Blázquez et al. 2006) and wide coverage of stellar parameters that are homogeneously calibrated (Cenarro et al. 2007) make the MILES an ideal empirical spectral library for stellar parameter determinations. The spectra are converted to match the LAMOST resolution by convolving with Gaussians and resampled to 1.0 Å per pixel. The width of the Gaussian, which is allowed to vary with wavelength, is taken to be the mean of all the 4000 fibers of LAMOST.

The MILES spectra are wavelength-calibrated to an accuracy of only approximately  $10 \text{ km s}^{-1}$ , not good enough for the purpose of radial velocity determinations for the LAMOST spectra. We have thus decided to use the ELODIE library as radial velocity templates. The library contains 1959 high-resolution spectra of 1388 stars, obtained with the ELODIE echelle spectrograph mounted on the Observatoire de Haute-Provence 1.93 m telescope, covering wavelength range 3900 – 6800 Å at a resolving power of 42,000 (Prugniel & Soubiran, 2001; Prugniel et al. 2007). In addition to spectra of the original resolving power, the library also provides another set of spectra, degraded to a resolving power of 10,000. We use the latter set of spectra. The spectra are further degraded in resolution to match that of the LAMOST and resampled to 1.0 Å per pixel. For stars with multiple spectra, only the one flagged as the best is used. Note that both the MILES and ELODIE libraries provide spectra in rest laboratory wavelengths, calculated using radial

velocities determined from the spectra. As a test of the accuracy of radial velocities adopted by the ELODIE, we cross-correlate the spectra with synthetic ones (Munari et al. 2005) of identical stellar atmospheric parameters, and find an average velocity residual and standard deviation of  $-2.8 \pm 0.7 \text{ km s}^{-1}$ . The small value of standard deviation reflects the high resolution of ELODIE spectra and that the spectra are wavelength-calibrated to high a precision. The offset,  $-2.8 \text{ km s}^{-1}$ , is however significant. Its origin is unclear. As shall be shown in Section 6.1, we correct for any systematics in radial velocities determined with the ELODIE by calibrating the results against external databases. For comparison, a similar exercise for the MILES library yields a residual of  $-2.6 \pm 6.5 \text{ km s}^{-1}$ . The above exercise also finds a few spectra in the ELODIE library that have very large velocity residuals. For spectra with residuals in excess of  $3\sigma$  of the mean, we have applied corrections to the wavelengths using the above determined residuals. Finally, given the scarce of stars of temperatures higher than 7000 K, we have added 360 synthetic spectra (Munari et al. 2005) with temperatures between 7000 and 12,000 K to the ELODIE library as radial velocity templates.

### 2.2 Interpolation of spectra

Although the MILES library has a decent coverage of the stellar parameter space, the coverage is not homogeneous and there are clusters and holes in the distribution of stars in the parameter space. Fig. 1 shows the distributions of MILES stars in the  $T_{\text{eff}} - \log g$  and  $T_{\text{eff}} - [\text{Fe}/\text{H}]$  planes. At  $T_{\text{eff}} \sim 5700 \text{ K}$ , for example, a number of stars cluster around  $[\text{Fe}/\text{H}] \sim 0.1$  and  $\sim -0.5$  dex, but few at  $[\text{Fe}/\text{H}] \sim -0.2$  dex. The presence of clusters and holes in the distributions introduces patterns and biases in the resultant stellar atmospheric parameters derived by template matching.

An observational campaign to fill the holes and to further expand the parameter space coverage, as well as to expand the template spectral wavelength coverage to 9200 Å to utilize the full potential of the LAMOST spectra, especially those from the red-arm, is well under way, using the NAOC 2.16 m telescope and the 2.4 m telescope of the Yunnan Astronomical Observatory. As a remedy for the time being, we interpolate the MILES spectra to fill up the apparent holes in parameter space. To do this, we first exclude 85 out of the 985 MILES template stars that do not have a complete set of high quality parameters ( $T_{\text{eff}}$ ,  $\log g$  and  $[\text{Fe}/\text{H}]$ ). Of the 900 stars left, 14 fall close the low  $\log g$  boundaries of the distribution in the  $T_{\text{eff}} - \log g$  plane and are also not used for the interpolation. To interpolate the spectra, the remaining 886 stars are divided into four groups in the  $T_{\text{eff}} - \log g$  plane (Table 1). For each group of stars, a third-order polynomial of 20 coefficients, is used to fit the spectral flux density normalized to unity at 5400 Å at each wavelength as a function of stellar atmospheric parameters,  $T_{\text{eff}}$ ,  $\log g$  and  $[\text{Fe}/\text{H}]$ . Here a third-order polynomial is selected as a compromise considering the fact that stellar spectra are a complicated function of atmospheric parameters and the limited number as well as parameter coverage of the MILES templates.

To examine the uncertainties of interpolated spectra, we have applied the interpolation scheme to the templates themselves. Specifically, we drop a template from the library, and fit the rest with the polynomial. The fit is then used to calculate the dropped spectrum at the given parameters. To characterize the goodness of fit, the dispersion of the relative differences between the interpolated and observed spectra, is calculated between 4320 – 5500 Å, the window the LSP3 adopts for estimating stellar parameters. When calculating the relative differences, the interpolated spec-

**Table 1.** Partition of the MILES stars for spectral interpolation

Group	$T_{\text{eff}}$ (K)	$\log g$ ( $\text{cm s}^{-2}$ )	Number of stars
Dwarfs	4500 – 7500	$> 3.2$	360
Giants	3000 – 5500	$< 3.4$	354
Hot stars	$> 7000$	–	125
Cool dwarfs	$< 5000$	$> 3.2$	51

trum is allowed to scale with a third-order polynomial to match the SED of the observed one. The exercise is repeated for all template in the library. For FGK dwarfs, giants, cool dwarfs and hot stars, the mean and scatter of dispersion thus calculated for all templates in the library are  $0.007 \pm 0.003$ ,  $0.013 \pm 0.007$ ,  $0.023 \pm 0.012$  and  $0.020 \pm 0.010$ , respectively. Fig. 2 compares the interpolated and observed template spectra for four example stars, one from each of the four groups. Compared to typical uncertainties of LAMOST spectra, the errors of interpolated templates due to fitting uncertainties are marginal, except for LAMOST spectra of very high SNRs. We have also tried to interpolate the templates using the formula of Prugniel et al. (2011). The results are generally comparable with each other.

To fill up some of the apparent holes in parameter space covered by the MILES library, some fiducial spectra are created by interpolating the existing templates in parameter space. In total, 416 fiducial spectra are interpolated using the fits generated above and added to the MILES library. The distributions of parameters of the interpolated spectra are over-plotted in Fig. 1 along with those of the original spectra. The resultant parameter coverage in  $T_{\text{eff}} - [\text{Fe}/\text{H}]$  plane, though still not fully homogeneous, is much improved. Finally, for the purpose of spectral classification only, we have added 18 spectra of white dwarfs (WDs), carbon stars and late-M/L type stars retrieved from the SDSS database to the final library of spectral templates used by the LSP3.

### 3 METHODOLOGY

The LSP3 adopts a cross-correlation algorithm to determine stellar radial velocities. For the determinations of stellar atmospheric parameters, LSP3 uses two approaches: the weighted means of parameters of the best-matching templates and values yielded by  $\chi^2$  minimization. Both methods are based on  $\chi^2$  values calculated from the target and matching template spectra.  $\chi^2$  is defined as

$$\chi^2 = \sum_{i=1}^N \frac{(O_i - T_i)^2}{\sigma_i^2} \quad (1)$$

where  $O_i$  and  $T_i$  are respectively flux densities of the target and template spectra of the  $i$ th pixel.  $N$  is the total pixel number used to calculate  $\chi^2$ , and  $\sigma_i$  is the error of flux density of the target spectrum of the  $i$ th pixel. Note that here we have neglected the errors of flux density of the template spectrum. The LSP3 is designed to match the LAMOST blue- and red-arm spectra with templates separately. However, limited by the wavelength coverage of the template spectra, in the current version of LSP3, only results derived from the blue-arm spectra are used.

#### 3.1 Flowchart

Fig. 3 illustrates a flowchart of the LSP3. For a given target spectrum, a set of initial parameters ( $V_r$ ,  $T_{\text{eff}}$ ,  $\log g$ ,  $[\text{Fe}/\text{H}]$ ) are first esti-

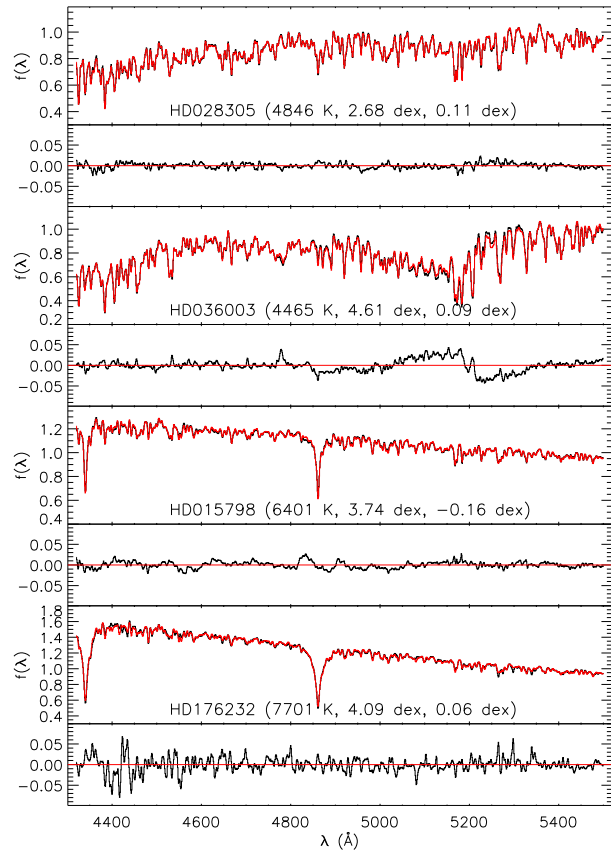


**Figure 2.** Comparison of interpolated (red) and observed (black) MILES template spectra for four example stars, one from each of the four groups of stars listed in Table 1. The flux densities are in arbitrary units. The name and atmospheric parameters (in the sequence of  $T_{\text{eff}}$ ,  $\log g$ ,  $[\text{Fe}/\text{H}]$ ) of the star are marked in each panel. For each star, the residuals between the interpolated and observed spectra are also plotted at the bottom of each panel.

ated by matching the normalized target spectrum with normalized MILES templates (cf. Section 3.3 for detail). A subset of templates that fall in a given parameter box centered on the initial estimates are then selected and scaled to match the spectral energy distribution (SED) with the  $V_r$ -corrected target spectrum to calculate values of  $\chi^2$ . From those  $\chi^2$  values, a new set of atmospheric parameters are estimated by taking the biweight mean values of parameters of the four best-matching templates. Several ELODIE spectra of stellar atmospheric parameters closest to the newly estimated ones, are then selected to determine a revised value of radial velocity using a cross-correlation algorithm. This newly derived radial velocity is then used to convert the target spectrum to laboratory wavelengths and re-calculate values of  $\chi^2$ . This process is iterated until values of  $V_r$  from two consecutive iterations differ by less than a predefined margin (default  $3.0 \text{ km s}^{-1}$  in the current version of LSP3).

Once  $V_r$  has been determined, two algorithms: a) weighted means of parameters of best-matching templates and, b)  $\chi^2$  minimization, are applied to further improve estimates of the target atmospheric parameters. For the weighted mean method, two weights are assigned to each MILES template, one accounts for the degree of similarity between the target and template spectra (i.e. values of  $\chi^2$ ), another accounts for the local density of templates in the  $T_{\text{eff}} - [\text{Fe}/\text{H}]$  plane of the parameter space.  $T_{\text{eff}}$  is first derived since it



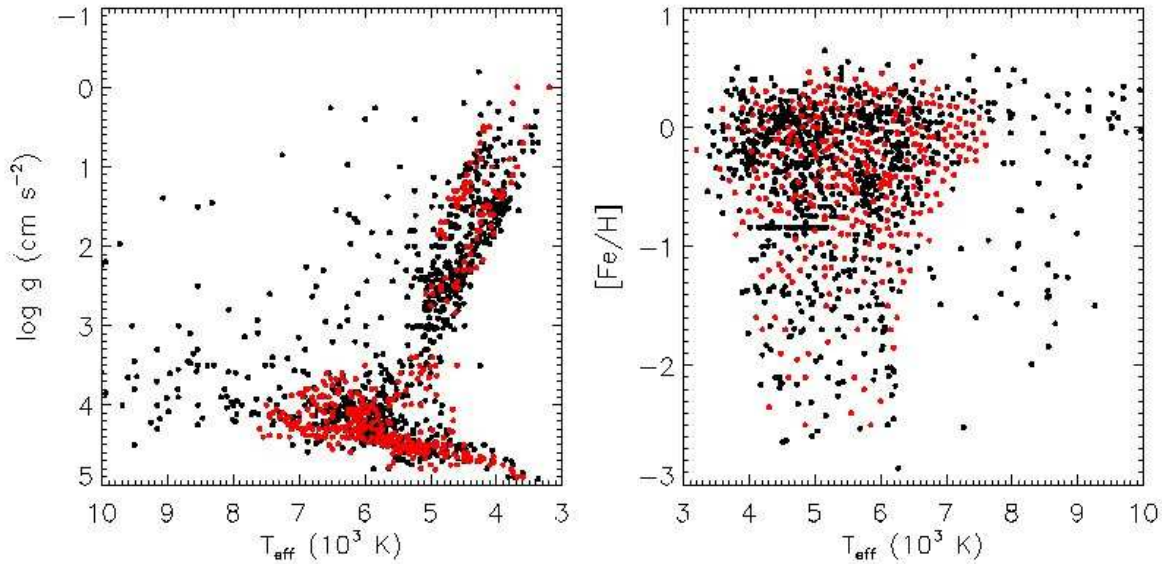


**Figure 1.** Distributions of stellar atmospheric parameter of the MILES spectral templates adopted by the LSP3 in the planes of  $T_{\text{eff}} - \log g$  (left) and  $T_{\text{eff}} - [\text{Fe}/\text{H}]$  (right). Black dots represent the original 900 MILES template spectra, while those in red represent the 416 interpolated spectra.

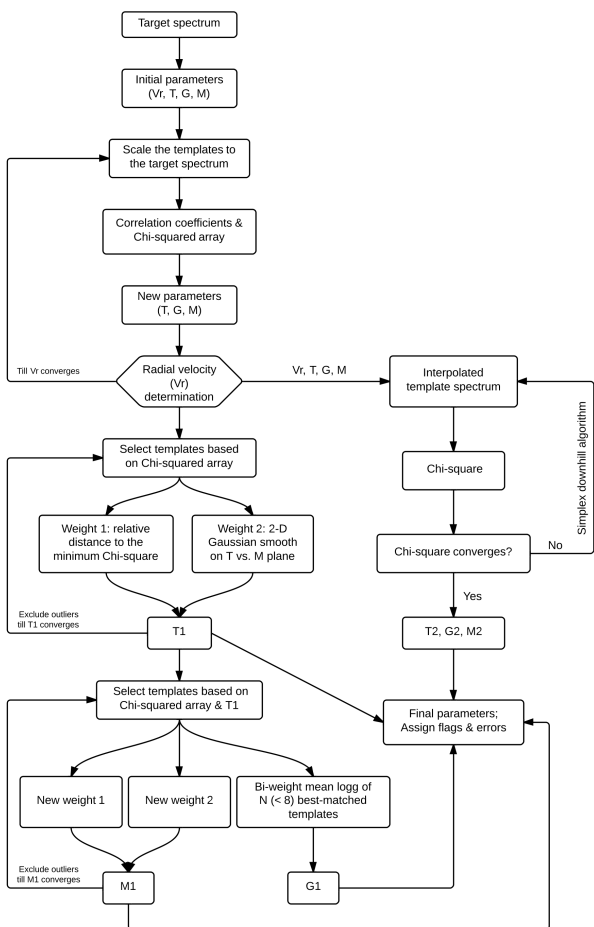


**Figure 3.** LSP3 Flowchart.

is the parameter that  $\chi^2$  is most sensitive to. Values of  $\log g$  and  $[\text{Fe}/\text{H}]$  are then determined using only templates that fall in a narrow (predefined) range of the afore determined value of  $T_{\text{eff}}$ . The processes are iterated to exclude obvious outliers of templates of parameters that deviate significantly from the weighted mean values. For the  $\chi^2$  minimization method, a simplex downhill algorithm (Nelder & Mead 1965) is used to search for the minimum  $\chi^2$  between the  $V_r$ -corrected target spectrum and templates in the parameter space. Note that the template spectrum of a given set of atmospheric parameters is calculated using the fits deduced in Section 2.2. In the current version of LSP3, results derived from the weighted mean method are adopted as the final parameters of the pipeline. Specific flags (cf. Section 3.8) are assigned to each target spectrum analyzed to indicate the quality and/or any warning of the parameters deduced. Errors of the final parameters are estimated by combining the random and systematic errors, and are functions of the SNR,  $T_{\text{eff}}$ ,  $\log g$  and  $[\text{Fe}/\text{H}]$ . Here the random errors are estimated by comparing results derived from multi-epoch observations of duplicate targets, while the systematic errors are derived by applying the LSP3 to the MILES templates.

### 3.2 Selection of matching wavelength range

LAMOST spectra are split with a dichroic into blue and red parts and are collected with two arms, the blue-arm spectra covering 3700 – 5900 Å, and the red spectra covering 5700 – 9000 Å (Cui et al. 2012). The blue- and red-arm raw spectra are processed separately in the LAMOST 2-D pipeline and are pieced together after flux calibration (Xiang et al. 2014, submitted, hereafter Paper I).

The LSP3 is designed to determine stellar parameters with the blue- and red-arm spectra separately, although the current version of LSP3 makes use of the results from the blue-arm spectra only. This approach is based on the following considerations. First, the LSS-GAC targets stars of a wide range of colours, thus depending on the colour, the blue- and red-arm spectra may have very different

signal-to-noise ratios (SNRs). Second, the accuracy of wavelength calibration of the blue- and red-arm spectra are different, since they are calibrated separately and corrected for systematics using different sets of sky emission lines (Luo A.-L., private communication). Finally, the blue- and red-arm spectra sometimes do not piece together smoothly due to uncertainties in flat-fielding, sky subtraction, and flux calibration. The problem is most acute for spectra of low SNRs. There are some rare cases where the current pipeline of flux-calibration fails to yield a reliable set of spectral response curves (SRCs). Spectra of those plates are processed with a nominal set of SRCs (Paper I), leading to large uncertainties in the SEDs of those spectra, in particular around the cross-over wavelength of the dichroic.

As a default, the current version of LSP3 uses the 4320 – 5500 Å wavelength region of the blue-arm spectra to derive stellar parameters. The region is selected in order to exclude the wavelength range beyond 5500 Å where the instrumental sensitivity drops rapidly due to the cutoff of the dichroic, and to avoid prominent atomic lines such as the Ca II H, K lines at 3967 and 3933 Å, often strongly saturated in stars of solar metallicity, and strong molecular absorption bands such as the CH G-band at 4314 Å. Excluding the wavelength region shorter than 4320 Å however does pose some problems, in particular for metal-poor stars, for which the Ca II K line at 3933 Å serves as an important metallicity indicator. Also the Ca I  $\lambda$ 4226 line is an important indicator of the stellar surface gravity (Gray & Corbally, 2009), while the G-band provides information of the [C/Fe] abundance ratios (Lee et al. 2013). As such, an option of matching target spectra with templates over a wider range of wavelengths, from 3900 – 5500 Å, is also implemented in the LSP3. For most targets, stellar parameters derived from the spectral range 4320 – 5500 Å differ little from those from the range of 3900 – 5500 Å. Stellar parameters derived from the 3900 – 5500 Å wavelength range will be presented in the next release of LSP3, along with estimates of  $[\alpha/\text{Fe}]$  and [C/Fe] abundance ratios.

For the red-arm spectra, the spectral range available for template matching is currently limited by the wavelength coverage of MILES spectra that extends only to 7410 Å. An option to determine stellar parameters by matching the 6100 – 6800 Å red-arm spectra is also implemented in the LSP3. However, few spectral features are available in this wavelength regime to constrain the stellar parameters robustly. As such parameters yielded by this option are not provided for the moment. An observational campaign to extend the MILES spectra to 9200 Å is currently in progress (Wang et al. 2014). We expect that the next version of LSP3 will include the wavelength region of the Ca II triplet lines in the red for template matching.

### 3.3 Initial parameters

Good estimates of initial parameters are important for two reasons. Firstly, an initial value of  $V_r$  is needed to convert the observed wavelengths of a target spectrum to laboratory values when calculating the  $\chi^2$  value of the target and matching template spectra. Secondly, the initial values of  $T_{\text{eff}}$ ,  $\log g$  and [Fe/H] are used to limit the parameter range of template spectra in order to reduce the number of templates for  $\chi^2$  calculations and thus to speed up the optimization.

The initial parameters are estimated by matching the continuum-normalized target spectrum with similarly normalized MILES template spectra. To obtain the continuum, the blue- (3900 – 6000 Å) and red-arm (5900 – 9000 Å) spectra are fitted, sep-

arately, with a fifth-order polynomial. The approach is similar to that used in the SSPP (Lee et al. 2008a). Note that continuum-normalized spectra are used to estimate the initial parameters only. When deriving the final parameters, spectra without continuum normalization are used (cf. Section 3.4). The normalized target spectrum is shifted in velocity with discrete values between  $-1000$  and  $1000 \text{ km s}^{-1}$ , at a step of  $10 \text{ km s}^{-1}$  within  $\pm 300 \text{ km s}^{-1}$  and a step of  $50 \text{ km s}^{-1}$  beyond. A Bessel interpolation is adopted to interpolate  $V_r$ -shifted spectra.  $\chi^2$  values and correlation coefficients of the  $V_r$ -shifted target spectrum with all the MILES templates are calculated. To estimate the initial value of  $V_r$ , the template that yields the maximum correlation coefficient is selected out. Then for this template, its correlation coefficient with the target spectrum as a function of velocity is fitted with a Gaussian plus a second-order polynomial to find the exact value of  $V_r$  where the correlation coefficient peaks. In doing so only a few discrete values of velocity shift around the maximum correlation coefficient are used for the fitting. As for the initial values of  $T_{\text{eff}}$ ,  $\log g$  and [Fe/H], we select the 20 templates that give the smallest  $\chi^2$  (at certain discrete value of velocity shift). The biweight means of atmospheric parameters of those 20 best-matching templates are then taken to be the initial parameters of the target spectrum, and the standard deviations of parameters of those templates are adopted as the errors of the initial parameters. Note that 20 is simply an empirical value based on an examination of the distribution of  $\chi^2$ . The final parameters deduced are found to be insensitive to this value given that a large box ( $0.2 \times T_{\text{eff}}$  in  $T_{\text{eff}}$ , 3.0 dex in  $\log g$  and 1.0 dex in [Fe/H]; Section 3.4) is set to re-do the template matching iteratively when estimating the final parameters with the weighted mean algorithm (Section 3.5).

### 3.4 Radial velocity determination and the final $\chi^2$ array

As described in §3.1, an iterative process is implemented to determine radial velocity and atmospheric parameters. It is designed to minimize the effects of uncertainties in  $V_r$  on the calculation of  $\chi^2$  array of the target spectrum with the MILES templates that are used to derive atmospheric parameters on the one hand, and, on the other hand to ensure radial velocity is determined by cross-correlating with an ELODIE template that has atmospheric parameters closest to the target.

Unlike most of the previous work where template matching is carried out using continuum-normalized spectra (e.g. Lee et al. 2008a), the LSP3 uses non-normalized spectra. One reason is that there is important information (in particular that of the effective temperature) encoded in the observed continuum shape (i.e. SED) of a target spectrum. Another reason is that accurate estimate of the continuum level over a wide wavelength range for medium-to-low resolution spectra is often quite difficult, especially for spectra of low SNRs or for stars of late-types whose spectra are dominated by prominent and broad molecular absorption bands. As designed, the LSS-GAC targets include many late-type stars and a significant fraction of the spectra accumulated so far have SNRs lower than 20 per pixel in the blue (3700 – 5900 Å) (cf. Paper III). To account for effects such as reddening by the interstellar dust grains and uncertainties in spectral flux calibration, a low-order polynomial is however allowed to scale the SEDs of template spectra to match that of the target spectrum of concern when calculating values of  $\chi^2$ . Based on extensive tests and tries, we find that a third-order polynomial is high enough to account for possible effects due to reddening and flux calibration for the wavelength ranges of con-

cern (4320 – 5500 Å in the blue and 6100 – 6800 Å in the red), and at the same time low enough to avoid inducing undesired artifacts.

To save computation time, for a given set of initial atmospheric parameters ( $T_{\text{eff}}$ ,  $\log g$  and  $[\text{Fe}/\text{H}]$ ), a 3-D box in the parameter space centered on the initial values and of dimensions 3 times the corresponding errors is defined. To ensure the box contains a sufficiently large number of templates, the box is required to have a minimum side of  $0.2 \times T_{\text{eff}}$ , 3.0 dex and 1.0 dex in the dimension of  $T_{\text{eff}}$ ,  $\log g$  and  $[\text{Fe}/\text{H}]$ , respectively. Typically, a box contains 100 – 500 templates, depending on the initial values of parameters. Values of  $\chi^2$  between the  $V_r$ -corrected target spectrum and the MILES templates of parameters falling inside the box are then calculated, after scaling the SEDs of templates to match that of the target using a third-order polynomial.

From the  $\chi^2$  values of target spectrum with MILES templates, the biweight mean values of parameters of the 4 best matching templates are adopted as the new set of parameters. Five ELODIE spectra that have parameters “closest” to the newly derived set of parameters are then selected and used to determine  $V_r$  by cross-correlation. Here, “closest” is defined by distances in the atmospheric parameter space assuming a distance of 75 K in temperature is equivalent to a distance of 0.1 dex in  $\log g$  or in  $[\text{Fe}/\text{H}]$ . To determine  $V_r$ , we first scale the 5 “nearest” ELODIE spectra to match the SED of the target spectrum using a third-order polynomial, shift the wavelengths in velocities between  $-1000 \text{ km s}^{-1}$  and  $1000 \text{ km s}^{-1}$  with a step of  $5 \text{ km s}^{-1}$ , and then calculate the correlation coefficients between the target and the continuum-rectified, velocity-shifted ELODIE spectra. For the ELODIE template showing the highest correlation, the correlation coefficient as a function of velocity shift is fitted with a Gaussian plus a second-order polynomial to determine the best matching radial velocity.

The above process is iterated until values of  $V_r$  from two consecutive iterations differ by less than  $3.0 \text{ km s}^{-1}$ . Typically, 2 – 3 iterations are sufficient. The final array of  $\chi^2$  values is recorded for a further iteration of atmospheric parameter determinations with a weighted mean method.

### 3.5 Parameters estimated by weighted mean

In this approach, the LSP3 adopts the weighted mean of the atmospheric parameters of a subsample of templates selected based on the  $\chi^2$  array as the parameters of the target spectrum. Considering that  $\chi^2$  has different sensitivity to different parameters, and in general  $\chi^2$  is more sensitive to  $T_{\text{eff}}$  than to  $[\text{Fe}/\text{H}]$  and  $\log g$ , the LSP3 estimates  $T_{\text{eff}}$  first, and then determine  $[\text{Fe}/\text{H}]$  and  $\log g$  within a constrained range of  $T_{\text{eff}}$ .

To define a subsample of templates used to calculate the target parameters using the weighted mean algorithm, we first define a threshold value of  $\chi^2$  such that templates with  $\chi^2 < a\chi_{\text{min}}^2$  are included in the subsample. Here  $a$  is a free parameter, and we require that  $a$  should be large enough to enclose sufficient templates (in terms of both the number and the parameter coverage), yet small enough to exclude those obviously “inappropriate” templates. Here, “inappropriate” means that given the parameters of a template, the probability that the target spectrum has the same parameters is lower than a predefined critical value. Given a degree of freedom ( $\sim 1160$ ) of the blue-arm spectra employed ( $\lambda\lambda 4320 - 5500 \text{ \AA}$ , with the Hg I  $\lambda 4358$  city light emission line masked out), we set  $a = 1.05$ . For the  $\chi^2$  range of concern here, the probability is sensitive to the value of  $\chi^2$ , and the probability decreases almost linearly with increasing  $\chi^2$ . In the cases where only a couple of templates ( $< 10$ ) fall within the aforementioned  $\chi^2$  cut,  $a$  is in-

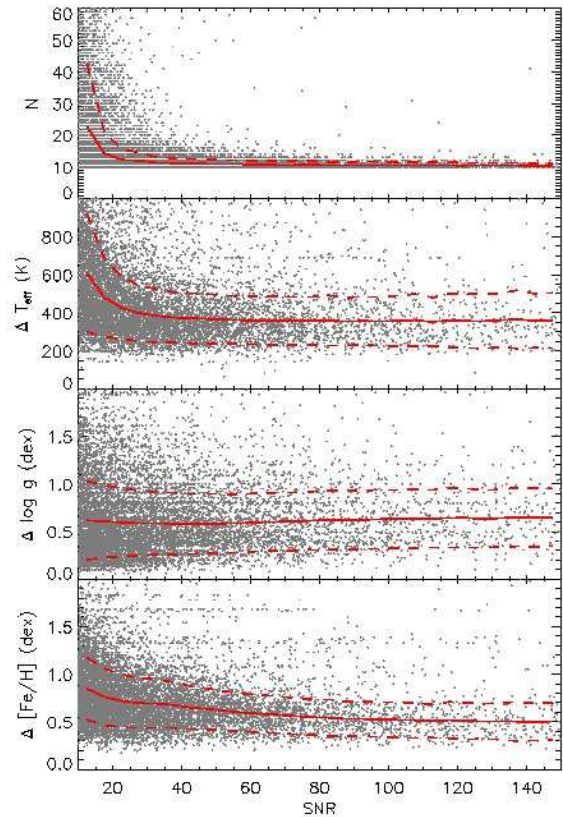


**Figure 4.** Distributions of the number of templates satisfying the  $\chi^2$  cut (top panel), as well as of the spreads (i.e. from the maximum to the minimum) of parameters of those templates in  $T_{\text{eff}}$ ,  $\log g$  and  $[\text{Fe}/\text{H}]$  (lower three panels), as function of the spectral SNR. In each panel, 10,000 stars randomly selected from the current sample are shown. The solid and dashed lines in each panel delineate the mean and the mean plus and minus the standard deviation as a function of the SNR. In the top panel, only the mean and the standard deviation are shown.

creased in order to encompass more ( $\gtrsim 10$ ) templates. Fig. 4 shows the distributions of the number of templates, as well as the spreads of parameters covered by the templates satisfying the  $\chi^2$  cut for the LSS-GAC targets processed with the current version of LSP3. It shows that for most stars about 10 – 20 templates are used to calculate the target parameters using the weighted mean method and the parameters of those templates spread over a range of about 400 K, 0.6 dex and 0.5 dex in  $T_{\text{eff}}$ ,  $\log g$  and  $[\text{Fe}/\text{H}]$ , respectively. Those numbers seem reasonable given the accuracy of parameters achievable with the current design of LSP3 (cf. Sections 5 and 6).

The LSP3 assigns two weights to each template used to calculate the weighted mean parameters. One weight accounts for the degree of similarity between the target and template spectra, defined as

$$w_1 \equiv 1.0 - \frac{\chi^2 - \chi_{\text{min}}^2}{\chi_{\text{max}}^2 - \chi_{\text{min}}^2} \times f. \quad (2)$$

Here  $\chi_{\text{max}}^2$  is the maximum value of  $\chi^2$  of templates in the subsample selected by the aforementioned criteria, and  $f$  is a fudge factor that defines the weight of template with the maximum value of  $\chi^2$ . Note that here we have effectively used a linear relation to replace



the real likelihood distribution, which is proportional to  $\exp(-\chi^2)$ . This is a temporary measure, based on trials and tests, and reflects the fact that, as discussed in Section 8.3, the current error estimates of LAMOST spectra are not reliable, and, consequently, the absolute values of  $\chi^2$ . Nevertheless, a linear relation should be a good approximation to the likelihood distribution for  $\chi^2$  value around 1.0, its most expected value. By this definition, the template having the minimum value of  $\chi^2$  has the highest weight of unity. If one assumes that the minimum value of  $\chi^2$  equals 1.0, the most possible statistical value, then the probability that a given correct model (template) has a value of  $\chi^2$  larger than  $a \times \chi_{\min}^2 = 1.05$  is  $\sim 0.1$  for a degree of freedom of 1160. The probability that a correct model has a  $\chi^2$  value larger than  $\chi_{\min}^2$  is 0.5, half the weight assigned to the template with the minimum  $\chi^2$ . Thus if we take  $f$  to be 0.8, then the template with the maximum  $\chi^2$  will have a weight  $w_1 = 0.2$ . Considering that the parameters of templates themselves have uncertainties, we have decided to give a higher weight to template with the maximum  $\chi^2$  and assign  $f$  as 0.5 in the current version of LSP3.

The second weight,  $w_2$ , accounts for the inhomogeneity of template distribution in the  $T_{\text{eff}} - [\text{Fe}/\text{H}]$  parameter plane. Even though we have interpolated the templates to fill the obvious holes in parameter coverage, local inhomogeneities in parameter space remain. The interpolated spectra are also subjected to interpolation errors. Based on those considerations, we have introduced a Gaussian kernel to smooth the parameters of the selected templates that are used to calculate the stellar parameters in the  $T_{\text{eff}} - [\text{Fe}/\text{H}]$  plane. Firstly, we define a box selection function  $f(T_{\text{eff}}, [\text{Fe}/\text{H}])$  such that  $f = 1$  for templates belonging to the subsample used to calculate the weighted mean parameters, and  $f = 0$  for all other templates. Then weight  $w_2$  for template  $i$  in the subsample is given by,

$$w_2 = \frac{1}{F(T_{\text{eff}}^i, [\text{Fe}/\text{H}]^i)}, \quad (3)$$

where

$$F(T_{\text{eff}}^i, [\text{Fe}/\text{H}]^i) = \sum_{j=1}^N f(T_{\text{eff}}^j, [\text{Fe}/\text{H}]^j) \times g(T_{\text{eff}}^{ji}, [\text{Fe}/\text{H}]^{ji}), \quad (4)$$

$$g(T_{\text{eff}}^{ji}, [\text{Fe}/\text{H}]^{ji}) = \exp\left(-\frac{(T_{\text{eff}}^j - T_{\text{eff}}^i)^2}{2.0\sigma_{T_{\text{eff}}}^2}\right) \times \exp\left(-\frac{([\text{Fe}/\text{H}]^j - [\text{Fe}/\text{H}]^i)^2}{2.0\sigma_{[\text{Fe}/\text{H}]}^2}\right). \quad (5)$$

Here  $N$  is the number of templates in the subsample. In principle, values of  $\sigma_{T_{\text{eff}}}$  and  $\sigma_{[\text{Fe}/\text{H}]}$  should be assigned based on local density of templates in the parameter plane. In the current version of LSP3,  $\sigma_{T_{\text{eff}}}$  and  $\sigma_{[\text{Fe}/\text{H}]}$  are simply assumed to be constants and equal 50 K and 0.05 dex, respectively.

The final weight of a template in the subsample is given by,

$$W = w_1 \times w_2. \quad (6)$$

The weighted mean of temperatures adopted for the target spectrum is thus,

$$T_{\text{eff}} = \frac{\sum_{i=1}^N W^i \times T_{\text{eff}}^i}{\sum_{i=1}^N W^i}. \quad (7)$$

The above process is iterated. In each iteration, templates with values of  $T_{\text{eff}}$  that differs from the weighted mean in excess of two times the standard deviation of the subsample are excluded. Note that the LSP3 always keeps the template with the minimum  $\chi^2$  in the weighting box. If the distance between the weighted mean  $T_{\text{eff}}$  and that of template with the minimum  $\chi^2$ ,  $d_{\min}$ , becomes larger than twice the standard deviation of templates in the box, then templates with  $T_{\text{eff}}$  that differ from the weighted mean by more than  $d_{\min}$  are excluded in the next iteration. Fig. 5 shows an example of this process.

Once  $T_{\text{eff}}$  is determined, the LSP3 selects templates that have  $T_{\text{eff}}$  between  $(1.0 \pm 0.05) \times T_{\text{eff}}$  and  $\chi^2 < a\chi_{\min}^2$  to calculate a weighted mean value of  $[\text{Fe}/\text{H}]$ . The weights of the individual templates are assigned in the same way as for  $T_{\text{eff}}$  estimation discussed above. The estimate adopted for the target spectrum is thus,

$$[\text{Fe}/\text{H}] = \frac{\sum_{i=1}^N (W_{[\text{Fe}/\text{H}]}^i \times [\text{Fe}/\text{H}]^i)}{\sum_{i=1}^N W_{[\text{Fe}/\text{H}]}^i}. \quad (8)$$

For the estimate of  $\log g$ , the LSP3 simply adopts a biweight mean of  $\log g$  of the  $N$  templates that have the highest  $W_{[\text{Fe}/\text{H}]}$ . Here we require  $N \lesssim 8$ . This is because  $\log g$  is usually the parameter that  $\chi^2$  is least sensitive to, and the  $\log g$  values of templates selected with the above  $\chi^2$  cut may spread over a wide range, sometimes even encompassing those of giants and dwarfs. By taking the biweight mean of values of only the few best-matching templates, we avoid the risk of averaging  $\log g$  values of giants and dwarfs. An iteration process similar to that for  $T_{\text{eff}}$  is also applied for the estimates of  $[\text{Fe}/\text{H}]$  and  $\log g$ . Parameters determined with this method are denoted by  $T_{\text{eff}1}$ ,  $\log g_1$ ,  $[\text{Fe}/\text{H}]_1$  for effective temperature, surface gravity and metallicity, respectively.

### 3.6 Parameters estimated by $\chi^2$ minimization

This approach searches for the minimum  $\chi^2$  in the stellar atmospheric parameter space, and adopts the parameters of the template that has the minimum  $\chi^2$  as those of the target. As shown in Fig. 3, the target spectrum is first converted to laboratory wavelengths using  $V_r$  deduced by cross-correlating with templates in the ELODIE library. Taking the biweight means of parameters of the 4 best-matching MILES templates as the initial values, the LSP3 searches the parameter space for the minimum  $\chi^2$  between the  $V_r$ -corrected target spectrum and the MILES templates using a downhill simplex minimization algorithm (Nelder & Mead 1965). Here, the template spectrum for given set of  $T_{\text{eff}}$ ,  $\log g$  and  $[\text{Fe}/\text{H}]$  is created using the parameter – spectra relation deduced by fitting the MILES spectral flux density at each wavelength as a function of stellar atmospheric parameters (cf. Section 2.2). Parameters derived from this method are denoted as  $T_{\text{eff}2}$ ,  $\log g_2$ ,  $[\text{Fe}/\text{H}]_2$  for effective temperature, surface gravity and metallicity, respectively.

### 3.7 The final parameters

Compared with parameters determined by the weighted mean, those deduced by  $\chi^2$  minimization are less affected by the inhomogeneous distribution of MILES templates in the parameter space. However, the parameters derived from the  $\chi^2$  minimization method are affected by the uncertainties of fiducial spectra calculated using the parameter – spectral flux density relations. The uncertainties vary with wavelength and depend on the location of the template



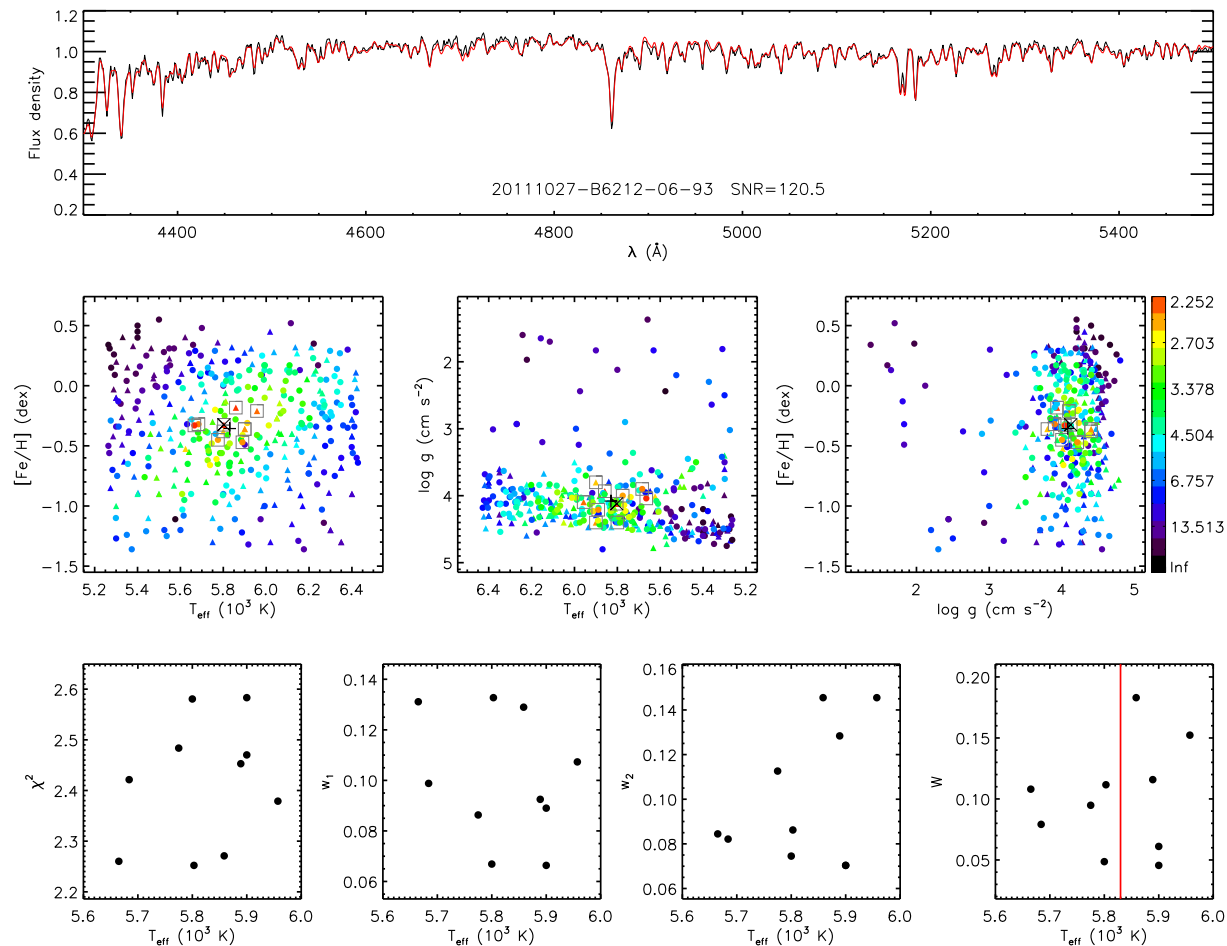


**Figure 5.** An example of estimating  $T_{\text{eff}}$  with the weighted mean algorithm. The top panel plots the target (black) and the best-matching template (red) spectra. The middle panel shows the colour coded distribution of  $\chi^2$  values of the individual templates. Dots represent the original MILES templates and triangles those interpolated. The cross indicates the best-matching template (i.e. the one with the minimum  $\chi^2$ ). Open squares in grey denote templates selected to calculate the weighted mean of parameters, marked by the bold plus. From left to right the three plots show the distributions in the  $T_{\text{eff}} - [\text{Fe}/\text{H}]$ ,  $T_{\text{eff}} - \log g$  and  $\log g - [\text{Fe}/\text{H}]$  plane, respectively. The bottom panel illustrates the process of calculating the weighted mean for  $T_{\text{eff}}$  estimation. From left to right, the four plots are, respectively, values of  $\chi^2$ , normalized  $w_1$ ,  $w_2$  and  $W$  as a function  $T_{\text{eff}}$  for templates in the subsample (weighting box). The red line in the fourth panel indicates the final value of  $T_{\text{eff}}$  adopted. For this particular target spectrum,  $a = 1.18$  (cf. §3.5).

in the parameter space. As shall be shown in Sections 5 and 6, the  $\chi^2$  minimization method yields  $T_{\text{eff}}$  and  $[\text{Fe}/\text{H}]$  with an precision comparable to that of the weighted mean approach. The results for  $\log g$  are inferior, yielding larger scatters compared to those derived by the weighted mean method. Given the nature of  $\chi^2$  minimization method and the complex behaviors of spectral flux density for varying parameters, it is difficult to ensure that the optimization converges to the global minimum rather than a local one, yielding wrong parameters as a consequence. With the above considerations, the current version of LSP3 simply adopts the parameters derived from the weighted mean method,  $T_{\text{eff}1}$ ,  $\log g_1$ ,  $[\text{Fe}/\text{H}]_1$ , as the final parameters of the target spectrum. Parameters given by the  $\chi^2$  minimization method are provided for comparison only, and various flags are assigned based on the degree of discrepancy between the parameters deduced from the two approaches (cf. Section 3.8). Errors of the final parameters are estimated by combining the random errors, estimated by comparing the results yielded by multi-epoch observations of duplicate stars, and the systematic errors, estimated

by applying the LSP3 to the MILES spectra themselves. Clearly, the errors are functions of the spectral SNR,  $T_{\text{eff}}$ ,  $\log g$  and  $[\text{Fe}/\text{H}]$  (cf. Section 7).

### 3.8 Flags

The LSP3 assigns 9 integer flags to the final parameters adopted for each star to mark potential anomalies of the derived values. The flags are listed in Table 2. Except the first one, all other flags are cautionary, and the smaller the values, the higher the quality the parameters derived.

The first flag describes which category of templates the best-matching one (the one with the minimum  $\chi^2$ ) belongs to. The templates are divided into 3 categories: the “normal” templates from the original MILES library, the fiducial templates calculated from the parameter – spectral flux density relations, and the templates of ‘special’ types. The special templates include 18 SDSS templates and 14 MILES templates that fall in specific regions in the  $T_{\text{eff}} -$

**Table 2.** Flags assigned to the final parameters

Flag	Value	Description
1	1, 2, 3	The best-matching template is one of the original MILES spectra (1), a fiducial spectrum calculated from the fitting parameters (2), or a spectrum of special type (3).
2	1, 2, 3...	$\chi_{\min}^2$ larger than the median value of stars in the corresponding SNR, $T_{\text{eff}}$ , $\log g$ and [Fe/H] bins by less than $n \times \text{MAD}^1$ .
3	1, 2, 3...	The peak correlation coefficient smaller than the median value of stars in the corresponding SNR bin by less than $n \times \text{MAD}$ .
4	1, 2, 3...	The final $T_{\text{eff}}$ differs from the value of the best-matching template by less than $n\sigma$ , where $\sigma$ is the estimated error <sup>2</sup> of $T_{\text{eff}}$ .
5	1, 2, 3...	Same as Flag 4 but for $\log g$ .
6	1, 2, 3...	Same as Flag 4 but for [Fe/H].
7	1, 2, 3...	The difference between values of $T_{\text{eff}}$ derived from the weighted mean and $\chi^2$ minimization methods is smaller than $n\sqrt{(\sigma_1^2 + \sigma_2^2)}$ , where $\sigma_1$ and $\sigma_2$ are the estimated errors given by the two methods, respectively.
8	1, 2, 3...	Same as Flag 7 but for $\log g$ .
9	1, 2, 3...	Same as Flag 7 but for [Fe/H].

<sup>1</sup> Mean absolute deviation; <sup>2</sup> See Section 7.

$\log g$  plane as discussed in Section 2.2. The remaining 886 MILES templates are referred to as normal. Depending on the category that the best-matching template belongs to, the LSP3 assigns an integer 1, 2 or 3 to Flag 1. Parameters of stars with Flag 1 = 3 should be treated with caution as the stars may well have a peculiar spectral type (e.g. white dwarfs, carbon stars, late-M/L type stars, BHB stars).

The second flag describes the anomalies of the minimum  $\chi^2$  of the best-matching template. A target spectrum can have an abnormally large  $\chi_{\min}^2$  for a number of reasons, including contamination of cosmic rays, poor background (sky and scattered light) subtraction, incorrect error estimates of spectral flux density, or the star is of some special spectral type that no template in the library can match with. The second flag aims to signal out such possibilities. We divide the LSS-GAC targets observed hitherto into bins of the SNR,  $T_{\text{eff}}$ ,  $\log g$  and [Fe/H], and calculate the median and mean absolute deviation (MAD) of  $\chi_{\min}^2$  values of stars in each bin. Then we construct relations between the median/MAD of  $\chi_{\min}^2$  and the above parameters (SNR,  $T_{\text{eff}}$ ,  $\log g$  and [Fe/H]) by linear interpolation. For a star of a given set of SNR,  $T_{\text{eff}}$ ,  $\log g$  and [Fe/H], if  $\chi_{\min}^2$  is larger than the median value by less than  $n \times \text{MAD}$  predicted by the relations, then the LSP3 assigns an integer  $n$  to the second flag of that star. Note that a lower limit of 1 is set to  $n$  for all the 9 flags.

The third flag describes the correlation coefficient for  $V_r$  estimation. We construct a relation between the median/MAD values of peak correlation coefficients for  $V_r$  estimation and the spectral SNR. For a star of given SNR, if the peak correlation coefficient is smaller than the median value by less than  $n \times \text{MAD}$  predicted by the relation, the LSP3 assigns an integer  $n$  to the third flag of that star.

Flags 4 to 6 describe the differences between the final parameters and the parameters of the best-matching template, for  $T_{\text{eff}}$ ,  $\log g$  and [Fe/H], respectively. If the difference is  $n$  times smaller than the estimated uncertainty of the parameter concerned (cf. Section 7), the LSP3 assigns an integer  $n$  to the corresponding flag.

Flags 7 to 9 describe the difference between the parameters derived from the weighted mean and from the  $\chi^2$  minimization methods, for  $T_{\text{eff}}$ ,  $\log g$  and [Fe/H], respectively. Let  $\Delta X$  denote the

difference of a given parameter, where  $X$  represents  $T_{\text{eff}}$ ,  $\log g$  or [Fe/H]. If  $\Delta X < n\sqrt{\sigma_1^2 + \sigma_2^2}$ , then the LSP3 assigns an integer  $n$  to the corresponding flag. Here  $\sigma_1$  and  $\sigma_2$  are the estimated uncertainties of parameter yielded by the two methods, respectively.

#### 4 TEST WITH THE MILES LIBRARY

We apply the LSP3 to the MILES template spectra to quantify the intrinsic errors of the algorithms. Fig. 6 plots the comparison of the LSP3 results deduced from the weighted mean algorithms with parameters from the MILES library. The upper panels shows the distributions of the parameter differences, and the low panels are direct comparisons in the 2-D parameter planes. An overall dispersion of 87 K, 0.19 dex and 0.13 dex for  $T_{\text{eff}}$ ,  $\log g$  and [Fe/H] respectively, is found for the original MILES spectra, while as for those interpolated spectra the corresponding values are much smaller, about 38 K, 0.14 dex, 0.07 dex. Both errors in the MILES parameters themselves and those introduced by the LSP3 algorithms contribute to those values, and they are the lower limits of errors of the LSP3 parameters.

In the upper middle panel of Fig. 6, there is a non-Gaussian tail in the distribution of differences of  $\log g$ . The values of  $\log g$  for stars in the tail could be systematically overestimated by as much as 0.5 dex or more. Those stars correspond to data points connected by long arrows in the bottom left panel, and are mostly F/G-type subgiants/giants/supergiants of  $\log g < 3.0$  dex or subgiants/turn-off stars of  $\log g$  slightly larger than 3.0 dex. Their values of  $\log g$  have been overestimated by the LSP3 due to the boundary effects of the weighted mean algorithm: near the boundary of parameter coverage of the library, the weighted mean algorithm tend to yield parameters that are biased toward the ‘inner’ region of the parameter coverage where most of the templates fall. Such systematic effects are primary defects of the current LSP3. The ‘gaps’ seen in the deduced values of  $\log g$  presented in Figs. 17, 18 and 21 are probably partly due to such boundary effect. Some similar but weaker ( $\sim 0.1$  dex) boundary effects may also be present in the case of [Fe/H] values deduced for super-metal-rich stars. Currently, we are carrying out a

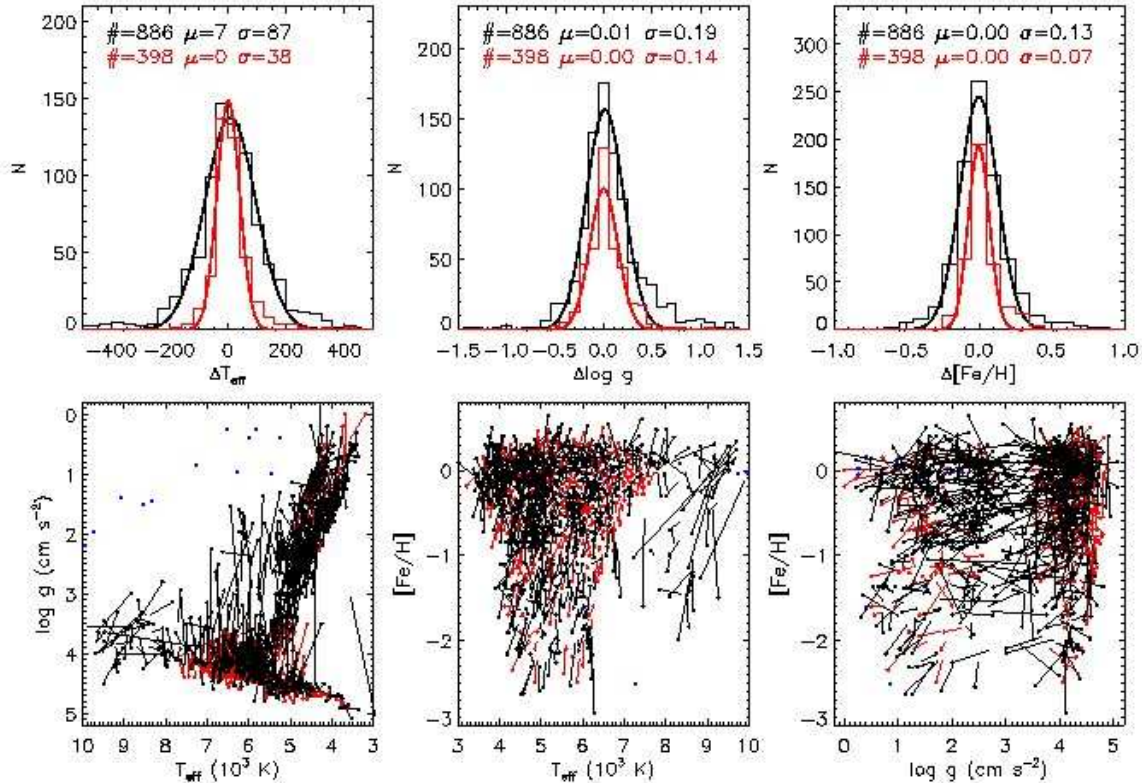


**Figure 6.** The upper panels plot distributions of differences between the parameters yielded by the LSP3 with the weighted mean algorithm and those from the MILES library. Also over-plotted are Gaussian fits to the distributions. The number of templates, the mean and dispersion of the Gaussian fit are marked. The lower panels connect the parameters yielded by the LSP3 and those from the library by lines in 2-D parameter planes, with those from the LSP3 marked by arrows and those from the library by dots. Again, black and red symbols/lines refer respectively to the original MILES and the ‘interpolated’ templates, whereas blue dots denote templates of special spectral types (cf. Section 2.2).

large campaign to expand the extent and homogeneity of parameter coverage of the MILES template library (Wang et al., in preparation).

A similar examination shows that the  $\chi^2$  minimization approach yields results comparable to those from the weighted mean algorithm. Note the  $\chi^2$  minimization method is sensitive to the initial values assigned. As described in Section 3.5, the LSP3 adopts the biweight means of parameters of the 4 best-matching templates as the initial values. Tests show that if we simply assign the initial values to those of the best-matching template, we get significantly different results for some stars, presumably for those stars  $\chi^2$  converges to some local rather than the global minimum, a potential risk inherent to the method.

## 5 PRECISIONS AND UNCERTAINTIES OF THE LSP3 ALGORITHMS

Preceded by one-year-long Pilot Surveys, the LAMOST Regular Surveys were initiated in October 2012. By June 2013, 1.8 million spectra of about 1.3 million LSS-GAC targets have been collected in total, with 750,867 (1,042,586) spectra having SNR in the blue (red) higher than 10 (Liu et al. 2014; Paper III). For spectra with an median SNR per pixel better than 3, parameters  $V_r$ ,  $T_{\text{eff}}$ ,  $\log g$  and  $[\text{Fe}/\text{H}]$  are determined with the LSP3. Unless specified otherwise, the SNRs are calculated per pixel in a wavelength range of 100 Å centered at 4650 Å, where one pixel corresponds to  $\sim 1.07$  Å. Fig. 7

shows example LSS-GAC spectra of SNRs between 10 and 15. Also over-plotted in the Figure are the best-matching template spectra for the wavelength range 4320–5500 Å. The spectral flux densities are plotted in arbitrary scale, and a third-order polynomial is allowed to correct for the SED differences between the LSS-GAC and template spectra. In this Section, we investigate the precision of LSP3 parameters by comparing the results yielded by different algorithms (Section 5.1) as well as by comparing parameters deduced from multi-epoch observations of duplicate targets (Section 5.2).

### 5.1 The weighted mean versus the $\chi^2$ minimization methods

As described in Section 3, the LSP3 determines stellar atmospheric parameters with two methods: the weighted mean ( $T_{\text{eff}1}$ ,  $\log g_1$ ,  $[\text{Fe}/\text{H}]_1$ ) and the  $\chi^2$  minimization ( $T_{\text{eff}2}$ ,  $\log g_2$ ,  $[\text{Fe}/\text{H}]_2$ ). Fig. 8 compares the distributions of parameters derived with the two methods in the  $T_{\text{eff}} - \log g$ ,  $T_{\text{eff}} - [\text{Fe}/\text{H}]$  and  $V_r - [\text{Fe}/\text{H}]$  planes. Note that only parameters derived from spectra of SNRs  $> 5$  are shown in the Figure. The SNR cut leads 1,091,301 spectra of 869,741 stars.

In Fig. 8, in the two panels of plot in the  $T_{\text{eff}} - \log g$  plane (the HR diagram), a Dartmouth isochrone (Dotter et al. 2008) of age 5 Gyr, metallicity  $[\text{Fe}/\text{H}] = -0.2$  dex and  $\alpha$ -element to iron ratio  $[\alpha/\text{Fe}] = 0.0$  dex is over-plotted. Fig. 8 shows that on the whole the weighted mean algorithm yields parameters in good agreement with the isochrone. At a given  $T_{\text{eff}}$ , the  $\chi^2$  minimization method yields a  $\log g$  distribution that looks ‘fatter’ than the weighted



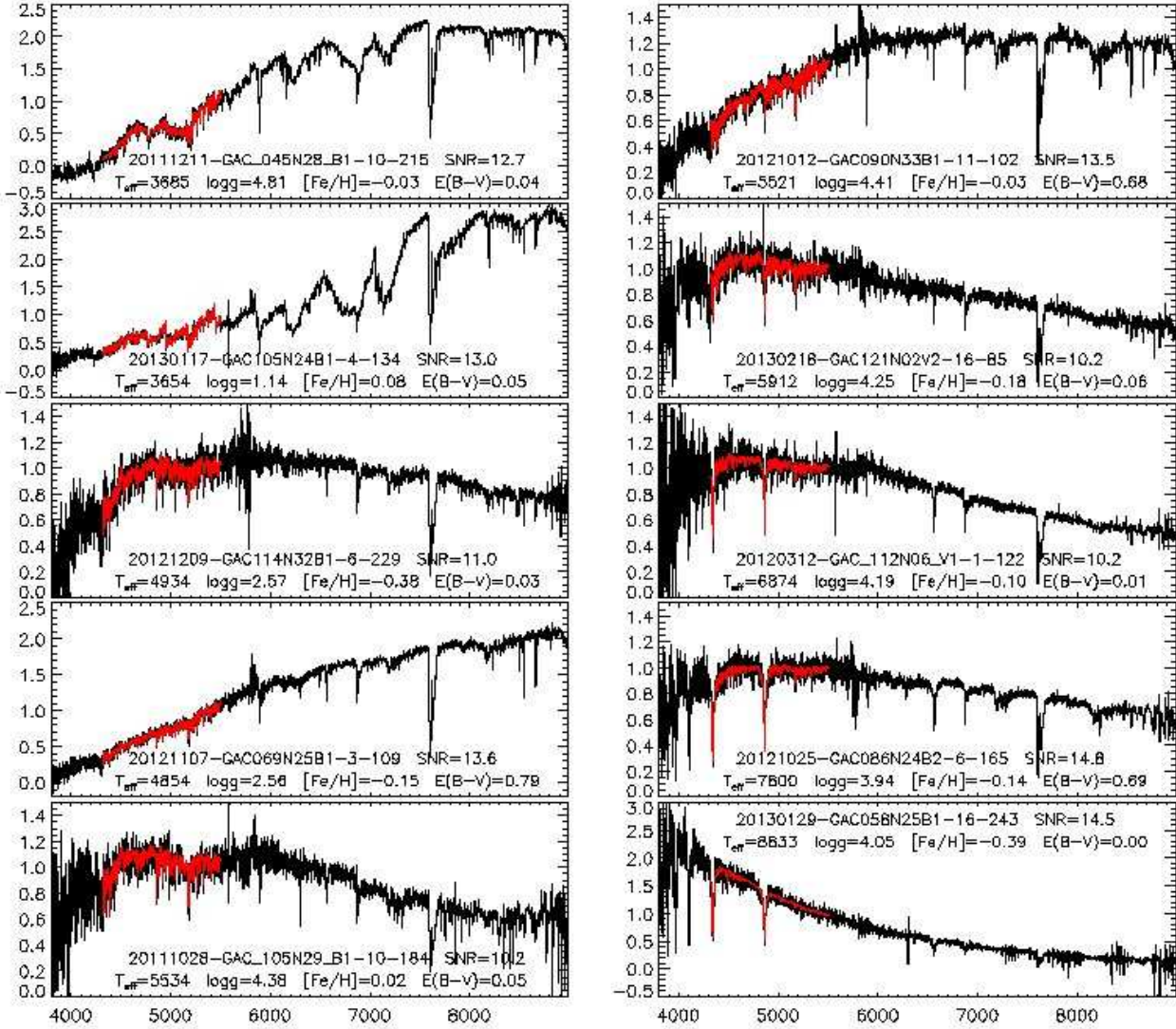


**Figure 7.** Examples of LSS-GAC spectra (black) of SNR between 10 and 15. Also over-plotted spectra in red are the best-matching template spectra for the wavelength range of 4320–5500 Å. The spectral flux densities are plotted in arbitrary scale. The LSS-GAC spectral ID (‘date-plate-spec-fiber’), SNR, LSP3 stellar atmospheric parameters ( $T_{\text{eff}}$ ,  $\log g$ ,  $[\text{Fe}/\text{H}]$ ), as well as reddening  $E(B - V)$  from Yuan et al. (2014b) are marked.

mean algorithm, largely a consequence of the employment of extrapolated templates in the former approach. For dwarfs of effective temperatures between 4800 and 7500 K, values of  $\log g_2$  are probably over-estimated by  $\sim 0.2$  dex. An artificial feature (“branch”) of decreasing  $\log g$  with decreasing  $T_{\text{eff}}$  is also seen for dwarfs between 4400 and 5000 K, as well as around 6000 K. The systematic overestimation of  $\log g_2$ , as well as the artifact branches, are likely caused by uncertainties in the fiducial templates calculated using the fitted parameter – spectral flux density relations (cf. Sections 2.2 and 3.6). In fact, a similar but more significant artificial branch of dwarf stars of  $T_{\text{eff}} < 4800$  K is also seen in the HR diagram constructed using the adopted parameters of SDSS DR9, presumably a consequence of the usage of synthetic spectra by the SSPP in the analysis of those late type stars.

In the  $T_{\text{eff}} - [\text{Fe}/\text{H}]$  plots of Fig. 8, only stars of effective temperatures between 3400 and 7600 K are shown. Overall the distri-

butions from the two methods resemble each other. The  $\chi^2$  minimization gives slightly smoother distribution than the weighted mean, in particular near the edge of the distributions. Again, this is a natural consequence of using the extrapolated templates in the  $\chi^2$  minimization method. For stars of  $T_{\text{eff}1}$  hotter than 7600 K, values of  $[\text{Fe}/\text{H}]$  yielded by the current pipeline are probably unreliable and better calibration is needed for those hot stars (cf. Section 6.7).

A direct comparison of parameters derived from the two algorithms is shown in Fig. 9. Here only results derived from spectra of SNRs better than 10 are shown. Fig. 9 shows that on the whole values of  $T_{\text{eff}}$  yielded by the two methods are consistent with each other, with an overall dispersion of 77 K and negligible systematic differences. However, for stars of  $T_{\text{eff}1} > 7500$  K, values of  $T_{\text{eff}2}$  are a few hundred Kelvin systematically lower than  $T_{\text{eff}1}$ . For  $\log g$ , while there are no significant overall differences, there are clear systematic patterns of differences. We believe that those pat-

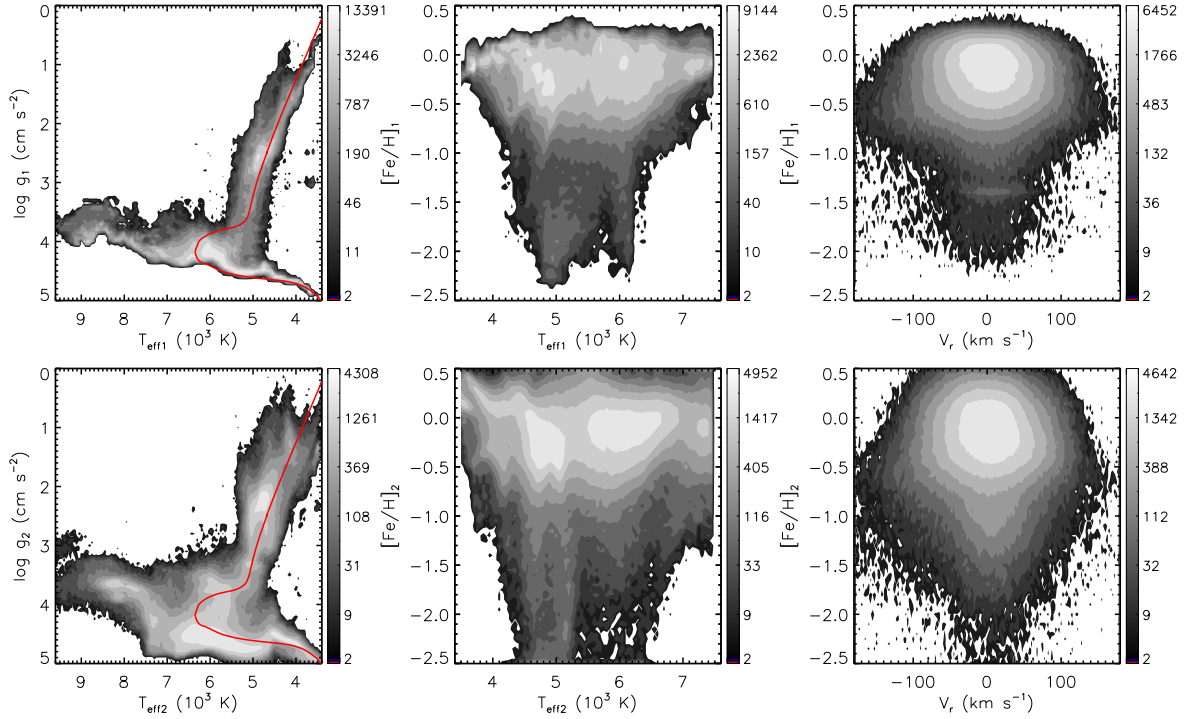


**Figure 8.** Contour distributions of LSP3 parameters derived from the weighted mean (upper panels) and from the  $\chi^2$  minimization (lower panels) methods. The plots include parameters deduced from 1,091,301 spectra of SNRs  $> 5$  for 869,741 stars. The isochrones plotted in the  $T_{\text{eff1}} - \log g$  planes are from Dotter et al. (2008), and have an age of 5 Gyr,  $[\text{Fe}/\text{H}]$  of  $-0.2$  dex and  $[\alpha/\text{Fe}]$  of 0.0 dex.

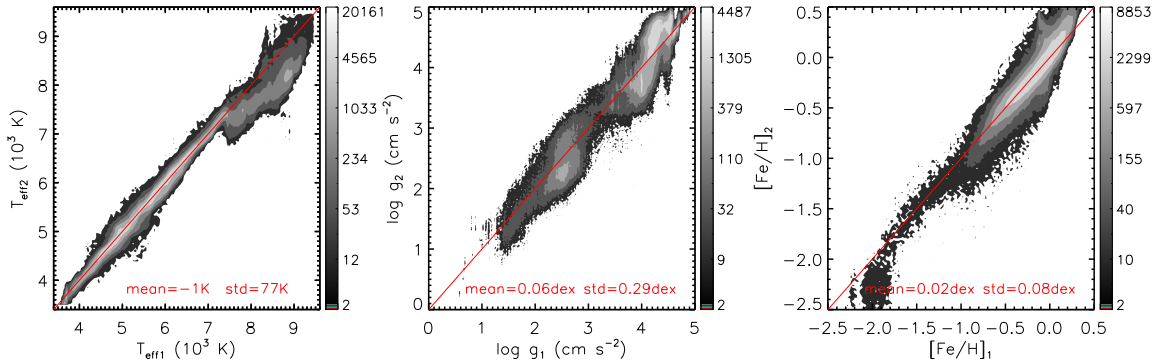


**Figure 9.** Comparison of stellar atmospheric parameters derived with the weighted mean and the  $\chi^2$  minimization algorithms. The mean and standard deviation of the differences are marked in each panel.

terns are mostly likely caused by the problematic values of  $\log g$  yielded by the  $\chi^2$  minimization method, as discussed above. For  $[\text{Fe}/\text{H}]$ , only results of stars of  $T_{\text{eff1}}$  between 3500 and 7500 K are compared. Values of  $[\text{Fe}/\text{H}]_1$  and  $[\text{Fe}/\text{H}]_2$  agree with each other very well, with a mean and standard deviation of differences of  $0.02 \pm 0.08$  dex. There are some evidence that for some stars of super-solar metallicity,  $[\text{Fe}/\text{H}]_1$  is  $\sim 0.1$  dex lower than  $[\text{Fe}/\text{H}]_2$ . This is probably caused by some weak boundary effects of the weighted mean algorithm.

Given that the  $\chi^2$  minimization method yields erroneous values of  $\log g$ , probably due to the inadequacies of the parameter – spectral flux density relations used to interpolate (and extrapolate) templates, the current version of LSP3 has adopted the stellar atmo-

spheric parameters derived from the weighted mean method,  $T_{\text{eff1}}$ ,  $\log g_1$  and  $[\text{Fe}/\text{H}]_1$  as the final estimates of parameters  $T_{\text{eff}}$ ,  $\log g$  and  $[\text{Fe}/\text{H}]$ . Values of  $T_{\text{eff2}}$ ,  $\log g_2$  and  $[\text{Fe}/\text{H}]_2$  are provided for comparison only. Flags are however assigned to reflect the magnitudes of differences between the two sets of parameters derived respectively with the two algorithms (cf. Section 3.8).

## 5.2 Comparison of results from multi-epoch duplicate observations

Owing to the overlapping of FoVs of adjacent plates, about 23 percent stars are targeted more than once in the LSS-GAC survey (Liu

et al. 2014). The number of stars with duplicate observations is further enlarged by repeated observations, either because the original observations failed to pass the quality control (60 per cent of the targeted sources meet the SNR requirements), or for some other reasons (cf. Paper III). Those multi-epoch observations of duplicate targets provide an opportunity to test the precision of parameters delivered by the LSP3 at different SNRs and for stars located at different positions in the parameter space.

To investigate the parameter precision, we first select spectra of duplicate stars obtained at different nights that have similar SNRs, and compare the stellar parameters yielded by the LSP3 as a function of the SNR for stars of different  $T_{\text{eff}}$ ,  $\log g$  and  $[\text{Fe}/\text{H}]$ . The results are presented in Figs. 10 – 13, which plot the precisions, i.e., the dispersions of parameters deduced from the two epoch observations divided by square root of two, as a function of the SNR. In the plots stars are grouped into bins of different temperatures and metallicities, as well as into dwarfs and giants. Note that unless specified otherwise, all stellar atmospheric parameters presented hereafter refer to the final adopted values, i.e. those derived from the weighted mean method (cf. Section 5.1).

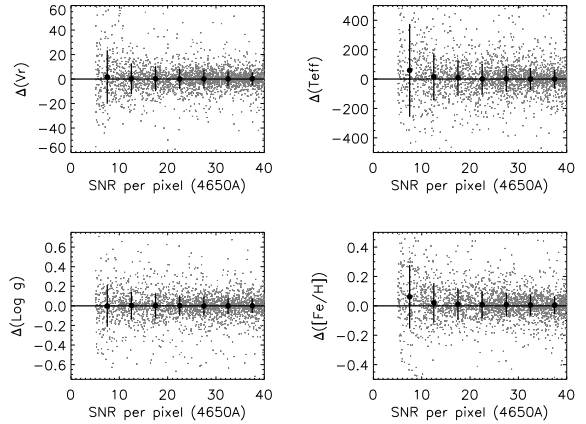
Fig. 10 shows that the precision of  $V_r$  is a steep function of the SNR and  $T_{\text{eff}}$ , but depends only moderately on  $[\text{Fe}/\text{H}]$ . Cooler or more metal-rich stars have better precision. For stars of  $T_{\text{eff}} < 6000$  K and  $[\text{Fe}/\text{H}] > -0.6$  dex,  $V_r$  can be determined to a precision of  $5 \text{ km s}^{-1}$  at a SNR of  $\sim 15$  and  $\sim 7.0 \text{ km s}^{-1}$  at a SNR of  $\sim 10$ . For stars of  $T_{\text{eff}} < 6000$  K but  $[\text{Fe}/\text{H}] < -0.6$  dex, the corresponding value at a SNR of  $\sim 10$  is about  $10 \text{ km s}^{-1}$ . For hot dwarfs of  $T_{\text{eff}}$  between 7000 and 9000 K, the precision decreases to  $\sim 20$  and  $15 \text{ km s}^{-1}$  at a SNR of  $\sim 15$  and 20, respectively.

Fig. 11 shows that the precision of  $T_{\text{eff}}$  are mainly sensitive to the SNR and  $T_{\text{eff}}$ . In general, except for metal-poor giants, the precision of  $T_{\text{eff}}$  is better than 120 K at a SNR higher than 10 for  $T_{\text{eff}} < 7000$  K. For metal-poor ( $[\text{Fe}/\text{H}] < -0.6$  dex) giants of  $T_{\text{eff}} < 7000$  K, the precision is about 200 K. For the hot, metal-poor stars, the precision is visibly worse.

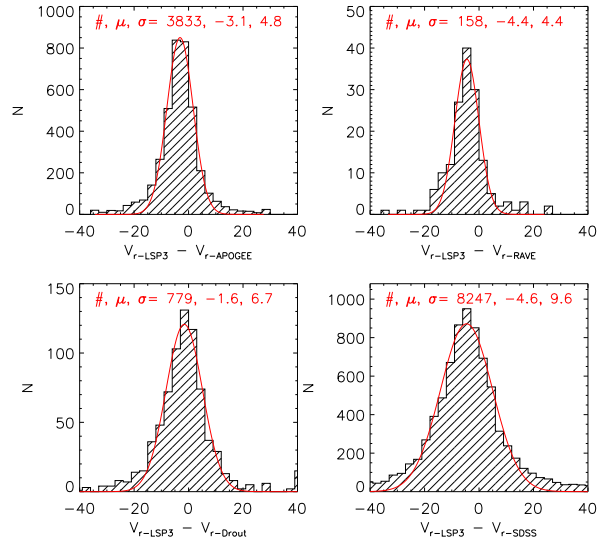
Fig. 12 shows that the precision of  $\log g$  is most sensitive to the SNR and  $\log g$ , but also has some dependence on  $T_{\text{eff}}$ . The precision is higher for dwarfs than for giants. For dwarfs of SNRs better than 10, the precision ranges from 0.05 to 0.1 dex, depending on  $T_{\text{eff}}$ . For giants, the precision ranges from 0.2 to 0.4 dex at a SNR of  $\sim 10$  and becomes better than 0.2 dex at a SNR of  $\sim 15$  for metal-rich stars of  $T_{\text{eff}} < 5000$  K.

Fig. 13 shows that the  $[\text{Fe}/\text{H}]$  precision is sensitive to the SNR and  $[\text{Fe}/\text{H}]$ , and to a less degree to  $T_{\text{eff}}$ . For stars of  $[\text{Fe}/\text{H}] > -0.6$  dex, the precision is better than 0.1 dex when the SNR is about 10. For metal-poor ( $[\text{Fe}/\text{H}] < -0.6$  dex) stars, the precision decreases to  $\sim 0.15$  dex for dwarfs and 0.2 dex for giants at a SNR of better than 10. Again, hot, metal-poor stars have poor precision.

To examine the possible systematic errors introduced by low SNRs, we compare parameters deduced from spectra of duplicate targets obtained at different epochs but having different SNRs. We require that the spectrum of higher quality has a SNR better than 40. Fig. 14 plots the differences of parameters deduced from the two epoch observations as a function of the SNR of the spectrum of lower quality. Fig. 14 shows that as long as the SNR of the lower quality spectrum is better than 15, there are no systematic errors induced by the limited SNR of the lower quality spectrum. This is true for the four parameters. At lower SNRs, systematic errors occur for  $T_{\text{eff}}$  and  $[\text{Fe}/\text{H}]$ , in the sense that the spectra of lower SNRs yields higher values of  $T_{\text{eff}}$  and  $[\text{Fe}/\text{H}]$ . At a SNR of  $\sim 7.5$ , the systematic errors are about 50 K and 0.05 dex for  $T_{\text{eff}}$  and  $[\text{Fe}/\text{H}]$ , respectively.



**Figure 14.** Differences of parameters deduced from two duplicate observations of very different SNRs as a function of the SNR of the spectrum of lower quality. The spectrum of higher SNR has SNR better than 40 per pixel. The differences refer to parameters derived from the spectra of lower SNRs minus those from the spectra of higher SNRs. The means (black dots) and standard deviations (vertical error bars) for the individual bins of SNR are also shown.



**Figure 15.** Histograms of differences of radial velocities of common stars derived from the LAMOST spectra with the LSP3 and those given by the APOGEE (upper left) and by the RAVE surveys (upper right), those from Drouot et al. (bottom left) and from the SDSS survey (bottom right). Overplotted in red are Gaussian fits to the distributions, with the mean and dispersion of the Gaussian marked in each panel.

## 6 COMPARISON OF THE LSP3 PARAMETERS WITH EXTERNAL DATABASES

### 6.1 Radial velocities

To examine the accuracy of LSP3 radial velocities, we compare them with measurements from a number of independent surveys, including the APOGEE (Ahn et al. 2013), RAVE (Steinmetz et al. 2006), and SEGUE (Yanny et al. 2009).

The APOGEE survey collects near-infrared ( $1.514 - 1.696 \mu\text{m}$ ) spectra with a resolving power  $R \sim 22,500$  (Majewski



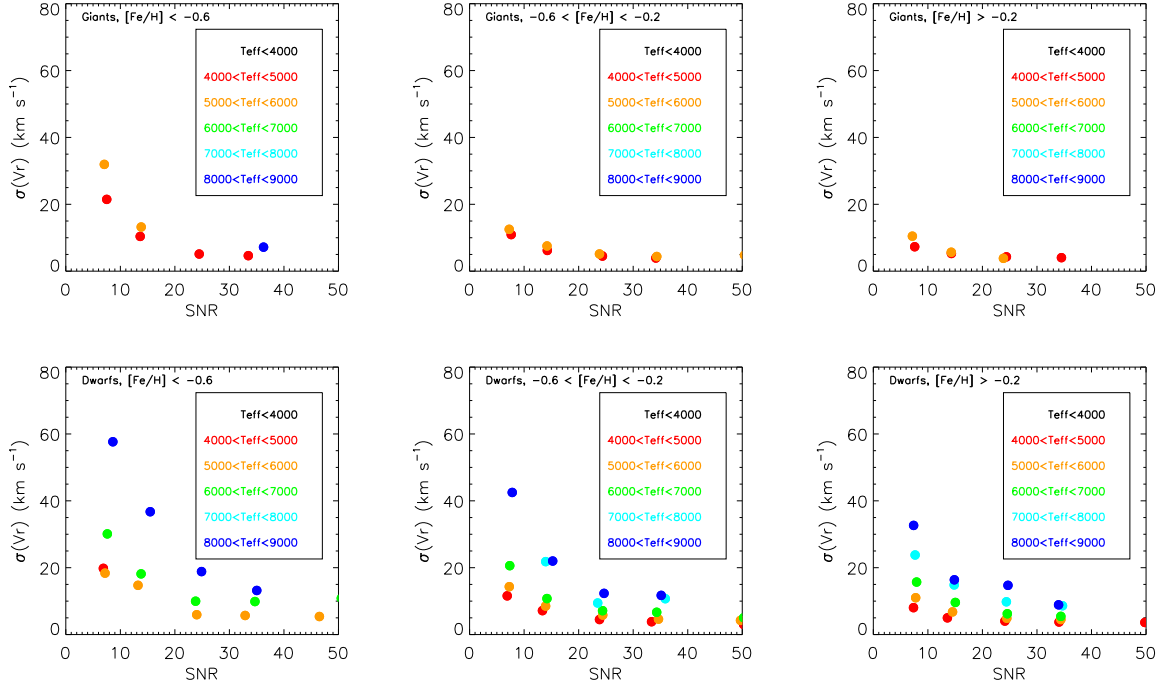


**Figure 10.** Precision of radial velocity determinations, estimated by comparing results yielded by duplicate observations of similar SNRs, as a function of the SNR. Stars are grouped into different bins of  $T_{\text{eff}}$  (colour-coded),  $[\text{Fe}/\text{H}]$  (different columns) and into giants [ $\log g < 3.5$  ( $\text{cm s}^{-2}$ ); upper row] and dwarfs [ $\log g \geq 3.5$  ( $\text{cm s}^{-2}$ ); lower rows].

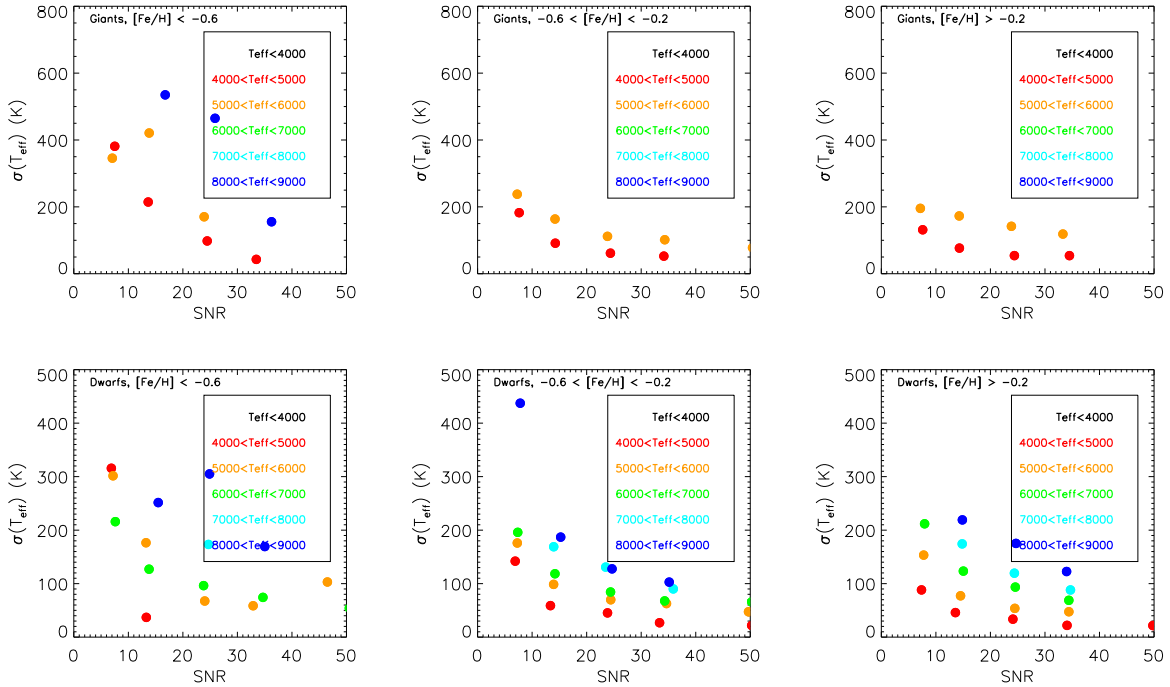


**Figure 11.** Same as Fig. 10 but for  $T_{\text{eff}}$ .

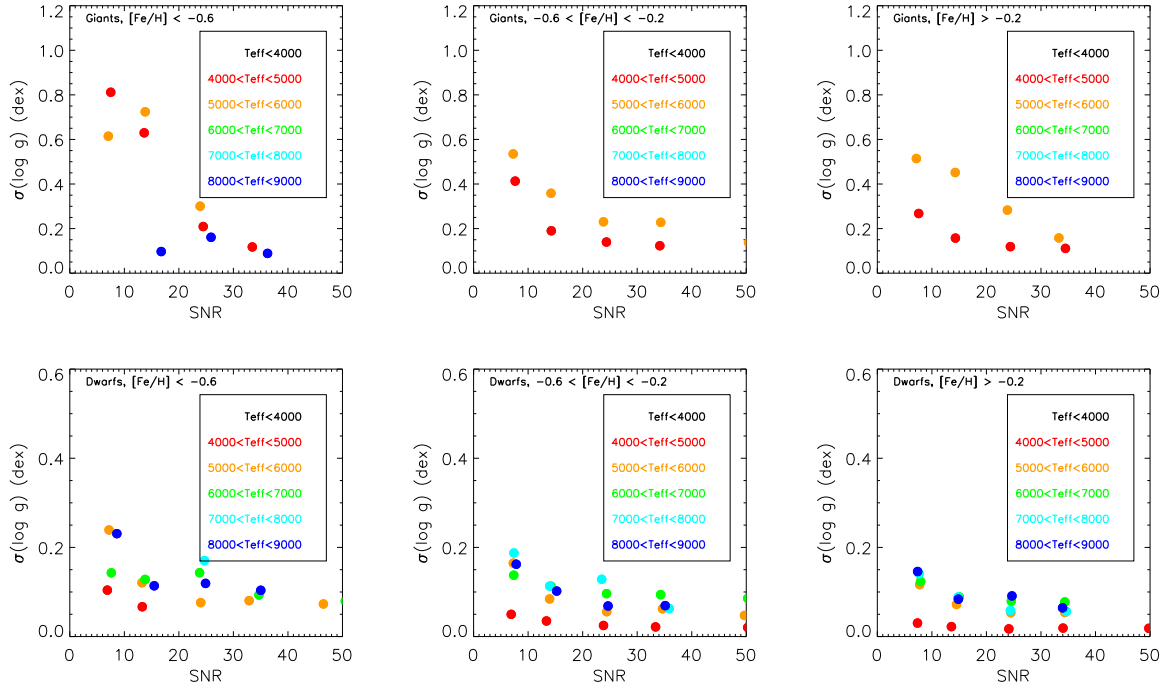


Figure 12. Same as Fig. 10 but for  $\log g$ .

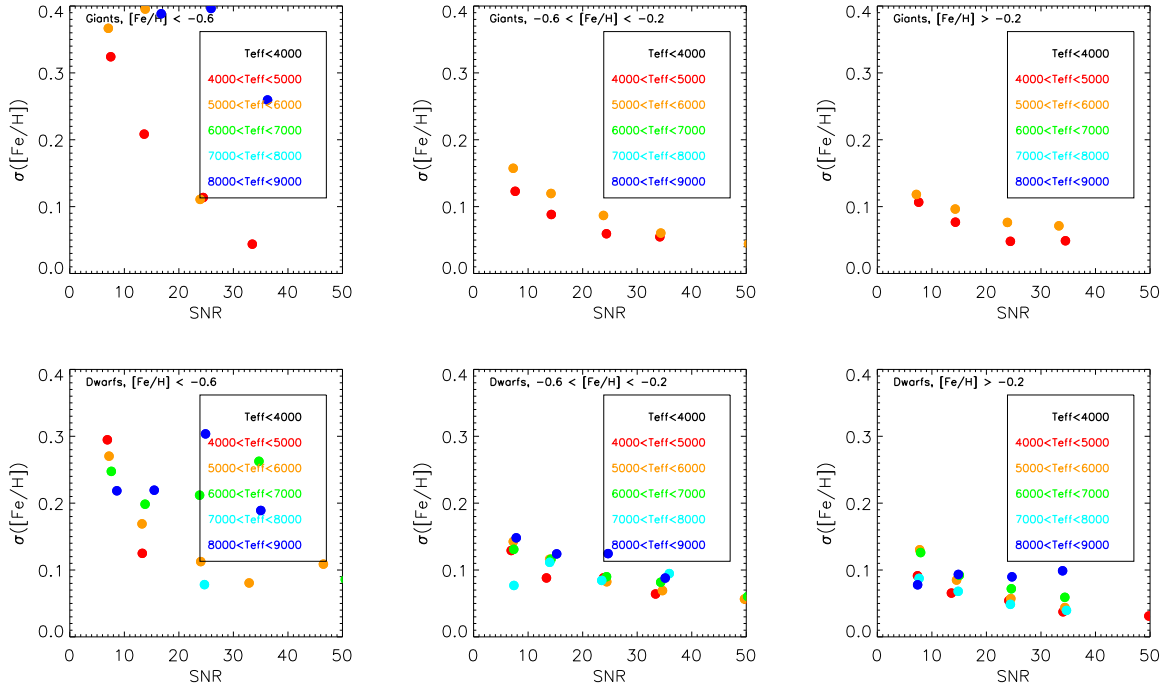
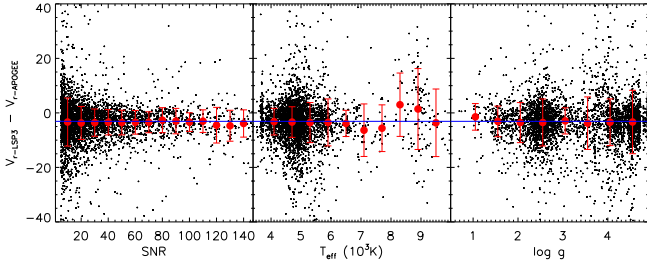


Figure 13. Same as Fig. 10 but for  $[\text{Fe}/\text{H}]$ .

et al. 2010; Ahn et al. 2013). Radial velocities of 57,454 stars have been released in the SDSS DR10, with a typical accuracy of  $\sim 100 \text{ m s}^{-1}$  (Ahn et al. 2013). We have cross-identified our sample with that of the APOGEE, and found 4009 LAMOST spectra of 3035 stars in common after discarding those of SNRs  $< 5$

in our sample. Note that for the comparison we have excluded 176 stars with radial velocities differing from the corresponding APOGEE values by more than  $40 \text{ km s}^{-1}$ . The origin of those large differences is unclear. However, it is found that for most of those stars, the templates for radial velocity determinations used by



**Figure 16.** The radial velocity difference between the LSP3 and the APOGEE as function of SNR,  $T_{\text{eff}}$  and  $\log g$ . The red dots and the error bars are the mean differences and dispersions in different SNR bins. The blue line represents the  $-3.1 \text{ km s}^{-1}$  offset presented in Fig. 15.

the APOGEE have effective temperatures that differ significantly ( $> 500 \text{ K}$ ) from the templates adopted by the LSP3. A Gaussian fit to the differences of radial velocities derived from the remaining 3833 LAMOST spectra and those of the APOGEE yields an offset of  $-3.1 \text{ km s}^{-1}$  and a dispersion of  $4.8 \text{ km s}^{-1}$  (Fig. 15). The origin of the small offset is unclear, but the offset is found to be independent of the SNR and stellar atmospheric parameters (Fig. 16). As Fig. 16 shows, the magnitude of the dispersion is primarily controlled by the limited SNRs of LAMOST spectra. At high SNRs, the dispersion becomes about  $4.0 \text{ km s}^{-1}$ . The hot stars have larger scatter, with typical values of about  $15 \text{ km s}^{-1}$  for stars of  $T_{\text{eff}} > 8000 \text{ K}$ .

The RAVE survey collects medium-resolution ( $R \sim 7500$ ) spectra of stars of  $9 < I < 12 \text{ mag}$ . around the Ca II triplet region ( $8410 - 8795 \text{ \AA}$ ), and delivers radial velocities accurate to  $2.0 - 3.0 \text{ km s}^{-1}$  (Steinmetz et al. 2006). There are 83,072 radial velocity measurements for 77,461 stars in the RAVE third data release (Siebert et al. 2011). Most RAVE targets are in the southern celestial hemisphere and are significantly brighter than those targeted by the LSS-GAC. Only 158 RAVE stars are found in common with our sample. A Gaussian fit to the distribution of differences of velocities measured by the two surveys for those common stars yields an offset of  $-4.4 \text{ km s}^{-1}$  and a dispersion of  $4.4 \text{ km s}^{-1}$  (Fig. 15). Again, the dispersion arises mainly from the LAMOST measurement uncertainties.

Amongst the LSS-GAC targets of a LAMOST spectral SNR better than 5 and an effective temperature between 4000 and 9000 K, we find 8247 stars in common with the SDSS DR9 (Ahn et al. 2012), most of which are from the SEGUE survey (Yanny et al. 2009). The SDSS spectra have a wavelength coverage and resolving power almost identical to those of LAMOST. As shown in Fig. 15, a Gaussian fit to the velocity differences yields an offset of  $-4.6 \text{ km s}^{-1}$  and a dispersion of  $9.6 \text{ km s}^{-1}$ . Both the LAMOST and SDSS measurements contribute, probably equally, to the dispersion.

We have also compared the LSP3 radial velocities with datasets available from the literature, including velocities measured for stars in the M 31 and M 33 direction (Drout et al. 2009, 2012). A total of 779 stars in our sample are found to be in common with those of Drout et al. A comparison of those stars (almost all the stars have an LSP3  $T_{\text{eff}} < 7000 \text{ K}$ ) yields an average difference of  $-1.6 \pm 6.7 \text{ km s}^{-1}$ .

The above comparisons show that the LSP3 radial velocities appear to have been underestimated by a small amount, between  $\sim -5$  and  $-2 \text{ km s}^{-1}$ . Considering that the APOGEE yields radial velocities of the highest accuracy amongst all measurements dis-

cussed above, and that it also has a large number of stars in common with our sample, we have adopted an offset of  $-3.1 \text{ km s}^{-1}$  for the LAMOST velocity measurements as yielded by the above comparison with the APOGEE measurements. A constant of  $+3.1 \text{ km s}^{-1}$  is then added to all radial velocities yielded by the LSP3. The uncertainties of LSP3 radial velocities depend mainly on the spectral SNR and type ( $T_{\text{eff}}$ ) of the stars. As discussed in Section 5.2,  $\log g$  and  $[\text{Fe}/\text{H}]$  have only moderate effects on the  $V_r$  determinations. For FGK stars, the LSP3 radial velocities are probably accurate to  $5 - 10 \text{ km s}^{-1}$  for SNRs better than 10. The uncertainties increase to  $10 - 15 \text{ km s}^{-1}$  at a SNR of  $\sim 5$ . For early type stars, a  $15 \text{ km s}^{-1}$  accuracy is expected for SNRs better than 10. The assignment of errors to individual radial velocity measurements is described in Section 7.

## 6.2 Testing the stellar atmospheric parameters with the ELODIE spectral library

As described in Section 2.1, the ELODIE library contains 1959 spectra of 1388 stars obtained with an echelle spectrograph mounted on the Observatoire de Haute-Provence 193 cm, covering the wavelength range  $3900 - 6800 \text{ \AA}$  at a resolving power of 42,000 (Prugniel et al. 2007). More than half of the stars have stellar atmospheric parameters collected from the literatures and assigned flags ranging from 1 to 4 designating the quality of the parameters, with 4 being the best. The catalog also contains stellar atmospheric parameters derived using the TGMET software for all stars (Prugniel & Soubiran 2001; Prugniel et al. 2007).

The ELODIE spectra are degraded to the LAMOST resolution and processed with the LSP3. Fig. 17 compares the resultant LSP3 parameters with the ELODIE values. Only ELODIE stars in the temperature range  $3500 < T_{\text{eff}} < 10,000 \text{ K}$  that have all three stellar atmospheric parameters ( $T_{\text{eff}}$ ,  $\log g$ ,  $[\text{Fe}/\text{H}]$ ) available from the literature are included in the comparison. The Figure shows that in general the agreement is very good. A Gaussian fit to the distribution of their differences yields an average of  $-27 \pm 106 \text{ K}$ ,  $0.04 \pm 0.20 \text{ dex}$ ,  $0.07 \pm 0.10 \text{ dex}$  for  $T_{\text{eff}}$ ,  $\log g$  and  $[\text{Fe}/\text{H}]$ , respectively. Nevertheless, some systematic discrepancies are seen in  $[\text{Fe}/\text{H}]$ : For metal-poor stars, the LSP3 values are  $\sim 0.1 - 0.2 \text{ dex}$  higher than those of ELODIE. A linear fit yields

$$[\text{Fe}/\text{H}]_{\text{ELODIE}} = -0.07 + 1.08 \times [\text{Fe}/\text{H}]. \quad (9)$$

For ELODIE stars that do not have high quality parameters from the literature, many of them are either very hot or cool stars, we compare the LSP3 effective temperatures with the TGMET values. Those are shown by grey dots in the lower left panel of Fig. 17. The agreement is very good for stars of  $7000 < T_{\text{eff}} < 8500 \text{ K}$ , with a scatter of less than  $200 \text{ K}$ . For stars cooler than  $3500 \text{ K}$ , effective temperatures given by the LSP3 are about  $100 - 200 \text{ K}$  higher. At both low ( $\sim 3500 \text{ K}$ ) and high ( $\sim 9000 \text{ K}$ ) temperatures, the LSP3 effective temperatures may have been affected by the boundary effects.

## 6.3 Comparison of LSP3 stellar atmospheric parameters with the PASTEL database

The PASTEL database (Soubiran et al. 2010) archives stellar atmospheric parameters ( $T_{\text{eff}}$ ,  $\log g$ , and  $[\text{Fe}/\text{H}]$ ) published in the literatures that are determined with high-resolution and high-SNR spectra. The current archive contains more than 30,000 measurements of  $T_{\text{eff}}$  for 16,649 stars. About 6000 of them have all the three parameters available.



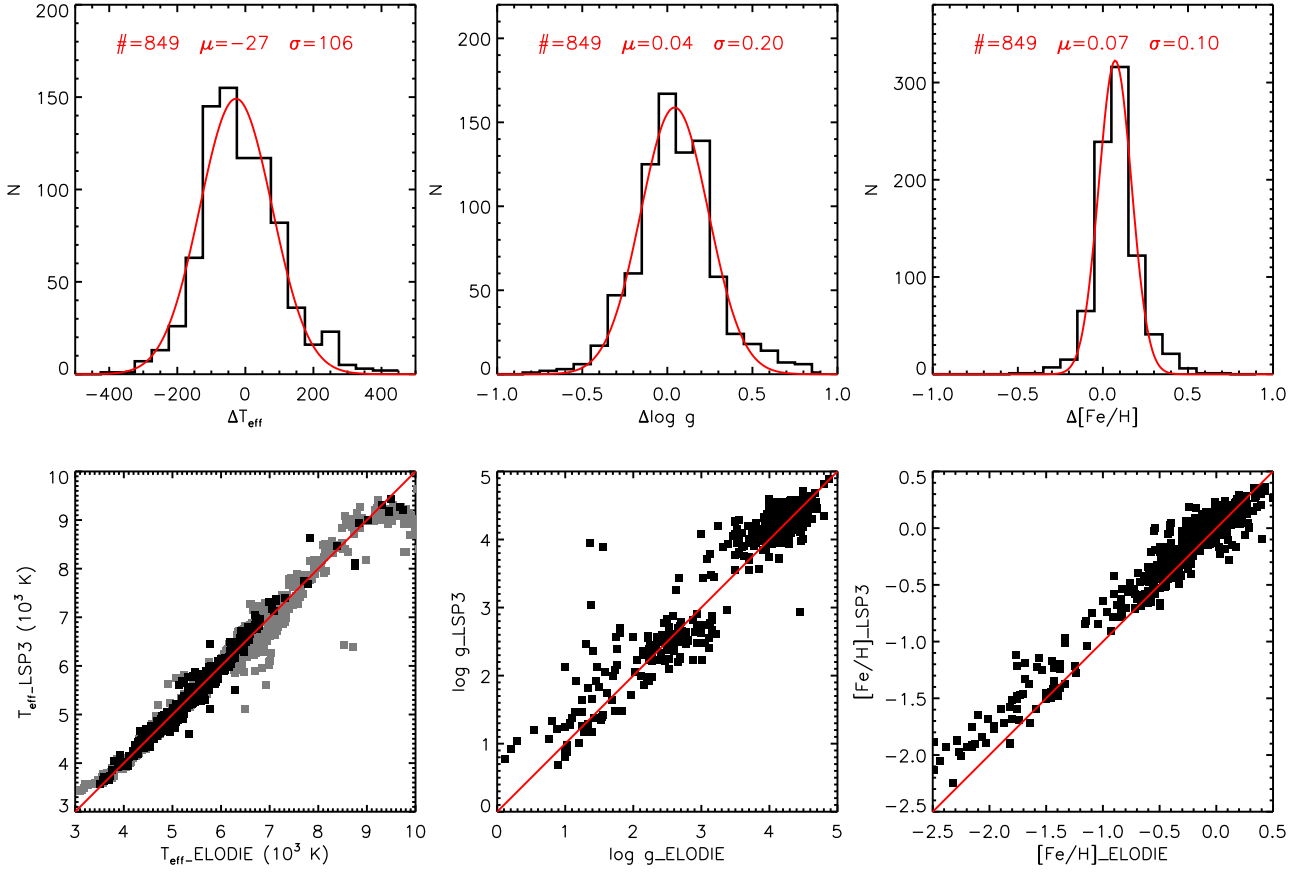


**Figure 17.** Comparison of stellar parameters derived from the ELODIE spectra with the LSP3 with values from the ELODIE library. In the upper panels, for each parameter, a Gaussian fit to the distribution of differences is over-plotted, with the number of stars, the mean and dispersion of the fitted Gaussian marked. Also in the upper panels, only stars with high quality parameters available from the literature, mostly determined with high resolution spectroscopy, are included, and those stars are marked by black dots in the lower panel. For the comparison of  $T_{\text{eff}}$  in the lower panel, the ELODIE stars without high quality parameters from the literature are also shown, as marked by grey squares. For those stars, the effective temperatures derived with the TGMET software are used.

Imposing a SNR cut of 10, we find respectively 314, 82 and 81 stars in our sample that have values of  $T_{\text{eff}}$ ,  $\log g$  and  $[\text{Fe}/\text{H}]$  recorded in the PASTEL database. For the comparison, a few stars with LSP3 values of  $T_{\text{eff}}$  cooler than 4000 K or hotter than 7500 K have been discarded. A few stars have more than one records in the PASTEL database. For those, we have excluded measurements published before 1990, and average the remaining ones with equal weights. The comparisons are shown in Fig. 18. The distributions of differences have mean and standard deviations of  $23 \pm 148$  K,  $-0.03 \pm 0.23$  dex and  $0.05 \pm 0.12$  dex for  $T_{\text{eff}}$ ,  $\log g$  and  $[\text{Fe}/\text{H}]$ , respectively. Except for a few obvious outliers, there is no systematic trend of difference in  $T_{\text{eff}}$  for stars between 4000 – 6700 K. Beyond 6700 K, the LSP3 yields temperatures of about 100 – 200 K higher. For dwarfs as well as giants of  $\log g$  between 2 – 3 dex, the LSP3  $\log g$  values match those of PASTEL well. There are only a couple of stars in the current sample that have  $\log g$  values below 2 dex or between 3 and 4 dex. For those of  $\log g < 2$  dex, the LSP3 seems to have overestimated the values. The  $\log g$  values of the few stars with a PASTEL  $\log g$  value between 3 and 4 dex seem to have been either over- or under-estimated by the LSP3. However, the numbers of stars are too small to allow for a detail investigation. For

$[\text{Fe}/\text{H}]$ , the LSP3 values are on average 0.05 dex higher than those of PASTEL. More data are needed for a more robust comparison.

#### 6.4 Applying the LSP3 to candidates of cluster members

Stars of a given open cluster (OC) are believed to form almost simultaneously from a single gas cloud with a small velocity dispersion and have almost the same metallicity. OCs thus serve as a good testbed to check the accuracy of radial velocity and metallicity determinations.

Several OCs have been targeted with the LAMOST. We select member candidates of those clusters based on the celestial coordinates, positions on the colour-magnitude diagram (CMD) and radial velocities derived with the LSP3 of the targets. Fig. 19 illustrates the process of selecting candidates of the OC M67 as an example. We obtain the basic information of the clusters (e.g. coordinates of cluster centers, cluster angular radii) from the DIAS database<sup>2</sup> (Dias et al. 2002), and select stars within twice the an-

<sup>2</sup> <http://www.astro.iag.usp.br/ocdb/>

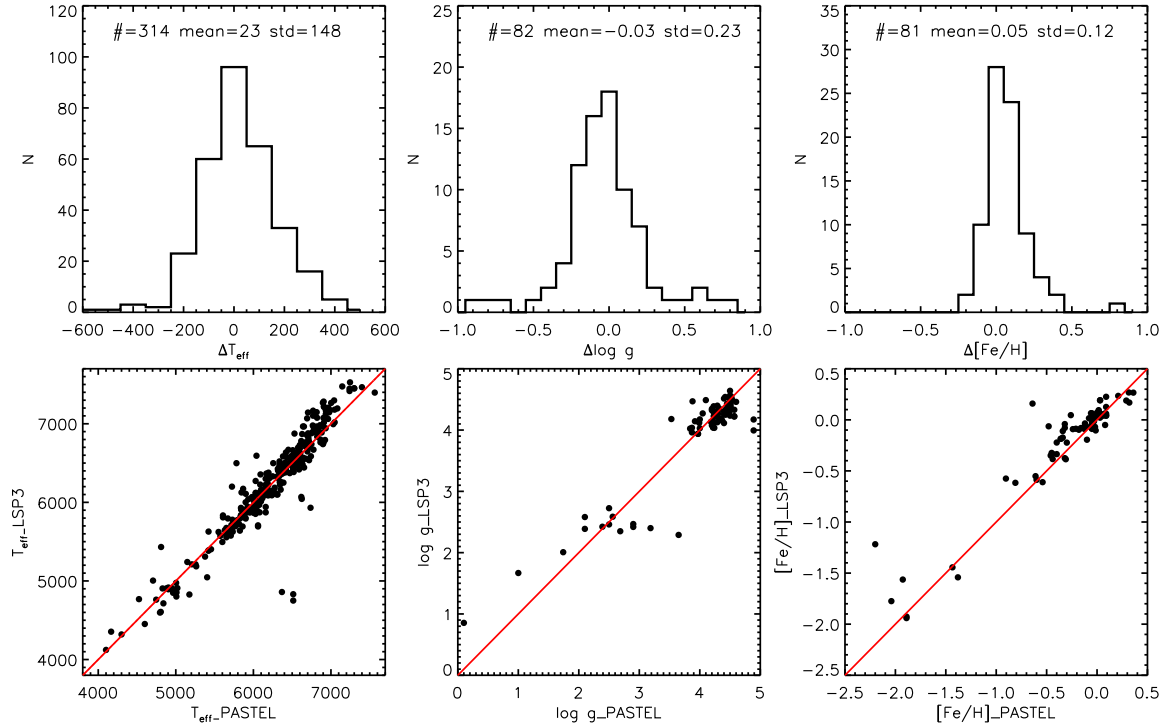


**Figure 18.** Comparison of LSP3 stellar atmospheric parameters with those from the PASTEL database. The upper panel shows the distributions of differences for the three parameters. The number of stars, the mean and standard deviation of the distribution are marked in the three top panels.

gular radius of the cluster. Then we draw a line manually delineating the cluster isochrone on the CMD, and set a colour cut at each magnitude bin to select possible candidates of cluster members. The XSTPS-GAC photometric catalog (Liu et al. 2014) is used, and if unavailable, the 2MASS catalog (Skrutskie et al. 2006) is used instead. Stars selected from the CMD are cross-identified with targets observed with the LAMOST. The distribution of radial velocities derived from the LAMOST spectra with the LSP3 of the selected stars is fitted with a Gaussian. Stars of velocities within  $2\sigma$  of the mean are adopted as candidates of the cluster members. Finally, after imposing the CMD and radial velocity cuts, we double the circular radius in celestial coordinates to include more member candidates.

Candidates of cluster members have been selected from the LSP3 results for five OCs. Details of those stars are listed in the Appendix. Note that for Berkeley 17, since the stellar density is quite low, our method fails to yield any candidate members. To define the candidate members of this cluster, we have directly cross-identified our catalog with that of Krusberg & Chaboyer (2006) directly. In the top five rows of Table 3, we compare the average values of  $[\text{Fe}/\text{H}]$  and  $V_r$  derived from the LAMOST spectra with the LSP3 for member candidates of those five OCs with the literature values. The number of candidate stars of each cluster used in the analysis is listed in the last column of Table 3. Note that a zero point correction of  $3.1 \text{ km s}^{-1}$  has been applied to all LSP3 radial velocities derived from the LAMOST spectra as discussed in Section 6.1. The agreement is very good, except for M 35 where the LSP3 estimates of  $[\text{Fe}/\text{H}]$  are on average 0.2 dex higher than the literature value. The scatters of LSP3  $[\text{Fe}/\text{H}]$  values deduced

for individual clusters are about 0.1 dex. For radial velocities, the dispersions are about  $3.0\text{--}4.0 \text{ km s}^{-1}$ .

Fig. 20 plots values of  $\log g$ ,  $[\text{Fe}/\text{H}]$  and  $V_r$  as a function of  $T_{\text{eff}}$  for candidate member stars of M 67 (NGC 2682), M 35 (NGC 2168) and NGC 2099, derived from the LAMOST spectra with the LSP3. Also over-plotted in the plots of  $\log g$  versus  $T_{\text{eff}}$  are the Yonsei-Yale ( $Y^2$ ) isochrones (Demarque et al. 2004) for the three clusters. Fig. 20 shows that in the  $T_{\text{eff}} - \log g$  plane, the LSP3 parameters generally match the isochrones. However, for the dwarf stars of  $T_{\text{eff}}$  between 5800 and 6400 K, the LSP3 values of  $\log g$  may have been systematically underestimated by about 0.2 dex, presumably due to a lack of templates of metal-rich dwarfs in that temperature range in the MILES library. For stars cooler than 7500 K, the values of  $[\text{Fe}/\text{H}]$  and  $V_r$  deduced show no obvious trend with  $T_{\text{eff}}$ .

We have also tested the accuracy of LSP3 parameters using the SDSS spectra of cluster member stars. Lee et al. (2008b) present lists of member stars of two OCs (M 67 and NGC 2420) and of three globular clusters (GCs; M 2, M 13 and M 15) that have SDSS spectra. We apply the LSP3 to the SDSS spectra of those cluster member stars. The results are presented in the last five rows of Table 3 and compared with the literature values. For  $[\text{Fe}/\text{H}]$ , the agreement is generally good. An exception is M 15, a metal-poor ( $[\text{Fe}/\text{H}] = -2.26$  dex) GC, for which the LSP3 values are on average 0.32 dex higher. For M 2, over-estimates of  $[\text{Fe}/\text{H}]$  for the hot ( $T_{\text{eff}} > 6000 \text{ K}$ ) stars, probably caused by the lack of hot, metal-poor templates in the MILES library, have led to relatively large discrepancies (0.19 dex) with the literature values. The dispersions of  $[\text{Fe}/\text{H}]$  of the 2 OCs are less than 0.1 dex, while those of the 3 GCs are about 0.2 dex. For  $V_r$ , the mean velocities are consistent

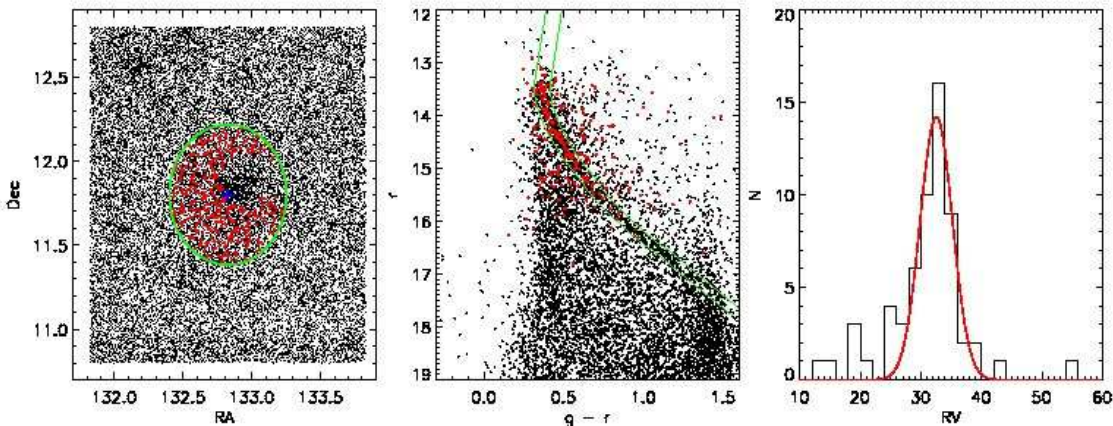


**Figure 19.** Selecting member candidates of the open cluster M67 based on the celestial coordinates (left panel), positions on the colour-magnitude diagram (middle panel) and radial velocities derived from the LAMOST spectra (right panel). The blue plus in the left panel indicates the central position of M67, while the green circle has a radius twice the angular radius of M67. Red pluses in the left and middle panels are stars observed with the LAMOST. The red curve in the right panel is a Gaussian fit to the distribution of radial velocities of stars targeted with the LAMOST that locate within the region delineated by the two green curves in the middle panel. Stars that fall inside the green circle in the left panel and within the region delineated by the two green curves in the middle panel, and have radial velocities within  $2\sigma$  of the mean are considered candidates of the cluster members.

with the literature values for all clusters, with systematic differences less than  $2.5 \text{ km s}^{-1}$  except for M 13. The latter shows a large systematic difference of  $4.0 \text{ km s}^{-1}$  for unknown reasons. Note that we have already applied a zero point correction of  $3.1 \text{ km s}^{-1}$  to all the LSP3 velocities.

### 6.5 Comparison with the APOGEE and SDSS stellar atmospheric parameters

In this Subsection, we compare the LSP3 atmospheric parameters with those from the APOGEE survey (Ahn et al. 2013) and the SDSS DR9 (Ahn et al. 2012). The APOGEE stellar atmospheric parameters are deduced by matching the continuum-normalized spectra with a grid of synthetic spectra and searching for the best fitting template via a  $\chi^2$  minimization algorithm (Ahn et al. 2013). The accuracies of APOGEE parameters are estimated to be about  $150 \text{ K}$  in  $T_{\text{eff}}$ ,  $0.2 \text{ dex}$  in  $\log g$  and  $0.1 \text{ dex}$  in  $[\text{Fe}/\text{H}]$  (Mészáro et al. 2013). There are about 33,000 stars in total in the released catalog of APOGEE with determinations of  $T_{\text{eff}}$ ,  $\log g$  and  $[\text{Fe}/\text{H}]$ , nearly all of them are giants. Cross identification with the LAMOST sources yields 1356 common stars for which both the LAMOST and APOGEE spectra have a SNR per pixel better than 15. A comparison of the APOGEE and LAMOST LSP3 parameters for those targets is presented in the upper panel of Fig. 21. The differences of the two sets of independent determinations have an average value and standard deviation of  $23 \pm 144 \text{ K}$ ,  $0.02 \pm 0.39 \text{ dex}$ ,  $0.06 \pm 0.14 \text{ dex}$  for  $T_{\text{eff}}$ ,  $\log g$  and  $[\text{Fe}/\text{H}]$ , respectively. Among the 1356 stars, 107 sources classified as giants in the APOGEE catalog ( $\log g < 3.5 \text{ dex}$ ) have LSP3  $\log g$  values larger than 4.0 dex. These are relatively hot stars, with an effective temperature around 5000 K, i.e. they are either G-dwarfs or turn-off stars. Those stars are responsible for the relatively large discrepancies between the APOGEE and LSP3 results in the cases of all three parameters. Some small systematic discrepancies are seen in  $[\text{Fe}/\text{H}]$ , similar to what found when applying the LSP3 to the ELODIE spectra [Section 6.2, Eq. (7)]. The discrepancy is about 0.1 dex at an APOGEE metallicity of about  $-0.5 \text{ dex}$ . The scatter of differences in  $\log g$  of the two sets of determinations is relatively high ( $\sim 0.4 \text{ dex}$ ). The

scatter is mainly contributed by hot stars for which the LSP3 yields  $\log g$  values larger than 3.2 dex, whereas the APOGEE finds  $\log g$  values smaller than 3.2 dex.

The SDSS stellar atmospheric parameters are derived with the SSPP, which adopts average values yielded by a variety of methods (Lee et al. 2008a), including template matching with synthetic library, neural network training and line-index algorithm. The SSPP parameters are claimed to have a precision of about  $130 \text{ K}$ ,  $0.21 \text{ dex}$  and  $0.11 \text{ dex}$  for  $T_{\text{eff}}$ ,  $\log g$  and  $[\text{Fe}/\text{H}]$ , respectively, with systematic uncertainties of comparable levels in  $T_{\text{eff}}$  and  $[\text{Fe}/\text{H}]$  (Allende Prieto et al. 2008). Note that the SDSS DR9 results differ systematically from the earlier values by about  $60 \text{ K}$  in  $T_{\text{eff}}$  and  $0.2 \text{ dex}$  in  $\log g$  as a consequence of recalibration (Ahn et al. 2012). There are 2837 LSP3 sources in common with those released in the SDSS DR9, for which both the LAMOST and SDSS spectra have SNRs better than 15. Their parameters are compared in the lower panels of Fig. 21. The differences have an average of  $-102 \pm 120 \text{ K}$ ,  $0.23 \pm 0.23 \text{ dex}$  and  $0.12 \pm 0.15 \text{ dex}$  for  $T_{\text{eff}}$ ,  $\log g$  and  $[\text{Fe}/\text{H}]$ , respectively. The SDSS temperatures are  $\sim 100 \text{ K}$  systematically higher. It seems that the SSPP calibration has systematically underestimated the  $\log g$  by  $\sim 0.23 \text{ dex}$ . The LSP3 metallicities are systematically 0.12 dex higher than the SSPP values, with no obvious trend for  $[\text{Fe}/\text{H}]$  between  $-2.0$  and  $0.5 \text{ dex}$ . For  $[\text{Fe}/\text{H}] < -2.0 \text{ dex}$ , the discrepancies become larger, reaching 0.5 dex at a SSPP metallicity of  $\sim -2.5 \text{ dex}$ . The large discrepancies at very low metallicities are likely caused by uncertainties in the LSP3 estimates due to the limited parameter coverage of the MILES library, in which only a few stars have  $[\text{Fe}/\text{H}] < -2.5 \text{ dex}$ , as well as by uncertainties in the SSPP values.

There is a group of stars with SSPP  $\log g$  values smaller than 3.5 dex but the LSP3 yields estimates larger than 4.0 dex. This leads to some apparent gaps in the plot comparing the  $\log g$  values yielded by the SSPP and by the LSP3 (the bottom middle panel of Fig. 21). The majority of those stars have effective temperatures higher than 5200 K. For those stars, the SSPP find that they are giants or supergiants, whereas the LSP3 find they are actually turn-off or dwarfs. Accurate estimates of  $\log g$  for these stars are difficult with the LSP3, given the sparse of templates at those tempera-

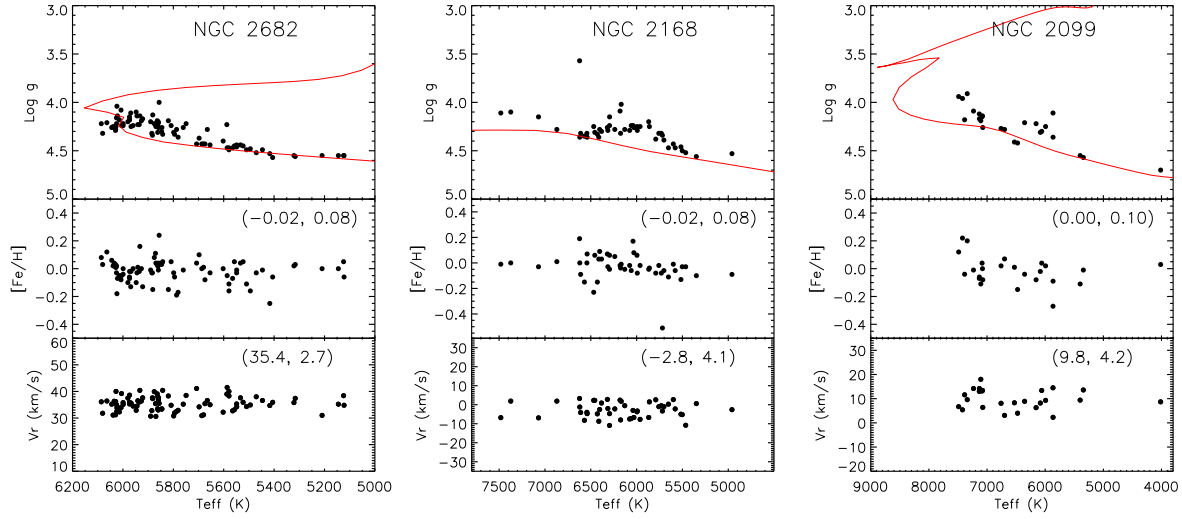


**Figure 20.** Values of LSP3  $\log g$ ,  $[\text{Fe}/\text{H}]$  and  $V_r$  plotted against  $T_{\text{eff}}$  for member candidates of the open clusters NGC 2682 (M 67; left), NGC 2168 (M 35; middle) and NGC 2099 (right) derived from LAMOST spectra. Also over-plotted are  $Y^2$  isochrones (red) in the panels of  $\log g$  versus  $T_{\text{eff}}$ . The metallicity and ages of the isochrones are 0.0 dex, 4.5 Gyr (von Hippel 2005) for NGC 2682, 0.0 dex, 0.2 Gyr (von Hippel 2005) for NGC 2168 and 0.0 dex, 0.6 Gyr (Kalirai et al. 2001) for NGC 2099.

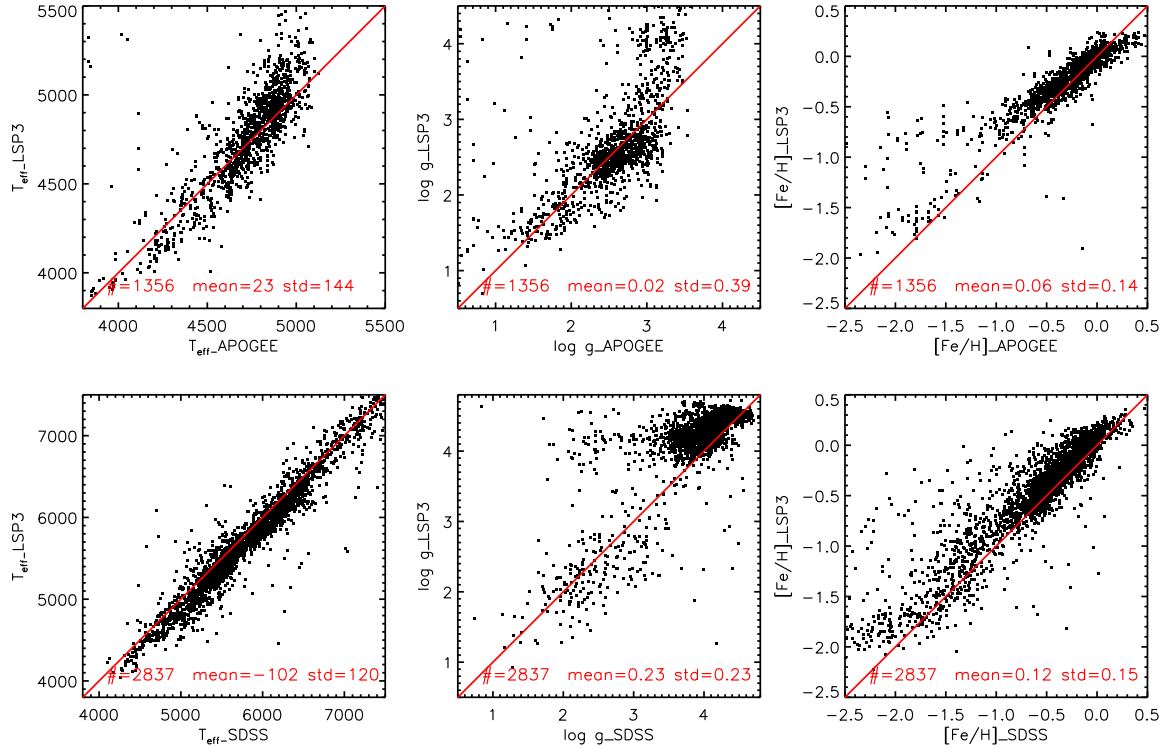


**Figure 21.** Comparison of the LSP3 parameters with those of the APOGEE (upper panels) and SDSS DR9 (lower panels). The number of stars, the mean and standard deviation of the differences are marked in each plot.



**Table 3.** Comparison of the LSP3 metallicities and radial velocities with the literature values for open and globular clusters

Cluster	[Fe/H] Literature	Reference	$\langle[\text{Fe}/\text{H}]\rangle$ This work	$\sigma([\text{Fe}/\text{H}])$ This work	$V_r$ (km s $^{-1}$ ) Literature	Reference	$\langle V_r \rangle$ (km s $^{-1}$ ) This work	$\sigma(V_r)$ (km s $^{-1}$ ) This work	$N$
Berkeley17 <sup>a)</sup>	-0.1	F05	-0.06	0.13	-73.7	F05	-73.4	3.5	5
NGC1912 <sup>a)</sup>	-0.11	L87	-0.12	0.09	-1.0	S06	2.8	2.4	14
NGC2099 <sup>a)</sup>	0.01	P10	-0.02	0.09	8.3	M08	9.8	4.5	27
M35 <sup>a)</sup>	-0.21	B01	-0.02	0.08	-5.0	S11	-2.8	4.1	47
M67 <sup>a)</sup>	-0.01	J11	-0.02	0.08	33.5	M86,M08	35.5	2.7	87
M67 <sup>b)</sup>	-0.01	J11	0.05	0.05	33.5	M86,M08	34.7	2.0	52
NGC2420 <sup>b)</sup>	-0.2	J11	-0.16	0.07	73.6	J11	73.0	3.3	163
M2 <sup>c)</sup>	-1.62	H96	-1.43	0.26	-5.3	H96	-5.0	12.0	76
M13 <sup>c)</sup>	-1.54	H96	-1.58	0.16	-245.6	H96	-249.6	7.0	293
M15 <sup>c)</sup>	-2.26	H96	-1.94	0.21	-107.0	H96	-106.5	11.0	98

<sup>a)</sup> An open cluster, for which the LSP3 parameters are derived from the LAMOST spectra.

<sup>b)</sup> An open cluster, for which the spectra analyzed with the LSP3 are from the SDSS.

<sup>c)</sup> A globular cluster, for which the spectra analyzed with the LSP3 are from the SDSS.

*References* – B01: Barrado y Navascués et al. (2001); F05: Friel et al. (2005); H96: Harris (1996); J11: Jacobson et al. (2011); L87: Lyngå (1987); M86: Mathieu et al. (1986); M08: Mermilliod et al. (2008); P10: Pancino et al. (2010); S06: Szabó et al. (2006); S11: Smolinski et al. (2011).

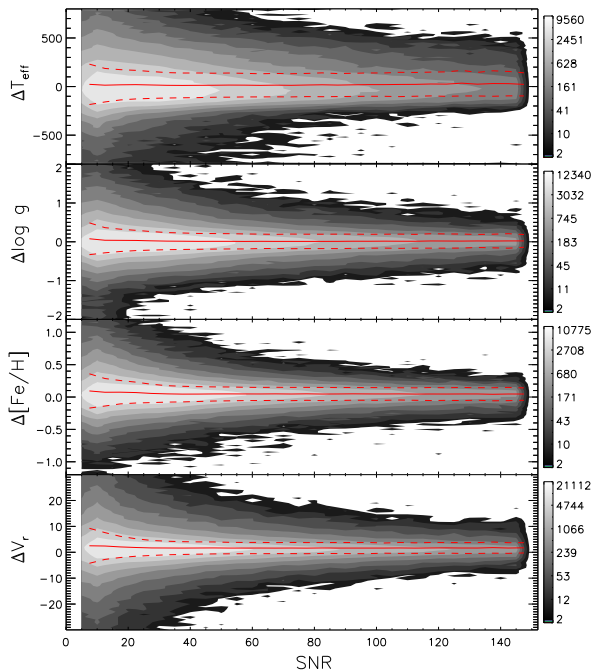


**Figure 23.** Contour maps of LSP3 and LAMOST DR1 parameter differences as a function of the spectral SNR.

tures and surface gravities. A minority of those stars are cooler, for which the SSPP finds they are red giants or clump stars, whereas the LSP3 finds they are probably subgiants or dwarfs. More analyses are needed to clarify the discrepancies.

## 6.6 Comparison with the LAMOST DR1

The first data release of LAMOST (DR1; Bai et al. 2014) contains values of  $V_r$ ,  $T_{\text{eff}}$ ,  $\log g$  and  $[\text{Fe}/\text{H}]$  deduced by LASP from 1,085,405 stellar spectra, collected by June 2013 for all components of the LAMOST spectroscopic surveys. The LASP derives stellar atmospheric parameters via template matching with the

ELODIE spectral library (Wu et al. 2014). Among the 1,085,405 spectra of LAMOST DR1, 456,697 are from the LSS-GAC sources targeted by the VB (Very Bright;  $r < 14$  mag), B (Bright;  $14 \leq r \lesssim 16.3$  mag), M (Medium bright;  $16.3 \lesssim r \lesssim 17.8$  mag) and F (Faint;  $17.8 \lesssim r \leq 18.5$  mag) plates in the direction of the Galactic anti-center as well as the M31/M33 area (cf. Liu et al. 2014; Paper III). They have been processed with the LSP3. Also processed with the LSP3 are some additional spectra not included in the DR1. They include spectra that the LASP opts not to process because of the low SNR and spectra from plates that the official LAMOST 2-D pipeline fails to process due to problems related to the flux calibration but have otherwise been successfully processed with the flux calibration pipeline developed specifically for the LSS-GAC at PKU (Paper I). Stellar parameters for all spectra of a SNR  $> 3$  are derived with the LSP3. The LASP adopts a more stringent SNR cut than the LSP3 does, in particular for VB plates collected under bright lunar conditions (Wu et al. 2014). In addition, plates collected as parts of a program to monitor the LAMOST performance (Liu et al. 2014), as well as nearly 60,000 spectra from plates of high Galactic latitudes ( $|b| > 30^\circ$ ), including some selected to study the SRCs of high Galactic latitude FoV's (and thus of low interstellar extinction), have been processed with the LSP3. A detailed description of the LSS-GAC sample can be found in Paper III.

In total, approximately 570,000 spectra with stellar parameters released in the LAMOST DR1 have also their parameters determined with the LSP3. After imposing a SNR cut of 15, the number of spectra in common amounts to 454,703 for  $T_{\text{eff}}$  in the range of 3500 – 9000 K. A direct comparison of the LSP3 and LAMOST DR1 parameters is presented in Fig. 22. In general, the agreement is quite good, with average differences of  $17 \pm 142$  K,  $0.02 \pm 0.23$  dex,  $0.05 \pm 0.13$  dex and  $1.7 \pm 2.9$  km s $^{-1}$  for  $T_{\text{eff}}$ ,  $\log g$ ,  $[\text{Fe}/\text{H}]$  and  $V_r$ , respectively. For  $T_{\text{eff}}$ , there are some systematic discrepancies for stars hotter than about 6500 K, at a level of 100 – 200 K. For dwarfs and red clump giants, the values of  $\log g$  yielded by the two pipelines agree well with each other. However, some subgiants ( $3 < \log g < 4$  dex) in the DR1 are actually found to show  $\log g$  values typical of dwarfs by the LSP3. Some systematic discrepancies are also seen for the red giant branch stars of  $\log g < 2$  dex. The LSP3 values of  $[\text{Fe}/\text{H}]$  are 0.05 dex systematically higher than

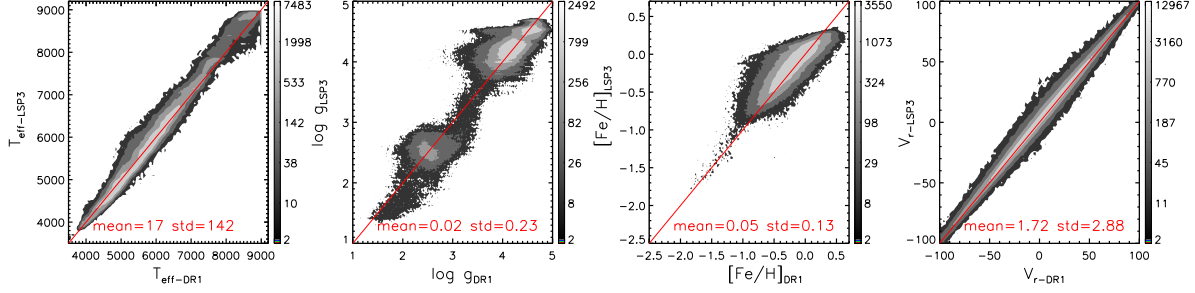


**Figure 22.** Comparison of the LSP3 parameters with those from the LAMOST DR1. A total of 454,703 stars are included in the comparison (see the text). The colours represent the stellar number density in the parameter space, with a colour bar shown on the side. The black line represents equal values. The mean and standard deviation of differences are marked in each plot.

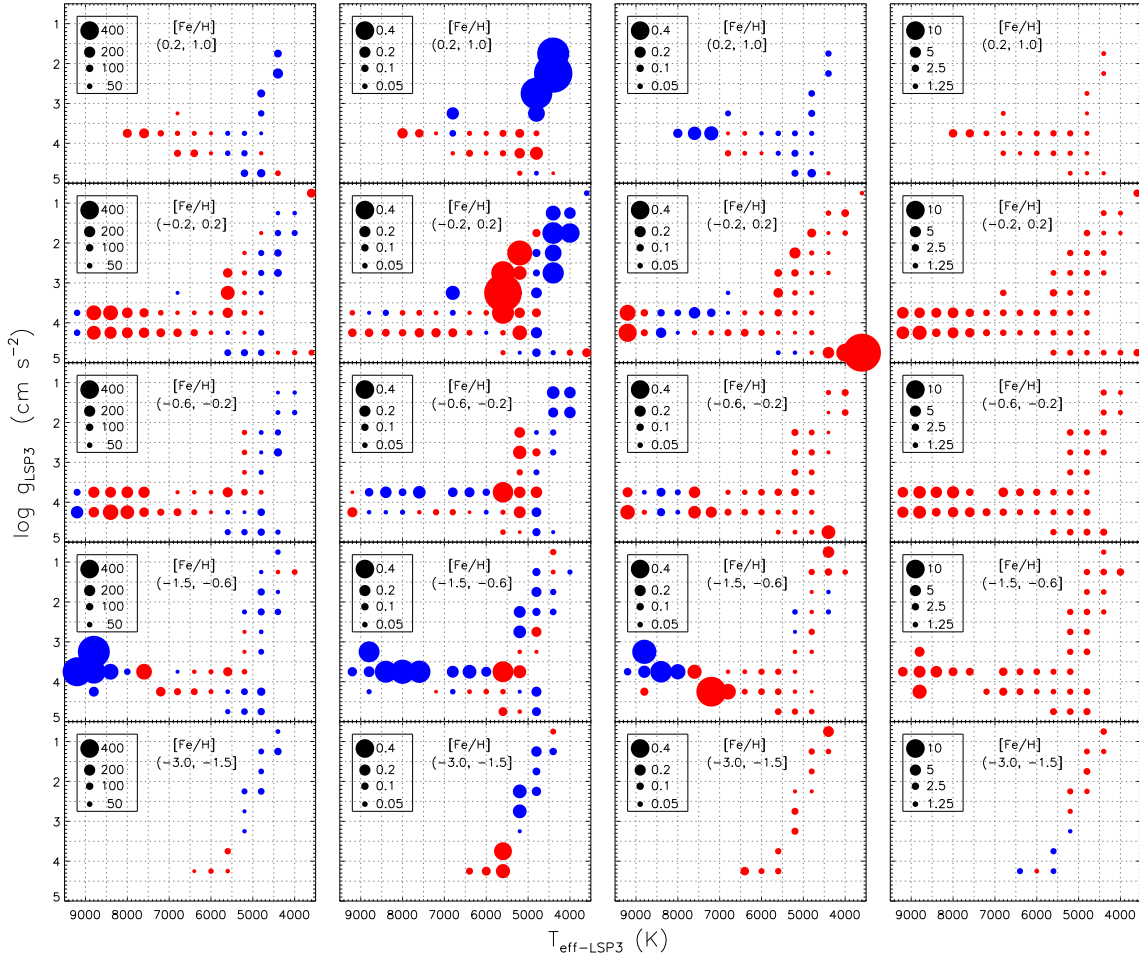


**Figure 24.** Distributions of the averages of differences of the LSP3 and LAMOST DR1 parameters in the  $T_{\text{eff}} - \log g$  plane for, from column 1 to 4,  $T_{\text{eff}}$ ,  $\log g$ ,  $[\text{Fe}/\text{H}]$  and  $V_r$ , respectively. Panels in different rows correspond to different  $[\text{Fe}/\text{H}]$  bin as marked in the plots. The magnitude of the difference are represented by the size of the symbols as marked in the plots (in units of K, dex, dex and  $\text{km s}^{-1}$  for  $T_{\text{eff}}$ ,  $\log g$ ,  $[\text{Fe}/\text{H}]$  and  $V_r$ , respectively). Red symbols represent that the LSP3 values are higher than those of LAMOST DR1 on average, while those in blue the opposite.

those of DR1, over the whole  $[\text{Fe}/\text{H}]$  range. Note that as described earlier, the LSP3 metallicities may suffer from some weak boundary effects at high metallicities, on the level of about 0.05 – 0.1 dex (Fig. 24). Values of LSP3  $V_r$  are about 1.7  $\text{km s}^{-1}$  higher than those of LAMOST DR1. Note that here the LSP3 values have not been

corrected for the offset of 3.1  $\text{km s}^{-1}$  estimated in §6.1. The differences are small however compared to the estimated uncertainties of the determinations (cf. Section 6.1).

The differences between the LSP3 and LAMOST DR1 parameters as a function of the SNR are plotted in Fig. 23. The Figure

shows that the small systematic differences noted above between the two sets of independent determinations are independent of the SNR, and the scatters of the differences decrease with increasing SNR as expected. For  $T_{\text{eff}}$ , the scatter decreases from a value of  $\sim 200$  K at a SNR of 10 to  $\sim 120$  K at SNRs  $> 40$ . For  $\log g$ , the dispersion is about 0.4 dex at a SNR of 10, and drops to less than 0.2 dex at the high end of the SNRs. For  $[\text{Fe}/\text{H}]$ , the dispersion is about 0.3 dex at a SNR of 10 and about 0.1 dex at a SNR of 40. The dispersion in  $V_r$  reaches  $6 - 7$  km s $^{-1}$  at SNRs  $< 10$ , and decreases to  $2 - 3$  km s $^{-1}$  at SNRs  $> 20$ .

To further examine any potential systematic discrepancies that might be present between the LSP3 and DR1 stellar parameters, we group the stars into different bins of  $T_{\text{eff}}$ ,  $\log g$  and  $[\text{Fe}/\text{H}]$  based on their LSP3 values for a detailed comparison. For the comparison, stars with spectral SNRs better than 15 are selected and divided into different bins of  $[\text{Fe}/\text{H}]$ :  $(-3.0, -1.5]$ ,  $(-1.5, -0.6]$ ,  $(-0.6, -0.2]$ ,  $(-0.2, 0.2]$  and  $(0.2, 1.0]$ . For each  $[\text{Fe}/\text{H}]$  bin, the stars are further divided into 400 K by 0.5 dex bins in the  $T_{\text{eff}}$  and  $\log g$  space. For each bin, the average difference between the LSP3 and LAMOST DR1 parameters are calculated. The results are plotted in Fig. 24. Clear patterns are seen in the Figure for all the four parameters. For  $T_{\text{eff}}$ , the LSP3 values of giant branch stars and G/K dwarfs are lower than those of LAMOST DR1, whereas for A/F stars the LSP3 gives higher values except for those hot stars in the  $(-1.5, -0.6]$   $[\text{Fe}/\text{H}]$  bin for which the LSP3 values are lower by more than  $\sim 400$  K. Typical values of the average differences range from a few tens to a hundred Kelvin. For hot stars of  $T_{\text{eff}} > 8000$  K the values may rise to  $300 - 400$  K. For  $\log g$ , the LSP3 yields lower values for red giant branch stars than the LAMOST DR1 does. The discrepancies are more significant for metal-rich stars. The discrepancies are likely caused by the fact that there are few stars of  $\log g < 2$  dex in the ELODIE spectral library, the spectral template library adopted by the LAMOST DR1 for parameter determinations. For subgiants of  $T_{\text{eff}} \sim 5500$  K, the LSP3 yields values of  $\log g$  that are 0.4 dex or more higher than given by the LAMOST DR1. The LSP3 values of  $[\text{Fe}/\text{H}]$  for FGK stars are constantly  $0.05 - 0.1$  dex higher than those of the LAMOST DR1, except for stars in the highest metallicity bins, where the LSP3 values for G/K stars are  $\sim 0.05$  dex lower than the LAMOST DR1 values. For dwarfs of  $T_{\text{eff}} < 4000$  K, the discrepancies in  $[\text{Fe}/\text{H}]$  are quite large ( $> 0.4$  dex). It is difficult to be sure which set of estimates, LSP3 or LAMOST DR1, is more accurate. It seems to us that the LSP3 values, peaking at  $-0.1$  dex (Fig. 8), are more consistent with what expected for a thin-disk population, while as those of DR1 are probably too low. Finally, for  $V_r$ , a small systematic difference of  $1.7$  km s $^{-1}$  is found for stars in different parameter bins, except for hot stars, where the discrepancies reach  $5$  km s $^{-1}$ .

### 6.7 Hot and cool stars

For cool ( $T_{\text{eff}} < 4000$  K) and hot ( $T_{\text{eff}} > 8000$  K) stars, few samples are available for comparisons. We thus compare the LSP3 determinations of  $T_{\text{eff}}$  with the predictions of photometric calibration to check the performance of LSP3.

Huang et al. (2014, submitted) derive an empirical relation of  $T_{\text{eff}}$  as a function of colour  $(g - K_s)$  and metallicity  $[\text{Fe}/\text{H}]$  based on over 100 calibration stars with  $T_{\text{eff}}$  inferred from the interferometric observations (e.g. Boyajian et al. 2013; Mozurkewich et al. 2003) and  $[\text{Fe}/\text{H}]$  retrieved from the PASTEL archive (Soubiran et al. 2010).  $g$  and  $K_s$  are SDSS  $g$ - and 2MASS  $K_s$ -band photometric

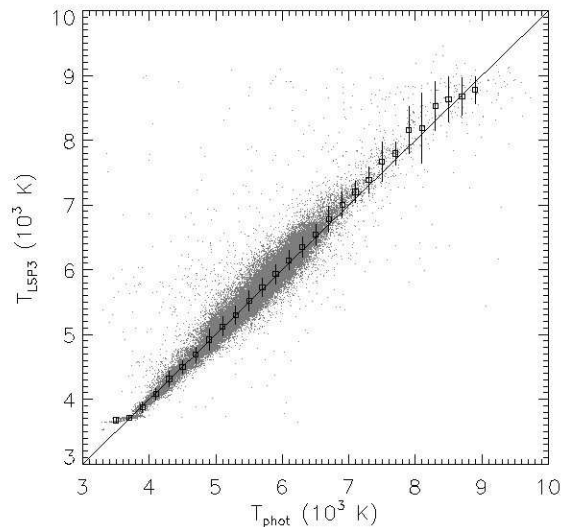


**Figure 25.** Comparison of LSP3 estimates of  $T_{\text{eff}}$  with photometric values. Black squares and error bars are averages and standard deviations of the LSP3 values of  $T_{\text{eff}}$  for stars in the individual bins of photometric  $T_{\text{eff}}$ , calculated using Eq. (10).

magnitudes, respectively. The relation is,

$$\theta = a_0 + a_1 \times (g - K_s)_0 + a_2 \times (g - K_s)_0^2 + a_3 \times (g - K_s)_0 \times [\text{Fe}/\text{H}] + a_4 \times [\text{Fe}/\text{H}] + a_5 \times [\text{Fe}/\text{H}]^2, \quad (10)$$

where  $\theta = 5040/T_{\text{eff}}$ , and  $(g - K_s)_0$  is the dereddened colour. A best fit to the data yields coefficients of 0.56653, 0.18358,  $-0.00365$ ,  $-0.02477$ , 0.02794 and  $-0.00552$  for  $a_0 - a_5$ , respectively, with a fitting residual of about 1.9 per cent. The relation is deduced for dwarfs of  $3000 < T_{\text{eff}} < 10,000$  K. In fact, an almost identical relation is also found for giants, with a difference of a few tens of Kelvin in the predicted  $T_{\text{eff}}$  for the same colour and metallicity. We have thus applied the above relation to all stars, both dwarfs and giants likewise. Note that the relation is only valid for stars of  $[\text{Fe}/\text{H}] > -1.0$  dex due to the lack of calibration stars of lower metallicities. For stars of  $[\text{Fe}/\text{H}] < -1.0$  dex, photometric  $T_{\text{eff}}$  values calculated assuming  $[\text{Fe}/\text{H}] = -1.0$  dex are adopted. Since there are only a small number of stars of metallicities lower than this in our sample, the simplification does not affect the conclusion below.

For comparison, we select stars of absolute Galactic latitudes larger than  $25$  deg. and  $E(B - V)$  given by the extinction map of Schlegel, Finkbeiner and David (1998; SFD98 hereafter) smaller than  $0.05$  mag, to minimize potential errors caused by uncertainties of the reddening corrections. We further require that the stars have spectral SNRs higher than 15. Fig. 25 compares the LSP3 estimates of  $T_{\text{eff}}$  with the photometric values calculated using the above relation. On the whole, the agreement is good. The agreement is particular good for  $3700 < T_{\text{eff}} < 7000$  K, with no systematic discrepancies and a dispersion of  $150$  K only. For  $T_{\text{eff}} < 3700$  K, the LSP3 estimates are  $100 - 300$  K higher than the photometric values, and the discrepancies increase with decreasing  $T_{\text{eff}}$ . For  $6500 < T_{\text{eff}} < 9000$  K, the LSP3 values are again  $100 - 200$  K higher than the photometric values, and shows large scatters of about  $300 - 400$  K. Few data points are available beyond  $9000$  K.

As a further check of the sanity of LSP3 determinations

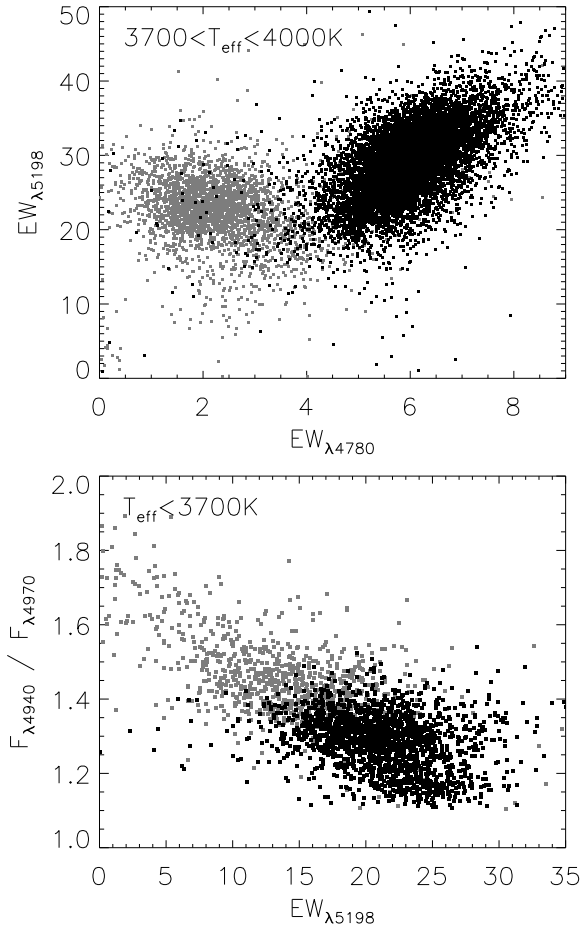


**Figure 26.** Line indices of cool dwarfs (black) and giants (grey). Upper panel: EW of the MgH  $\lambda 5198$  band plotted against that of the MgH  $\lambda 4780$  band for stars of  $3700 < T_{\text{eff}} < 4000$  K. Lower panel: Flux density ratio  $F_{\lambda 4940}/F_{\lambda 4970}$  plotted against the EW of the MgH  $\lambda 5198$  band for stars of  $T_{\text{eff}} < 3700$  K.

of  $\log g$  for cool stars, we have calculated the equivalent widths (EWs) of the  $\lambda\lambda 4780, 5198$  MgH bands and the flux density ratio  $F_{\lambda 4940}/F_{\lambda 4970}$ . The EWs of the MgH  $\lambda 4780$  band are calculated by integrating the normalized spectra between  $4760 - 4800 \text{ \AA}$ , whereas for the MgH  $\lambda 5198$  band, the integration is from  $5010$  to  $5260 \text{ \AA}$ . The flux density at  $4940 \text{ \AA}$ ,  $F_{\lambda 4940}$ , is taken to be the average value between  $4930 - 4950 \text{ \AA}$ , and  $F_{\lambda 4970}$  that between  $4965 - 4980 \text{ \AA}$ . Fig. 26 plots the distributions of EWs of the two MgH bands, as well as the  $F_{\lambda 4940}/F_{\lambda 4970}$  flux density ratios as a function of the EW of the MgH  $\lambda 5198$  band for cool giants and dwarfs that have spectral SNRs better than 10. The Figure clearly shows that for stars of  $3700 < T_{\text{eff}} < 4000$  K, the dwarfs have larger EWs of the MgH  $\lambda 4780$  band than the giants, whereas for stars of  $T_{\text{eff}} < 3700$  K, the giants all fall in the upper-left parts of the plot of  $F_{\lambda 4940}/F_{\lambda 4970}$  against  $\text{EW}_{\lambda 5198}$ . The results suggest that the LSP3 is capable of discriminating the dwarfs from the giants at  $T_{\text{eff}} < 4000$  K.

It is difficult to assess the accuracy of  $[\text{Fe}/\text{H}]$  determined from low resolution spectra for cool stars. The uncertainties are likely to be large, in particular in view that a few metal-poor cool stars of  $T_{\text{eff}} < 4000$  K are available in the currently available spectral template libraries including the MILES. More calibration sources

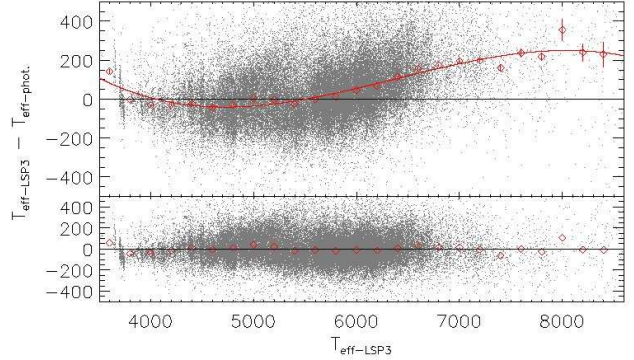


**Figure 27.** Calibrating LSP3  $T_{\text{eff}}$  against photometric values. The upper panel plots differences of the LSP3 and photometric estimates of  $T_{\text{eff}}$  as a function of  $T_{\text{eff}}$  yielded by the LSP3. Individual data points are represented by grey dots. Red diamonds and associated error bars are the average differences and standard errors for individual temperature bins. The red curve is a third-order polynomial fit to the average values. The residuals of the fit are shown in the lower panel, with the mean values of residuals for individual temperature bins represented by red diamonds.

as well as better algorithms to estimate the metallicities of those cool stars are clearly needed to access the performance of LSP3. Similarly, more studies are needed to access the performance of LSP3 for  $\log g$  and  $[\text{Fe}/\text{H}]$  of early type stars ( $T_{\text{eff}} > 8000$  K), and we leave them to future work.

## 7 CALIBRATION AND ERROR ESTIMATES OF THE FINAL PARAMETERS

As discussed in Section 6.1, after corrected for a zero-point offset of  $-3.1 \text{ km s}^{-1}$ , radial velocities determined with the LSP3 by cross-correlation with the ELODIE spectral templates are adopted as the final values.

For effective temperatures, the above comparisons of LSP3 values with those from the PASTEL and photometric calibration, as well as applying the LSP3 on the ELODIE library, show that the LSP3 over-estimates the values by  $100 - 200$  K for stars of effective temperatures at the hotter ( $T_{\text{eff}} \gtrsim 6500$  K) or cooler ( $T_{\text{eff}} \lesssim 3700$  K) end. The systematic deviations for those hot or cool stars are probably caused by the poor calibration of MILES parameters for those stars (Cenarro et al. 2007). We have thus decided to calibrate the LSP3 values of  $T_{\text{eff}}$  to those predicted by the photometric relation Eq. (10) given above. To derive a calibration relation, we first group values of  $T_{\text{eff}}$  yielded by the LSP3 for stars of spectral SNRs better than 15 and with  $E(B - V)$  given by the SFD98 extinction map less than  $0.05$  mag into bins of width  $200$  K, and then calculate the average differences between the values yielded by the LSP3 and those predicted by the photometric relation for the individual bins. A third-order polynomial is used to model the average differences as a function of  $T_{\text{eff}}$  yielded by the LSP3, such that

$$\Delta T_{\text{eff}} = a_1 + a_2 \times T_{\text{eff}} + a_3 \times T_{\text{eff}}^2 + a_4 \times T_{\text{eff}}^3 \quad (11)$$

$$T_{\text{eff}}^{\text{calib}} = T_{\text{eff}} - \Delta T_{\text{eff}} \quad (12)$$

The best fit yields  $3416$ ,  $-1.82$ ,  $3.06 \times 10^{-4}$  and  $-1.60 \times 10^{-8}$  for coefficients  $a_1$ ,  $a_2$ ,  $a_3$  and  $a_4$ , respectively. The data and fit residuals are plotted in Fig. 27, along with the fit. The model fits the data well for  $T_{\text{eff}}$  between  $3500$  and  $8200$  K, with a residual of  $25$  K



only. Since there are few stars hotter than 8500 K for the fitting, we simply assign values of  $\Delta T_{\text{eff}}$  for those hotter stars to be that at 8500 K. The  $T_{\text{eff}}$  thus calibrated are adopted as the final results of LSP3. Note that as Fig. 14 shows, at SNRs of  $\sim 7.5$ , the LSP3 may have systematically over-estimated  $T_{\text{eff}}$  by  $\sim 50$  K. However at such low SNRs, the uncertainties of  $T_{\text{eff}}$  ( $\sim 200 - 400$  K) are significantly larger than the calibration uncertainties discussed above. We have therefore ignored possible systematic errors at extremely low SNRs.

For  $\log g$ , since no obvious systematic trends are found, and also considering that there are no usable high quality calibration sources, we have opted not to apply any corrections to values yielded by the LSP3.

Comparisons with the PASTEL and APOGEE databases, as well as applying the LSP3 to the ELODIE spectral library have shown that the LSP3 may have slightly over-estimated [Fe/H] (by about 0.04 – 0.06 dex on average). In principle, one can use the PASTEL database as a calibration reference considering that it provides high quality estimates of [Fe/H] deduced from high-resolution spectroscopy. This approach seems reasonably considering that the LSP3 have estimated values of [Fe/H] for some of the PASTEL sources using the LAMOST spectra of those sources directly. On the other hand, currently the number (81) of PASTEL stars that have been observed with the LAMOST is still quite limited. In view fact that a probable offset of 0.05 dex of [Fe/H] yielded by the LSP3 is small compared with the typical uncertainties ( $\sim 0.15$  dex) estimated for the LSP3 determinations, we have decided not to apply any corrections to the LSP3 determinations of [Fe/H]. The possible causes of the small ( $\sim 0.05$  dex) offset are unclear. Note that as Fig. 14 shows, at SNRs lower than 10, the LSP3 may have systematically overestimated [Fe/H] by 0.05 to 0.1 dex. Any such possible systematic errors are small compared to the intrinsic uncertainties of the method (0.2 – 0.4 dex) at such low SNRs, and they have thus been ignored.

As the LAMOST surveys progress, more LAMOST observations of stars with high-resolution [Fe/H] measurements will become available. In addition, a project to expand the MILES spectral library, both in parameter space coverage by observing additional stars with quality measurements of stellar parameters and in wavelength coverage of the spectra and to obtain a better calibration of the MILES stellar parameters using interferometric measurements, is well under way. One can expect that values of [Fe/H] will be much better calibrated in the next release of LSP3 parameters.

The uncertainties of the final LSP3 parameters are estimated by combining the systematic and random errors,

$$\sigma(X) = \sqrt{\sigma_{\text{sys}}^2(X) + \sigma_{\text{ran}}^2(X)}, \quad (13)$$

where  $X$  represents  $V_r$ ,  $T_{\text{eff}}$ ,  $\log g$  and [Fe/H].

By systematic errors, we refer to those inherent to the LSP3 algorithms, including contributions from the uncertainties of stellar atmospheric parameters of the MILES templates or from the uncertainties of radial velocities of the ELODIE spectral library, as well as any potential systematics induced by the weighted mean and biweight mean algorithms. For radial velocities, the systematic errors, estimated to be at the level of  $\sim 0.7 \text{ km s}^{-1}$  (Section 2.1), are much smaller than the potential random errors, and are therefore set to zero. The systematic errors of stellar atmospheric parameters are estimated by fitting a 2nd-order polynomial to the absolute differences of the MILES parameters and the LSP3 derived values as a function of the latter (cf. Section 4). The fitting formulae are presented in Eqs. (14) – (16). We assume that  $\sigma_{\text{sys}}(T_{\text{eff}})$  is a function of  $T_{\text{eff}}$  only, whereas  $\sigma_{\text{sys}}(\log g)$  depends on  $\log g$  as well as on

$T_{\text{eff}}$ , and, similarly,  $\sigma_{\text{sys}}(\text{[Fe/H]})$  on [Fe/H] and  $T_{\text{eff}}$ . Coefficients of the fits are presented in Table 4.

The random errors are estimated from the dispersions (divided by square root of 2) of parameters yielded by duplicate observations (Sections 5.2), and are functions of the SNR and stellar atmospheric parameters. To estimate the random errors, the dispersions of a given parameter yielded by the duplicate observations of comparable SNRs are fitted with a 2nd-order polynomial as a function of the SNR,  $T_{\text{eff}}$ ,  $\log g$  and [Fe/H]. The fitting formulae are presented in Eqs. (17) – (20), and the coefficients are listed in Table 4. Note the fitting are based on stars of SNR between 10 and 50. For stars of SNR better than 50, the random errors are assigned to be values of those at SNR = 50.

$$\sigma_{\text{sys}}(T_{\text{eff}}) = a_1 + a_2 \times T_{\text{eff}} + a_3 \times T_{\text{eff}}^2 \quad (14)$$

$$\begin{aligned} \sigma_{\text{sys}}(\log g) = & \\ & b_1 + b_2 \times \log g + b_3 \times \log g^2 + b_4 \times T_{\text{eff}} + \\ & b_5 \times T_{\text{eff}} \times \log g + b_6 \times T_{\text{eff}}^2 \end{aligned} \quad (15)$$

$$\begin{aligned} \sigma_{\text{sys}}(\text{[Fe/H]}) = & \\ & c_1 + c_2 \times \text{[Fe/H]} + c_3 \times \text{[Fe/H]}^2 + c_4 \times T_{\text{eff}} + \\ & c_5 \times T_{\text{eff}} \times \text{[Fe/H]} + c_6 \times T_{\text{eff}}^2 \end{aligned} \quad (16)$$

$$\begin{aligned} \sigma_{\text{ran}}(T_{\text{eff}}) = & \\ & d_1 + d_2 \times T_{\text{eff}} + d_3 \times \text{SNR} + d_4 \times T_{\text{eff}}^2 + \\ & d_5 \times \text{SNR}^2 + d_6 \times T_{\text{eff}} \times \text{SNR} \end{aligned} \quad (17)$$

$$\begin{aligned} \sigma_{\text{ran}}(\log g) = & \\ & e_1 + e_2 \times T_{\text{eff}} + e_3 \times \text{SNR} + e_4 \times \log g + \\ & e_5 \times T_{\text{eff}}^2 + e_6 \times \text{SNR}^2 + e_7 \times \log g^2 + \\ & e_8 \times T_{\text{eff}} \times \text{SNR} + e_9 \times T_{\text{eff}} \times \log g + \\ & e_{10} \times \text{SNR} \times \log g \end{aligned} \quad (18)$$

$$\begin{aligned} \sigma_{\text{ran}}(\text{[Fe/H]}) = & \\ & f_1 + f_2 \times T_{\text{eff}} + f_3 \times \text{SNR} + f_4 \times \text{[Fe/H]} + \\ & f_5 \times T_{\text{eff}}^2 + f_6 \times \text{SNR}^2 + f_7 \times \text{[Fe/H]}^2 + \\ & f_8 \times T_{\text{eff}} \times \text{SNR} + f_9 \times T_{\text{eff}} \times \text{[Fe/H]} + \\ & f_{10} \times \text{SNR} \times \text{[Fe/H]} \end{aligned} \quad (19)$$

$$\begin{aligned} \sigma_{\text{ran}}(V_r) = & \\ & g_1 + g_2 \times T_{\text{eff}} + g_3 \times \text{SNR} + g_4 \times \text{[Fe/H]} + \\ & g_5 \times T_{\text{eff}}^2 + g_6 \times \text{SNR}^2 + g_7 \times \text{[Fe/H]}^2 + \\ & g_8 \times T_{\text{eff}} \times \text{SNR} + g_9 \times T_{\text{eff}} \times \text{[Fe/H]} + \\ & g_{10} \times \text{SNR} \times \text{[Fe/H]} \end{aligned} \quad (20)$$

In assigning the total errors to the final parameters, a lower limit of 30 K, 0.05 dex, 0.035 dex and  $3.0 \text{ km s}^{-1}$  has been set for  $T_{\text{eff}}$ ,  $\log g$ , [Fe/H] and  $V_r$ , respectively.

## 8 ERROR SOURCES OF THE LSP3 PARAMETERS

### 8.1 Limitation of the templates

Possible values of LSP3 parameters are obviously limited by the coverage of MILES spectral templates in the parameter space. Al-

**Table 4.** Coefficients of fitting formulae for the estimates of systematic and random errors of the LSP3 parameters<sup>1)</sup>.

$a_1$	$a_2$	$a_3$							
434.41	-1.27(-1)	1.11(-5)							
$b_1$	$b_2$	$b_3$	$b_4$	$b_5$	$b_6$				
-5.15(-1)	2.75(-2)	8.88(-3)	2.49(-4)	-3.07(-5)	-8.31(-9)				
$c_1$	$c_2$	$c_3$	$c_4$	$c_5$	$c_6$				
5.70(-1)	-7.05(-3)	-1.81(-4)	-1.65(-4)	-4.86(-6)	1.39(-8)				
$d_1$	$d_2$	$d_3$	$d_4$	$d_5$	$d_6$				
-103.27	6.03(-2)	-3.34	-1.53(-6)	6.47(-2)	-4.61(-4)				
$e_1$	$e_2$	$e_3$	$e_4$	$e_5$	$e_6$	$e_7$	$e_8$	$e_9$	$e_{10}$
-6.27(-1)	-8.91(-5)	-1.89(-2)	6.25(-1)	-2.45(-9)	9.02(-5)	-9.61(-2)	1.65(-7)	-2.15(-5)	2.52(-3)
$f_1$	$f_2$	$f_3$	$f_4$	$f_5$	$f_6$	$f_7$	$f_8$	$f_9$	$f_{10}$
1.43(-2)	2.54(-5)	-2.82(-3)	7.26(-2)	-1.64(-9)	2.24(-5)	3.40(-1)	6.19(-8)	-1.47(-5)	1.37(-3)
$g_1$	$g_2$	$g_3$	$g_4$	$g_5$	$g_6$	$g_7$	$g_8$	$g_9$	$g_{10}$
7.24	-1.66(-3)	-1.06(-1)	-10.29	4.51(-7)	4.60(-3)	11.76	-5.09(-5)	1.16(-3)	1.85(-1)

<sup>1)</sup> The numbers in parentheses are powers of ten, thus  $-1.27(-1)$  represents  $-1.27 \times 10^{-1}$ .

though the MILES library has a relatively broad parameter coverage compared with other available empirical libraries, it is nevertheless restricted by our current knowledge of stars in the solar neighborhood and suffers from various observational biases. For example, there are few metal-poor late-type (K/M) dwarfs, as well as few metal-rich AFGKM stars of  $[\text{Fe}/\text{H}] > 0.3$  dex. Such stars, albeit rare, are expected to be present in the Milky Way, but are absent in the MILES library due to either their rareness or faintness, and thus are difficult to find and measure. The parameter space covered by MILES templates is thus unlikely to encompass the whole parameter space occupied by stars targeted by the LSS-GAC which surveys a much larger volume of the Milky Way and orders of the more stars than the MILES library. It is therefore quite likely that the LSP3 parameters will suffer from the limited parameter space coverage of MILES templates in one way or other.

In addition, within the parameter space covered by the MILES library, the distribution of MILES templates are inhomogeneous. There are holes and peaks in the distribution of stars in the parameter space. The inhomogeneous distribution can lead to clustering artifacts in the resultant LSP3 parameters. To minimize such effects, we have interpolated the MILES spectra to fill up some of the most apparent holes in the  $T_{\text{eff}} - [\text{Fe}/\text{H}]$  space, and introduced  $w_2$ , a weight reflecting the distribution (clustering) of templates in the  $T_{\text{eff}} - [\text{Fe}/\text{H}]$  parameter plane, when calculating the weighted mean of parameters. Although the effects are much reduced, they cannot be avoided entirely. The effectiveness of those measures also depends strongly on the location of the target concerned in the parameter space.

The MILES spectral parameters themselves are also not entirely free of systematics. Although significant efforts have been made by Cenarro et al. (2007) to homogenize the parameters collected from various sources and determined with a variety of methods, some systematic patterns remain, especially at  $T_{\text{eff}} < 4000$  K and  $T_{\text{eff}} > 6300$  K, where the parameters are out of the range of calibration benchmarks (Cenarro et al. 2007). Note that Cenarro et al. homogenize the MILES parameters by linear regression, which

may be insufficient. For example, the giants and dwarfs from a given source may not share the same systematic errors. Any outliers, even of a small number, in the MILES can lead to significant systematic errors in the LSP3 parameters under certain circumstances. By comparing the LSP3 parameters with those predicted by the photometric relation (Section 6.7), with the PASTEL archive (Section 6.3) as well as with the ELODIE library (Section 6.2), it seems that the MILES may have overestimated  $T_{\text{eff}}$  by 100 - 200 K for stars between 6500 - 8500 K. For FGK stars, the systematic errors of MILES effective temperatures, if any, are likely to be small, on the level of a few tens of Kelvin. The systematic errors in  $\log g$  and  $[\text{Fe}/\text{H}]$  of MILES templates are also expected to be small and have negligible impacts on the LSP3 parameters compared with other potential error sources as discussed below, except for those near the boundary of the parameters space.

## 8.2 Limitation of the algorithms

In the current version of LSP3, stellar parameters are determined using spectra of the same wavelength range, 4320 - 5500 Å, for all types of star. The choice works well for the majority of FGK stars, but less so for early type or extremely metal-poor stars. For the latter, a blue part of the spectra (e.g. 3900 - 4320 Å) that include the Ca II  $\lambda\lambda 3933, 3967$  K and H lines are more appropriate. Because for such extremely metal-poor stars, most metallic lines other than the prominent Ca II doublet become too weak to be usable as metallicity tracers. The Balmer decrement and jump in the blue are also important diagnostics of  $T_{\text{eff}}$  and  $\log g$  for hot stars. Below 4320 Å, there are also other sensitive tracers of  $T_{\text{eff}}$ ,  $\log g$  and  $[\text{Fe}/\text{H}]$  for stars of various types (e.g. the Ca II  $\lambda 4226$  line; cf. Gray & Corbally 2008). Making use of spectra below 4320 Å in a proper way will no doubt improve the reliability and accuracy of the parameters deduced. As mentioned in Section 3.2, the current version of LSP3 is being optimized in order to make a better use of spectra between 3900 - 4320 Å in the blue, as well as red-arm

spectra. The improvements will be included in the next release of LSP3.

As discussed in Section 4, some LSP3 parameters may have suffered from various boundary effects in the weighted mean algorithm. For examples, values of  $\log g$  may have been overestimated by  $\sim 0.4$  dex for some subgiants, whereas for very metal-rich ( $[\text{Fe}/\text{H}] > 0.3$  dex) stars, the LSP3 may have provided values of  $[\text{Fe}/\text{H}]$  that are too low. Although such stars are relatively rare, they are of interest for some studies. Given that a project to expand the MILES library, both in parameter space coverage and in spectral wavelength range, is well under way, we expect that those effects will be much reduced in the next release of LSP3. In the meanwhile, Flags 4 – 6 (cf. Section 3.8) are assigned to help identify stars that may have suffered from those obvious boundary effects.

### 8.3 Quality of the spectra

Another, probably the most important factor that affects the accuracy of parameter determinations is the quality of spectra used, including the quality of the raw spectra (the SNR, spectral resolution) as well as the quality of data reduction (sky subtraction, flux calibration, estimates of flux density uncertainties). Some targets are seriously affected by interstellar extinction, and this also has an impacts on the reliability and accuracy of parameters derived.

#### 8.3.1 Spectral SNRs

Limited spectral SNRs are always a major contributor to the parameter uncertainties. As discussed in Section 5, the SNR is the dominant factor affecting the accuracy of the four parameters ( $V_r$ ,  $T_{\text{eff}}$ ,  $\log g$  and  $[\text{Fe}/\text{H}]$ ) in all cases. The uncertainties increase rapidly as the SNR decreases (Figs. 10 – 13).

A large number of spectra acquired during the LAMOST Pilot Surveys (September 2011 - May 2012) have low spectral SNRs. Although we have provided LSP3 parameters determined from spectra of SNRs lower than 5, we strongly advice that interested users apply a minimum SNR cut based the scientific goals when using the LSP3 parameters. One can refer to the extensive comparisons, presented in Sections 5 and 6 to choose a suitable SNR threshold. Alternatively, one can exclude stars with poor parameter determination based on the values of flags assigned, which include effects of the limited SNRs (cf. Section 7).

#### 8.3.2 Spectral resolution

Spectral resolution is another important factor that affects the determinations of stellar parameters, especially  $[\text{Fe}/\text{H}]$ . As described in Section 2.1, we degrade the resolving power of the template spectra to match the average value of spectra from the 4000 fibers of LAMOST. Fiber to fiber variations of the spectral resolving power are thus ignored, although such variations have been observed among the LAMOST fibers. Fig. 28 plots the distributions of FWHMs of an arc line at 5460 Å for 250 fibers from each of the 16 spectrographs of LAMOST, as measured on a specific arc plate. It shows that fibers of the individual spectrographs have quite different distributions of spectral resolution, with mean values ranging from 2.4 (Spectrograph #7) to 3.5 Å (Spectrograph #4), although the majority of spectrographs have a mean FWHM between 2.8 and 3.0 Å. For a given spectrograph, the resolution of the individual fibers varies by as much as 0.2 Å.

To examine how the LSP3 results are affected by the spectral

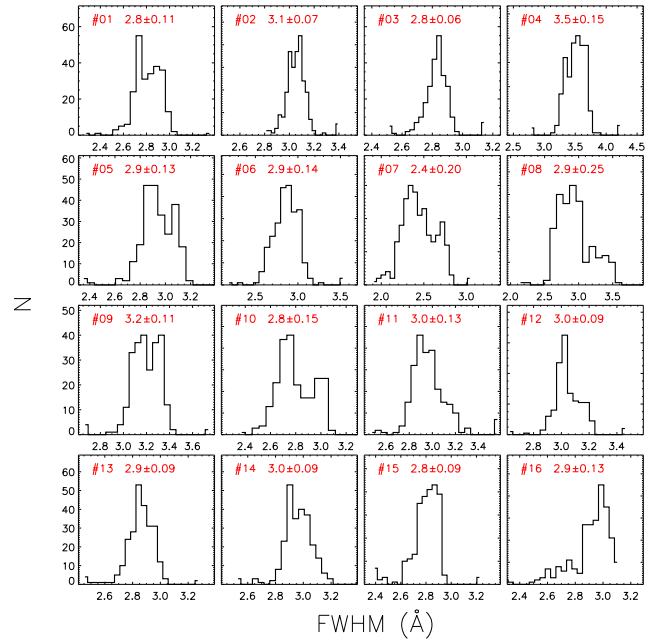


**Figure 28.** Distributions of FWHMs of the Hg  $\lambda 5460$  arc line of the 250 fibers of each of the sixteen spectrographs of LAMOST. The spectrograph ID, the mean and standard deviation of FWHMs are marked in each panel.

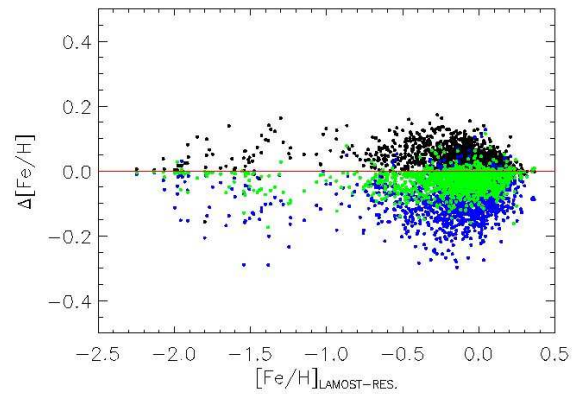


**Figure 29.** Changes in  $[\text{Fe}/\text{H}]$  values derived with the LSP3 from the ELODIE spectra degraded to a spectral resolution of FWHM of 2.4 Å (black), 3.0 Å (green) and 3.5 Å (blue), compared to those derived from the ELODIE spectra degraded to match the average resolution of the LAMOST spectra, plotted as a function of the latter.

resolution, we degrade the ELODIE spectra to different resolutions and compare the resultant LSP3 parameters. The results of  $[\text{Fe}/\text{H}]$  are shown in Fig. 29. It shows that as the FWHM varies from 2.4 to 3.0 Å, the resultant  $[\text{Fe}/\text{H}]$  can vary by as much as 0.1 – 0.2 dex on average. The variations can reach 0.2 – 0.3 dex as FWHM varies from 2.4 to 3.5 Å. Therefore, the simple treatment of spectral resolution in the current implementation of LSP3, assuming a uniform wavelength-dependent spectral resolving power for all the 4000 fibers of LAMOST, will introduce an uncertainty of  $\sim 0.1$  dex in the resultant values of  $[\text{Fe}/\text{H}]$  because of the fiber to fiber variations of the spectral resolution. For about 10 – 20 per cent stars targeted by some specific spectrographs, the errors can even reach 0.2 dex

as a consequence. In the next release of LSP3, we plan to incorporate day to day, fiber to fiber variations of the spectral resolution to further improve the accuracy of our parameter determinations.

### 8.3.3 Estimates of the spectral flux density uncertainties

Robust estimates of the spectral flux density errors for LAMOST spectra are difficult given the complexity of the data collection system and the process of data reduction. The LAMOST has an unprecedented large FoV of 20 sq. deg., and employs 4000 fibers to relay the light to 16 spectrographs. Accurate flat fielding and background (sky, scatter light) subtraction are therefore quite difficult as the process can be easily affected by the potential inhomogeneity in either the background or the instrument sensitivity. As a consequence, proper and robust propagation of errors are not easy tasks in the implementation of data reduction pipeline. Fig. 30 shows the distribution of minimum values of reduced  $\chi^2$  for spectra collected in a specific plate as a function of the spectral SNR and  $T_{\text{eff}}$ . One expects that the minimum values peak at unity in the ideal case where the flux density errors have been properly propagated and accurately modeled, and that the best-matching model (template) is a good approximation of the observation. In addition, the minimum values of reduced  $\chi^2$  should be independent of the SNR, a natural consequence of the definition of reduced  $\chi^2$ . However, Fig. 30 clearly shows that the minimum values of reduced  $\chi^2$  peak at about 0.7 instead of unity at low SNRs. This is likely caused by the overestimated flux density errors by the current pipeline. This is one of the reasons why weights are assigned to the matching templates based on the relative values of  $\chi^2$  (Section 3.4), rather than the absolute ones, i.e. based on the probability of occurrence of that particular value of  $\chi^2$  given the correct model (template). By such a choice, the potential effects caused by the underestimation of  $\chi^2$  has been much reduced. Efforts to obtain more robust estimates of the flux density errors are in progress. Fig. 30 shows that the minimum values of reduced  $\chi^2$  increases with increasing SNR. It is likely that at high SNRs, the differences between the observed spectrum and the template dominate the value of  $\chi^2$ , whereas at low SNRs, the observational uncertainties dominate. The  $\chi^2$  show little trend with  $T_{\text{eff}}$ .

### 8.3.4 Extinction and flux calibration

As described in Section 3.3, given that both the interstellar extinction and uncertainties in the spectral flux calibration could affect the actual shape of the observed SEDs, the LSP3 has used a third-order polynomial to scale the SEDs of template spectra to match that of the target spectrum when calculating  $\chi^2$ . The practice assumes that the effects of interstellar extinction and the distortions of SED caused by uncertainties in the flux calibration can be modeled with a third-order polynomial. Since the current implementation of LSP3 makes use of spectra in a limited wavelength range of 4320 – 5500 Å only, a third-order polynomial is indeed found to be sufficient for the purpose. As a check, we use a third-order polynomial to fit the extinction curve of Fitzpatrick (1999), which is thought to be a good description of the Galactic interstellar extinction by the diffuse medium (Yuan et al. 2013), assuming  $R_V = 3.1$  and  $E(B - V) = 0.5$  mag. For the wavelength range of interest, the residuals of the fit amount to only 0.1 per cent. Even for an expanded wavelength range of 3900 – 5500 Å, a third-order polynomial seems to be adequate. However, if one uses 3900 – 5500 Å, there are always some spectra for which a third-order polynomial

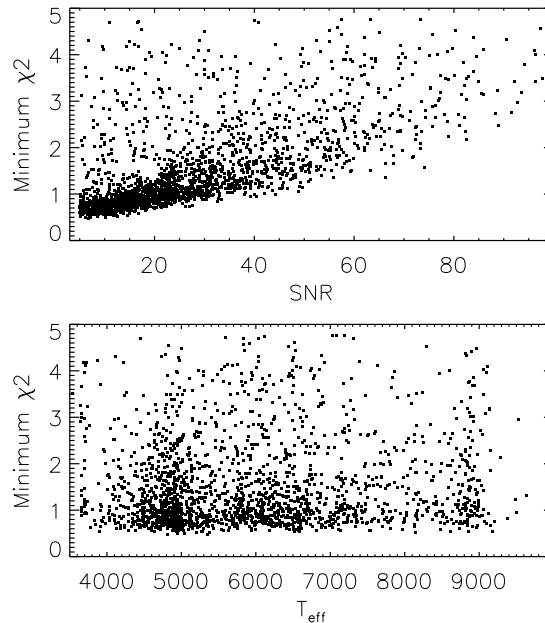


**Figure 30.** Distribution of the minimum values of reduced  $\chi^2$  as a function of the spectral SNR (upper panel) and  $T_{\text{eff}}$  (lower panel).

may be insufficient to model the deviations of their SEDs from those of template spectra.

## 9 SUMMARY

In this work, we describe the algorithms and implementation of LSP3 – the LAMOST Stellar Parameter Pipeline at Peking University, a pipeline developed to determine the stellar parameters (radial velocity  $V_r$ , effective temperature  $T_{\text{eff}}$ , surface gravity  $\log g$  and metallicity  $[\text{Fe}/\text{H}]$ ) from LAMOST spectra based on a template matching technique.

The LSP3 determines radial velocities by cross-correlating the target spectrum with templates provided by the ELODIE library. For the determinations of stellar atmospheric parameters,  $T_{\text{eff}}$ ,  $\log g$  and  $[\text{Fe}/\text{H}]$ , templates from the MILES library, obtained with a spectral resolving power similar to that of LAMOST spectra and accurately flux-calibrated, are used instead. The atmospheric parameters are estimated via two approaches, the weighted mean and  $\chi^2$  minimization. In the current released version, only results deduced with the former approach are adopted, those from the latter method are provided for comparison only. The LSP3 provides robust estimates of parameters of stars in a large parameter space ( $-1000 - 1000 \text{ km s}^{-1}$  for  $V_r$ ,  $3500 - 9000 \text{ K}$  for  $T_{\text{eff}}$ ,  $0.5 - 5$  dex for  $\log g$  and  $-2.5 - 0.5$  dex for  $[\text{Fe}/\text{H}]$ ). In the current work, we have focused on the performance of LSP3 for FGK stars.

Extensive studies have been carried out to check the performance of LSP3. The pipeline has been applied to spectral templates from the ELODIE and MILES libraries themselves, to multi-epoch LAMOST spectra of duplicate targets, to LAMOST and SDSS spectra of candidate member stars of open and globular clusters. Stellar parameters derived with the LSP3 are compared with independent measurements available from a number of external databases, including the PASTEL archive, the APOGEE, SDSS and RAVE surveys as well as the LAMOST DR1. The studies are used



to characterize and quantify uncertainties of the LSP3 parameters as a function of the spectral SNR, and of the stellar parameters.

The accuracy of radial velocity is found to mainly depend on the SNR and spectral type, and varies from  $\sim 5$ ,  $5 - 10$  and  $10 - 20 \text{ km s}^{-1}$  for G/K-, F- and A-type stars, respectively, for a SNR per pixel ( $\sim 1.07 \text{ \AA}$ ) at  $4650 \text{ \AA}$  better than 10. Typical accuracies of stellar atmospheric parameters for FGK dwarfs and most G/K giants are better than 150 K, 0.25 dex, 0.15 dex for  $T_{\text{eff}}$ ,  $\log g$  and  $[\text{Fe}/\text{H}]$ , respectively. For stars of effective temperatures cooler than 4000 K or hotter than 7000 K, the LSP3 provides reasonable  $T_{\text{eff}}$  estimates, with an accuracy of about 100 – 200 K for the cool ( $3500 < T_{\text{eff}} < 4000 \text{ K}$ ) stars, and 200 – 400 K for the hot ( $7000 < T_{\text{eff}} < 8500 \text{ K}$ ) ones. The LSP3 also provides robust  $\log g$  for stars of  $T_{\text{eff}} < 4000 \text{ K}$ . For some subgiants, the LSP3 values of  $\log g$  may have been overestimated by 0.4 dex due to boundary effects of the weighted mean algorithm. Similarly,  $[\text{Fe}/\text{H}]$  values of some stars of super-solar metallicity are probably underestimated by 0.05 – 0.1 dex. Stars suffering from obvious boundary effects can be identified using the LSP3 flags.

More calibration sources with accurate parameters are needed to improve the parameter space coverage as well as the accuracy of parameters deduced with the LSP3. A project to expand the MILES spectral library, both in the parameter space coverage as well as in the spectral wavelength range, is well under way. Inclusion of the new templates, together with better calibrated parameters of the templates are expected to significantly improve the accuracy of LSP3 results. We also plan to provide estimates of  $[\alpha/\text{Fe}]$  and  $[\text{C}/\text{Fe}]$  in the next release of LSP3.

The current version of LSP3 has been applied to over a million LAMOST spectra collected hitherto, mostly for sources targeted by the LSS-GAC. Stellar parameters deduced with the LSP3, together with estimates of  $E(B - V)$  and distances to individual stars, deduced by making use of the LSP3 parameters (Paper III), as well as those deduced from multi-band photometry (Chen et al. 2014), are presented in the form of value-added products of LAMOST data release. Following the data policy of LAMOST surveys, the data as well as the LSP3 pipeline will be public released as value-added products of the first data release of LAMOST (LAMOST DR1; Bai et al. 2014), currently scheduled in December, 2014, and can be accessed via <http://162.105.156.249/site/LSS-GAC-dr1/>, along with a description file.

**Acknowledgments** We thank the anonymous referee for valuable suggestions. This work is supported by National Key Basic Research Program of China 2014CB845700. Guoshoujing Telescope (the Large Sky Area Multi-Object Fiber Spectroscopic Telescope LAMOST) is a National Major Scientific Project built by the Chinese Academy of Sciences. Funding for the project has been provided by the National Development and Reform Commission. LAMOST is operated and managed by the National Astronomical Observatories, Chinese Academy of Sciences.

## REFERENCES

- Ahn, C. P., Alexandroff, R., Allende Prieto, C., et al. 2012, *ApJS*, 203, 21  
Ahn, C. P., Alexandroff, R., Allende Prieto, C., et al. 2014, *ApJS*, 211, 17  
Allende Prieto, C., Beers, T. C., Wilhelm, R., et al. 2006, *ApJ*, 636, 804  
Allende Prieto, C., Sivarani, T., Beers, T. C., et al. 2008, *AJ*, 136, 2070  
Bai, Z.-R. et al. 2014, *Research in Astronomy and Astrophysics*, to be submitted  
Barrado y Navascués, D., Deliyannis, C. P., & Stauffer, J. R. 2001, *ApJ*, 549, 452  
Beers, T. C., Rossi, S., Norris, J. E., et al. 1999, *AJ*, 117, 981  
Boyajian, T. S., von Braun, K., van Belle, G. et al. 2012, *ApJ*, 757, 112  
Boyajian, T. S., von Braun, K., van Belle, G. et al. 2013, *ApJ*, 771, 40  
Cenarro, A. J., Gorgas, J., Cardiel, N., et al. 2002, *MNRAS*, 329, 863  
Cenarro, A. J., Peletier, R. F., Sánchez-Blázquez, P., et al. 2007, *MNRAS*, 374, 664  
Chen, B.-Q., Liu, X.-W., Yuan, H.-B. et al. 2014, *MNRAS*, in press, arXiv: 1406.3996  
Cui, X.-Q., Zhao, Y.-H., Chu, Y.-Q., et al. 2012, *Research in Astronomy and Astrophysics*, 12, 1197  
Demarque, P., Woo, J.-H.; Kim, Y.-C. & Yi, S. K., 2004, *ApJS*, 155, 667  
Dias, W. S., Alessi, B. S., Moitinho, A. & Lepine, J. R. D. 2002, *A&A*, 389, 871  
Drout, M. R., Massey, P., Meynet, G., et al. 2009, *ApJ*, 2009, 703, 441  
Drout, M. R., Massey, P., & Meynet, G. 2012, *ApJ*, 2012, 750, 97  
Dotter, A., Chaboyer, B., Jevremović, D., et al. 2008, *ApJS*, 178, 89  
Falcón-Barroso, J., Sánchez-Blázquez, P., Vazdekis, A., et al. 2011, *A&A*, 532, 95  
Fitzpatrick, E. L. 1999, *PASP*, 111, 63  
Friel, E. D., Jacobson, H. R., & Pilachowski, C. A. 2005, *AJ*, 129, 2725  
Gray, R. O. & Corbally, C. J. 2009, *Stellar Spectral Classification* (Princeton, NJ: Princeton Univ. Press)  
Harris, W. E. 1996, *AJ*, 112, 1487  
Huang et al. 2014, *MNRAS*  
Kalirai, J. S., Ventura, P., Richer, H. B. et al. 2001, *AJ*, 122, 3239  
Katz, D., Soubiran, C., Cayrel, R., et al. 1998, *A&A*, 338, 151  
Koleva, M., Prugniel, P., Bouchard, A., & Wu, Y. 2009, *A&A*, 501, 1269  
Krusberg, Z. A. C. & Chaboyer, B., 2006, *AJ*, 131, 1565  
Jacobson, H. R., Pilachowski, C. A. & Friel, E. D. 2011, *AJ*, 142, 59  
Jester, S., Schneider, D. P., Richards, G. T. et al. 2005, *AJ*, 130, 873  
Lee, Y. S., Beers, T. C., Sivarani, T., et al. 2008a, *AJ*, 136, 2022  
Lee, Y. S., Beers, T. C., Sivarani, T., et al. 2008b, *AJ*, 136, 2050  
Lee, Y. S., Beers, T. C., Masseron, T., et al. 2013, *AJ*, 146, 132  
Liu, X.-W., Yuan, H.-B., Huo, Z.-Y., et al. 2014, in Feltzing, S., Zhao, G., Walton, N., Whitelock, P., eds, *Proc. IAU Symp. 298, Setting the scene for Gaia and LAMOST*, Cambridge University Press, pp. 310-321, preprint (arXiv: 1306.5376)  
Luo, A.-L., Zhang, H.-T., Zhang, H.-T., Zhao, Y.-H., et al. 2012, *Research in Astronomy and Astrophysics*, 12, 1243  
Lyngå, G. 1987, *Catalogue of open cluster data* (Strasbourg: CDS)  
Majewski, S. R., Skrutskie, M. F., Schiavon, R. P., et al. 2007, *Bulletin of the American Astronomical Society*, 39, #132.08  
Mathieu, R. D., Latham, D. W., Griffin, R. F., & Gunn, J. E. 1986, *AJ*, 92, 1100  
Mermilliod, J. C., Mayor, M., & Udry, S. 2008, *A&A*, 485, 303  
Mészáros, S.,  
Mozurkewich, D., Armstrong, J. T., Hindsley, R. B. et al. 2003, *AJ*, 126, 2502  
Munari, U., Sordo, R., Castelli, F., et al. 2005, *A&A*, 442, 1127  
Nelder, J., & Mead, R. 1965, *Comput. J.* 7, 308  
Pancino, E., Carrera, R., Rossetti, E., & Gallart, C. 2010, *A&A*, 511, 56  
Perryman, M. A. C., de Boer, K. S., Gilmore, G. et al. 2001, *A&A*, 369, 339  
Prugniel, Ph., & Soubiran, C. 2001, *A&A*, 369, 1048  
Prugniel, Ph., Soubiran, C., Koleva, M., et al. 2007, arXiv:astro-ph/0703658  
Prugniel, Ph., Vauglin, I., Koleva, M. 2011, *A&A*, 531, 165  
Recio-Blanco, A., Bijaoui, A., & de Laverny, P. 2006, *MNRAS*, 370, 141  
Re Fiorentin, P., Bailer-Jones, C. A. L., Lee, Y. S., et al. 2007, *A&A*, 467,

1373

- Roeser, S., Demleitner, M., & Schilbach, E. 2010, *AJ*, 139, 2440
- Sánchez-Blázquez, P., Peletier, R. F., Jiménez-Vicente, J., et al. 2006, *MNRAS*, 371, 703
- Schönrich, R. & Bergemann, M., 2013, arXiv: 1311.5558
- Skrutskie, M. F., Cutri, R. M., Stiening, R., et al. 2006, *AJ*, 131, 1163
- Smolinski, J. P., Lee, Y. S., Beers, T. C., et al. 2011, *AJ*, 141, 89
- Soubiran, C., Le Campion, J.-F., Cayrel de Strobel, G., et al. 2010, *A&A*, 515, 111
- Steinmetz, M., Zwitter, T., Siebert, A., et al. 2006, *AJ*, 132, 1645
- Szabó, Gy. M., Furész, G., Székely, P., & Szentgyorgyi, A. 2006, *ASPC*, 349, 339
- von Hippel, T. 2005, *ApJ*, 622, 565
- Wang, C., Liu, X.-W., Huang, Y. et al. 2014, in preparation
- Wilhelm, R., Beers, T. C., Gray, R. O., 1999, *AJ*, 117, 2308
- Wu, Y., Luo, A.-L., Li, H.-N., et al. 2011, *Research in Astronomy and Astrophysics*, 11, 924
- Wu, Y., Luo, A.-L., Du, B., et al. 2014, *Proceedings of IAU Symposium No.306*, in press, arXiv: 1407.1980
- Xiang, M.-S., Liu, X.-W., Yuan, H.-B. et al. 2014, *MNRAS*, (Paper I)
- Yanny, B., Rockosi, C., Newberg, H. J., et al. 2009, *AJ*, 137, 4377
- Yuan, H.-B., Liu, X.-W., Xiang, M.-S. 2013, *MNRAS*, 430, 2188
- Yuan, H.-B., Liu, X.-W., Huo, Z.-Y. et al. 2014, *MNRAS*, (Paper III)
- Zacharias, N., Finch, C. T., Girard, T. M., et al. 2013, *AJ*, 145, 44
- Zwitter, T., Siebert, A., Munari, U., et al. 2008, *AJ*, 136, 421
- Zhao, G., Zhao, Y.-H., Chu, Y.-Q., Jing, Y.-P., & Deng, L.-C. 2012, *Research in Astronomy and Astrophysics*, 12, 723

**APPENDIX A:**

**Table A1.** Candidate members of star clusters observed with the LAMOST

Cluster	RA (2000.0) (deg.)	Dec (2000.0) (deg.)	$T_{\text{eff}}$ (K)	$\log g$ ( $\text{cm s}^{-2}$ )	[Fe/H] (dex)	$V_r$ $\text{km s}^{-1}$	SNR
Berkeley17	80.080030	30.523356	4467.3	2.22	-0.16	-71.2	15.8
Berkeley17	80.158312	30.578175	4316.3	2.13	0.07	-70.3	11.3
Berkeley17	80.172651	30.601170	4994.7	2.43	-0.60	-72.5	20.6
Berkeley17	80.187027	30.633909	4786.9	2.51	-0.10	-75.3	12.2
Berkeley17	80.193692	30.519862	4416.5	2.01	-0.05	-77.8	17.9
NGC1912	81.637042	35.908412	7116.1	4.26	-0.14	2.6	13.5
NGC1912	81.922060	35.862551	7014.9	4.22	-0.05	1.3	17.7
NGC1912	81.970785	35.587292	6788.1	4.30	-0.12	-3.2	26.1
NGC1912	82.020551	35.880601	6899.6	4.31	-0.14	2.9	29.2
NGC1912	82.048509	35.761982	6925.4	4.29	-0.11	1.2	20.2
NGC1912	82.060197	35.528253	7403.7	4.09	0.02	4.2	33.5
NGC1912	82.100735	35.863465	7061.8	4.30	-0.04	4.4	13.5
NGC1912	82.118035	35.684713	6572.6	4.34	-0.11	3.0	15.9
NGC1912	82.150155	35.819408	7178.1	4.29	-0.14	6.4	35.9
NGC1912	82.198105	35.888803	7493.5	4.00	0.08	-2.6	34.3
NGC1912	82.219693	35.639864	7369.5	4.01	0.03	3.2	53.1
NGC1912	82.278458	36.271576	6814.5	4.32	-0.14	1.6	39.7
NGC1912	82.326016	36.097890	6805.3	4.31	-0.12	0.8	23.1
NGC1912	82.517774	35.812384	6974.2	4.23	-0.20	1.8	36.7
NGC2099	87.593707	32.352967	5865.0	4.36	-0.09	2.3	19.3
NGC2099	87.727658	32.584512	7085.5	4.15	0.04	13.2	58.4
NGC2099	87.741285	32.368901	6060.1	4.30	0.04	13.4	36.4
NGC2099	87.805791	32.824768	7488.5	3.94	0.12	6.7	34.3
NGC2099	87.806249	32.465110	7078.9	4.14	0.00	13.4	61.0
NGC2099	87.939731	32.498580	6759.4	4.27	0.02	8.1	75.0
NGC2099	87.945725	32.536423	7131.8	4.17	-0.06	14.2	73.1
NGC2099	87.959815	32.429468	5993.5	4.25	0.02	9.3	24.8
NGC2099	87.963059	32.639557	5399.1	4.55	-0.11	9.4	11.6
NGC2099	87.979722	32.693774	7385.9	4.18	-0.04	11.6	32.8
NGC2099	87.999774	32.329985	6529.4	4.41	0.01	8.3	31.2
NGC2099	88.019759	32.621234	5344.0	4.57	-0.01	13.6	16.1
NGC2099	88.032838	32.444156	5865.9	4.11	-0.27	14.5	34.4
NGC2099	88.058791	32.549114	4014.8	4.70	0.03	8.7	11.2
NGC2099	88.060874	32.630768	6699.3	4.28	0.07	3.1	62.1
NGC2099	88.077153	32.666130	7133.0	4.12	-0.07	13.0	69.9
NGC2099	88.096656	32.586605	6083.6	4.31	-0.02	8.2	30.8
NGC2099	88.164077	32.340684	6475.0	4.42	-0.15	4.0	26.9
NGC2099	88.166683	32.707965	6156.6	4.22	-0.08	6.3	27.1
NGC2099	88.187577	32.798827	7340.6	3.91	0.20	9.6	84.9
NGC2099	88.190944	32.591233	6354.3	4.21	-0.04	8.9	23.9
NGC2099	88.198069	32.406829	7422.6	3.96	0.22	5.4	48.8
NGC2099	88.238835	32.623684	7073.9	4.26	-0.08	6.4	70.8
NGC2099	88.331256	32.462140	7233.4	4.09	-0.01	14.2	30.9
NGC2099	88.402562	32.446199	7107.5	4.19	-0.11	18.0	66.9
M35	90.812715	24.047386	5652.9	4.47	-0.11	0.3	13.3
M35	91.056838	24.446490	6870.5	4.28	0.01	1.9	42.9
M35	91.057711	23.531181	7481.9	4.11	-0.01	-6.8	49.7
M35	91.079898	24.035402	5718.7	4.34	-0.51	-3.3	13.8
M35	91.156781	24.785329	6039.3	4.24	0.17	-3.0	26.5
M35	91.170843	23.500702	5516.3	4.46	-0.13	-5.0	11.5
M35	91.226171	25.216736	7373.5	4.10	0.00	1.9	42.9
M35	91.242804	24.765560	5791.3	4.38	-0.08	2.6	28.2
M35	91.370669	23.923172	6456.6	4.31	0.06	2.3	32.8
M35	91.429181	24.870560	7070.4	4.15	-0.03	-6.9	108.2
M35	91.502833	23.891186	6295.0	4.15	0.06	-4.7	30.8
M35	91.570607	24.002285	6295.6	4.24	-0.05	-10.9	27.3
M35	91.576787	24.316003	6620.2	4.36	0.00	-1.2	16.6
M35	91.631412	24.938741	6383.1	4.30	0.03	0.9	24.1
M35	91.637225	23.993000	6569.5	4.35	-0.15	-8.2	55.4
M35	91.655450	24.214521	6540.1	4.36	0.07	-4.7	66.8

Table A1. – *continued*

Cluster	RA (2000.0) (deg.)	Dec (2000.0) (deg.)	$T_{\text{eff}}$ (K)	$\log g$ ( $\text{cm s}^{-2}$ )	[Fe/H] (dex)	$V_r$ $\text{km s}^{-1}$	SNR
M35	91.672723	24.807495	5579.1	4.47	-0.06	-2.2	13.0
M35	91.684405	24.280308	5992.4	4.29	-0.08	-3.3	28.9
M35	91.744527	25.133462	6428.3	4.33	-0.15	-4.8	21.0
M35	91.792861	23.956444	6622.3	3.57	0.19	3.3	32.5
M35	91.951777	24.766640	5599.6	4.43	-0.01	2.7	16.1
M35	92.109718	24.459892	6076.0	4.29	-0.02	-7.5	45.3
M35	92.122290	24.483560	6129.6	4.28	-0.05	-0.5	42.9
M35	92.123130	24.235860	6610.8	4.32	-0.09	-4.1	37.0
M35	92.158984	24.370499	6412.6	4.36	0.03	-8.7	61.5
M35	92.175891	24.539354	6314.0	4.29	-0.03	-2.0	47.1
M35	92.182670	24.286720	6175.1	4.32	-0.04	-8.0	55.1
M35	92.199540	24.336500	6542.5	4.32	0.00	-4.0	87.5
M35	92.234890	24.451880	5348.3	4.56	-0.10	0.6	21.1
M35	92.315396	24.513493	5702.4	4.39	-0.06	-1.0	25.7
M35	92.330580	24.319080	6058.7	4.24	-0.06	-7.3	34.2
M35	92.349589	24.388638	6030.1	4.26	0.08	-6.7	33.3
M35	92.380897	24.463773	5730.3	4.32	-0.08	-0.5	13.1
M35	92.438109	23.577000	5867.9	4.20	-0.05	-6.7	58.5
M35	92.440868	24.756354	5996.1	4.25	0.06	-3.7	33.4
M35	92.482379	24.504451	5502.2	4.50	-0.03	-5.2	16.9
M35	92.529745	25.631488	6319.2	4.26	0.07	2.8	24.4
M35	92.569606	24.340346	4959.9	4.53	-0.09	-2.6	16.6
M35	92.576234	25.305559	5962.3	4.25	-0.02	-7.7	12.2
M35	92.698655	24.300170	5757.8	4.32	-0.02	-1.0	30.5
M35	92.748451	25.319479	6168.3	4.02	-0.01	1.8	18.2
M35	92.913694	24.970778	5860.5	4.25	-0.04	1.5	19.7
M35	92.984542	25.291350	5464.7	4.52	-0.03	-10.8	27.7
M35	93.036766	25.323962	6180.7	4.09	-0.02	2.4	33.1
M35	93.070419	25.104811	6238.2	4.28	0.05	-2.2	47.6
M35	93.113441	23.558530	6403.2	4.28	0.09	-2.5	17.9
M35	93.406855	24.992339	6468.2	4.25	-0.23	2.3	16.2
M67	132.255818	11.982972	6080.5	4.32	0.03	31.8	56.0
M67	132.270552	11.696430	5144.9	4.55	-0.00	35.2	14.4
M67	132.284122	12.334856	6029.3	4.29	0.03	31.2	22.9
M67	132.313167	11.737440	5885.3	4.32	-0.03	32.8	35.8
M67	132.366239	11.706203	5586.3	4.47	-0.05	41.5	23.9
M67	132.400701	11.363308	5417.1	4.53	-0.25	34.7	10.3
M67	132.433580	12.367976	5209.6	4.55	0.00	31.0	12.2
M67	132.438195	12.040859	5969.0	4.11	-0.13	35.5	72.4
M67	132.440581	11.979247	5446.3	4.49	-0.01	36.6	19.7
M67	132.467429	11.546726	5944.2	4.14	-0.03	34.5	58.4
M67	132.485962	11.948136	5973.7	4.18	-0.07	35.9	51.1
M67	132.503509	11.702729	5861.6	4.24	0.02	38.0	18.1
M67	132.541439	11.998321	5870.8	4.23	0.11	35.4	46.3
M67	132.550622	11.714708	5316.1	4.56	0.03	37.4	20.5
M67	132.561035	11.741567	5321.2	4.55	0.02	35.8	10.9
M67	132.567596	12.326211	5781.0	4.36	-0.17	32.9	14.9
M67	132.570682	12.450383	6044.5	4.26	0.06	35.2	55.6
M67	132.576618	11.906679	5548.5	4.44	-0.01	34.2	25.7
M67	132.577855	12.266950	5860.3	4.20	0.02	33.0	13.6
M67	132.583854	11.819741	6034.7	4.26	0.04	36.3	68.4
M67	132.583890	11.819694	6039.1	4.25	0.02	31.1	43.8
M67	132.589041	11.985801	5494.4	4.48	-0.16	34.9	13.3
M67	132.589891	11.839766	5680.0	4.43	0.01	31.2	20.2
M67	132.590068	11.682061	5940.9	4.23	0.01	36.5	53.2
M67	132.620890	11.635912	5999.3	4.22	-0.04	35.8	42.8
M67	132.658436	11.911304	5557.7	4.45	0.05	33.1	28.4
M67	132.658636	11.331912	5707.6	4.43	0.04	41.1	37.0
M67	132.661141	11.203579	5875.5	4.22	0.08	39.9	41.3
M67	132.675421	11.439848	6021.5	4.14	-0.07	34.1	67.4
M67	132.677078	11.663713	6063.8	4.21	0.12	36.4	42.1
M67	132.685551	11.990308	5749.3	4.22	-0.53	38.5	21.9
M67	132.696363	11.715231	5842.2	4.33	0.05	40.4	31.8
M67	132.702588	12.061477	6025.5	4.16	-0.03	32.3	41.3



Table A1. – *continued*

Cluster	RA (2000.0) (deg.)	Dec (2000.0) (deg.)	$T_{\text{eff}}$ (K)	$\log g$ ( $\text{cm s}^{-2}$ )	[Fe/H] (dex)	$V_r$ $\text{km s}^{-1}$	SNR
M67	132.717930	11.750991	5579.2	4.47	-0.11	40.0	15.0
M67	132.721149	11.667290	5926.7	4.19	-0.00	36.4	59.4
M67	132.721518	11.792825	5973.6	4.18	-0.02	38.6	51.8
M67	132.726414	12.259466	6005.5	4.24	-0.05	39.2	39.2
M67	132.733352	11.897774	5947.4	4.10	-0.10	32.9	70.2
M67	132.735524	11.635607	5795.0	4.33	-0.06	31.9	12.3
M67	132.738335	12.093445	5869.2	4.25	0.04	30.6	16.3
M67	132.741071	11.587439	5862.0	4.31	0.03	33.5	42.5
M67	132.749192	11.853498	5509.5	4.49	-0.11	34.3	24.2
M67	132.783816	12.018475	5819.7	4.19	-0.15	38.3	55.5
M67	132.787759	12.050611	5980.3	4.20	-0.10	37.5	36.2
M67	132.791306	11.771373	5674.4	4.43	-0.08	35.4	40.7
M67	132.796550	11.443022	5787.0	4.28	-0.19	32.5	46.6
M67	132.801343	11.310762	5859.4	4.26	-0.01	36.8	32.4
M67	132.823736	12.461495	5697.6	4.37	0.10	34.2	13.1
M67	132.836630	11.661145	5858.8	4.21	0.04	37.6	40.6
M67	132.840996	11.721588	5687.0	4.43	0.00	30.9	15.6
M67	132.846624	11.654122	5533.5	4.44	0.04	37.6	17.3
M67	132.860338	11.643576	5881.6	4.13	-0.15	37.3	62.2
M67	132.875371	11.458759	5564.7	4.47	-0.07	32.7	13.9
M67	132.911410	11.710382	5883.0	4.34	-0.03	37.6	36.8
M67	132.915392	12.203025	5124.3	4.55	0.05	38.4	12.2
M67	132.921686	12.409107	5959.7	4.24	-0.00	34.5	19.0
M67	132.937204	11.649700	6025.4	4.22	0.02	35.0	51.5
M67	132.940772	11.645889	5665.1	4.28	-0.79	36.6	26.5
M67	132.969325	11.513024	5921.7	4.17	-0.13	37.6	38.7
M67	132.995892	11.696994	5523.0	4.45	0.05	35.9	19.0
M67	133.005656	12.186139	6014.3	4.18	-0.05	32.3	44.7
M67	133.006516	12.065050	5846.5	4.30	0.03	33.4	25.9
M67	133.034143	12.262911	5798.6	4.31	-0.03	30.8	13.1
M67	133.041442	12.175305	5932.8	4.14	0.16	40.4	11.1
M67	133.058637	12.212279	5999.1	4.24	0.00	35.1	47.0
M67	133.072200	12.334044	5548.7	4.46	-0.03	35.3	22.0
M67	133.091003	11.779630	5974.0	4.15	-0.06	35.3	22.3
M67	133.104021	11.174182	5808.7	4.24	0.05	34.8	32.5
M67	133.104041	11.174156	5863.8	4.19	0.03	39.1	17.7
M67	133.107283	12.384580	5890.0	4.20	-0.01	30.7	16.1
M67	133.126162	11.714005	5845.2	4.26	0.04	33.4	25.0
M67	133.137844	11.756676	6027.4	4.25	0.01	40.0	46.4
M67	133.149849	11.623530	5470.8	4.52	-0.03	38.0	14.7
M67	133.186029	11.430369	5935.1	4.23	-0.02	36.0	44.6
M67	133.244947	11.757958	5122.3	4.55	-0.06	34.8	13.7
M67	133.282203	11.803569	6007.5	4.08	-0.08	33.9	48.9
M67	133.291121	12.004910	5760.5	4.26	-0.01	35.2	11.3
M67	133.301250	11.674549	5602.2	4.40	-0.00	32.2	26.9
M67	133.327231	12.366576	5587.6	4.23	-0.55	39.0	11.9
M67	133.340579	11.287396	5967.9	4.25	-0.02	35.6	39.2
M67	133.354071	12.417892	5654.2	4.44	-0.03	35.0	22.1
M67	133.384039	12.186201	6023.8	4.04	-0.18	33.8	51.3
M67	133.464535	11.292121	5856.3	4.00	0.24	35.5	63.2
M67	133.490143	12.262763	6028.8	4.28	0.01	36.2	51.2
M67	133.510279	11.875851	5405.7	4.57	-0.06	35.9	16.3
M67	133.511237	12.134510	6085.8	4.22	0.08	36.1	10.9
M67	133.525382	11.753270	5579.1	4.49	-0.16	38.3	19.9